Spring 2023

Multidimensional Transport-Coupled Numerical Investigation of Non-premixed Low-Temperature Flame in Atmospheric and High-Pressure Systems

Sudipta Saha

MULTIDIMENSIONAL TRANSPORT-COUPLED NUMERICAL INVESTIGATION OF NON-PREMIXED LOW-TEMPERATURE FLAME IN ATMOSPHERIC AND HIGH-PRESSURE SYSTEMS

by

Sudipta Saha

Bachelor of Science
Bangladesh University of Engineering and Technology, 2013

Master of Science
University of South Carolina, 2019

Submitted in Partial Fulfillment of the Requirements

For the Degree of Doctor of Philosophy in

Mechanical Engineering

College of Engineering and Computing

University of South Carolina

2023

Accepted by:

Tanvir Farouk, Major Professor

Sang Hee Won, Committee Member

Jamil Khan, Committee Member

Jasim Imran, Committee Member

Cheryl L. Addy, Interim Vice Provost and Dean of the Graduate School

DEDICATION

To our daughter, my parents, wife, brother, and friends.

ACKNOWLEDGMENTS

My graduate journey at the University of South Carolina has been a challenging yet rewarding experience, and I owe the completion of this dissertation to the many individuals who have supported and inspired me along the way.

First and foremost, I would like to express my deepest gratitude and appreciation to my advisor, Dr. Tanvir Farouk, for his exceptional guidance and supervision throughout my graduate research. Thanks to his mentorship, I was able to obtain my Master's degree in thermal-fluid science, and acquired a solid understanding of numerical modeling and simulation techniques for complex energy systems. This served as a strong foundation for my doctoral studies, which focused on analyzing chemically reacting flows. I am especially grateful for the multidisciplinary collaborative work he involved me in, which helped me grow a versatile mindset to approach complex physical problems. Working at the ReActing System And Energy Research (RASAER) laboratory under undoubtedly made me a better engineer, critical thinker, and an adept problem solver.

I am grateful to Dr. Sang Hee Won for his invaluable and in-depth scrutiny of my work, upon which my research improved significantly. I am grateful for his extensive meeting hours and categorical guidance, which helped me advance my work on counterflow cool flame research. I am grateful to Dr. Jamil Khan for his unwavering support and mentorship throughout my graduate journey. His words of encouragement and guidance were invaluable during the moments of frustration and self-doubt (in other word, ‘imposter syndrome’). I would like to express my appreciation to Dr Jasim Imran for his

support, scientific feedback, and judicious comments on my work. Finally, I like to express my gratitude towards my department chair, Dr Travis Knight, for his steadfast support and emphasis on academic integrity, ethics, and hard work.

I would like to take a moment to express my sincere appreciation to the members of the RASAER lab who have provided me with unwavering support. I feel fortunate to have worked alongside Fahd, Ali, Malik. Farhan, Rajib, Damon, Greg, Ejaz, and Ebrahim during my PhD studies. I am especially grateful to Fahd, who guided me with his extensive knowledge and experience in combustion systems and chemical kinetics. Thanks to his valuable insights, I was able to enhance my understanding of combustion analyses and receive critical advice on career development. I consult with him to this day and hope to have his continued support in the coming years. Similarly, Ali has been a true friend and a kind soul who provided me with vital resources and tips on OpenFOAM, which proved invaluable in my research. I will always be grateful to this down-to-earth person with an amazing personality for his support and kindness.

Graduate life can be tough, especially when you are far away from your family and home. However, I consider myself blessed to have had the support of some amazing individuals during our time in Columbia. The local Bangladeshi community was a source of comfort for me in times of homesickness. I am deeply grateful to Titan da, Kedar da, Gopa di, and Aporna di for treating us like their family and always being there for us. I will always cherish the love and kindness we received from Aruna di and Himadri da, who we consider our local guardians. Their support and guidance were invaluable to us in a foreign land.

Alongside the Bangladeshi community in Columbia, we were fortunate to have made some wonderful local friends. I am grateful for the friendships I formed with Patricia Canon, Scott and Victoria Andes, Jamie and Tasha Rogers, and their families. They embraced us with warmth and provided us with strength and support when we needed it the most. I will miss the Thursday lunch at the Carolina BCM with the wonderful people there (Rock, Fatty, Chelsea and more). We are grateful to have met these amazing people, who helped make Columbia feel like a home away from home.

I must also acknowledge Dr. Jeffery Domey and Mr. Jim Peris for recruiting me into their group at the Corning Inc. R&D division and supporting me in completing my PhD remotely. They have been amazing mentors, continuously guiding me towards further improvement and growth. Joining their team, which conducts fundamental research and development in an incredible team environment, has been a privilege and a great opportunity for me.

Last but certainly not least, I want to express my gratitude to my family. My father, Dr. Subas Chandra Saha, is a constant source of energy, resilience, and determination, and my mother, Chandana Saha, is the main reason for my success today. My younger brother, Auritra, has always been a great support for me. I am especially thankful to my wife, Anu Pria Roy, for her caring and supportive presence in both my family and work life. During my PhD, she endured through my frustration and eccentric behavior, and helped me keep believing in myself. Finally, my baby daughter Arya is a blessing in my life, and her everyday presence gives me hope and courage.

ABSTRACT

Gas-phase chemical reactions coupled with multidimensional fluid flow and heat and mass transport are found in various applications, i.e., from conventional engine applications to novel combustion techniques. With the goal of understanding such complex coupling in such reacting flow systems, this dissertation work focuses on developing multi-physics simulation frameworks to investigate the effect of multidimensional transport on flame dynamics. This study primarily focuses on the modeling and simulation of low-temperature flame formation in i) a canonical experimental setting with counterflow burners and ii) a supercritical water medium (i.e., hydrothermal flame).

In the first part of the dissertation, simulations of the cool flame formation of dimethyl ether (DME) combustion in a counterflow geometry have been presented. Historically, flame formation in counterflow geometry is studied to understand the strength of the flames under the effect of the stretch. The formation of hot flames in this arrangement has been studied profoundly over the last half-century. The counterflow/opposed-flow diffusion flame configuration allows one to implement a similarity solution approach, which makes the numerical modeling approach tractable and inexpensive [1]. This approach assumes the dependent variables to be a function of the axial distance only. Hence, the problem can be represented by a quasi-one-dimensional (1D) numerical model. This assumption is valid for high Reynolds numbers (i.e., high strain rate) and large activation energy (i.e., thin flame sheets), which are generally the case for a hot flame formation in counterflow geometry. However, this similarity solution approach becomes

questionable for a low-temperature cool flame where the strain rate is relatively low, and the flame achieves a finite thickness. Therefore, multidimensional numerical analyses are required to simulate the cool flame formation in a counterflow geometry. In this dissertation, a two-dimensional (2D) axisymmetric multi-physics numerical framework has been proposed to simulate the opposed flow diffusion flame configuration operating in the low-temperature cool flame regime. An OpenFOAM (Open-source Field Operation And Manipulation) based reacting flow solver has been utilized for this purpose. The goal is to understand the effect of multidimensional transport in the formation of cool flame in counterflow geometry and its deviation from ideal conditions. The 2D-axisymmetric model prediction has been found to be in better agreement with the experimental measurements compared to the quasi-1D model prediction. One of the critical findings of this study is identifying the Richardson number as a key parameter to characterize the system. The strain rate required to establish a cool flame is lower in comparison to that of a hot flame. At a lower strain rate, the competition between flow inertia and buoyancy dictates the location of the stagnation plane of the opposing jets and the consequent flame location. The proposed model has been able to capture velocity perturbation at the nozzle exits due to the flame without imposing any radial velocity gradient. The extinction limit of the cool flame has been studied in 1, 3, and 5 atmospheric pressure. The extinction limits predicted by the 2D model are found to be higher than the 1D model predictions. The 2D model permits the velocity boundary conditions to be perturbed at the nozzle exits, which allows the flame to sustain higher strain rates.

In the second part of the dissertation, simulation of the hydrothermal flame of methanol oxidation in supercritical water is conducted utilizing the proposed mathematical

model. The high-pressure combustion is an emerging technique for improving thermodynamic efficiency and reducing harmful contaminants. Additionally, recent studies suggest the presence of low-temperature oxidation in high-pressure conditions, making it worth investigating the effects of multidimensional transport on the reacting flow system in these conditions. The simulation results provide insight into the possible multi-dimensional mixing that can lead to low-temperature flames even under supercritical conditions. In this dissertation, it is found that the hydrothermal flame exhibits different flame structures depending on the fuel loading. For a higher fuel loading (X_F=0.12), a classic non-premixed flame was observed with a peak temperature of ~~2000K. Whereas, for the leanest case studied (X_F=0.071), a peak temperature of ~1200K was observed with extremely low hydroxyl OH concentration (ranging to a few ppm levels). It is difficult to conclude if it is a hot flame or a reduced-temperature flame phenomenon due to partial oxidation processes. Additionally, it was observed that the flame structure is determined by the balance between convective and diffusive flux, which is dictated by the fuel loading. For high fuel loading, the flame forms on the jet periphery, while as the fuel loading decreases, the flame is observed to be lifted in the radial direction. At lower fuel loading, radial mixing is more prominent, and the multidimensional effect appears to be significant.

TABLE OF CONTENTS

LIST OF TABLES

LIST OF FIGURES

LIST OF ABBREVIATIONS

CDS.....Central Differencing Scheme

CFD.....Computational Fluid Dynamics

CFL.....Courant-Frederichs-Lewy

CNES.....National Centre for Space Studies (France)

DME.....Dimethyl Ether

EOS.....Equation of State

EPA.....Environmental Protection Agency

FVM.....Finite Volume Method

GHG.....Greenhouse Gas

HCCI.....Homogeneous Charge Compression Ignition

HRR.....Heat Release Rate

IEA.....International Energy Association

ISS.....International Space Station

KHP.....Ketohydroperoxide

LTC.....Low Temperature Combustion

MeOH.....Methanol

NASA.....National Aeronautics and Space Administration

NTC.....Negative Temperature Coefficient

PBiCGStab.....Stabilized Preconditioned (bi-)conjugate Gradient

PISO.....Pressure-Implicit with Splitting Operator

RCM.....Rapid Compression Machine

RCCI .....Reactivity-controlled Compression Ignition

SCWO ..... Supercritical Water Oxidation

SIMPLE ..... Semi-Implicit Method for Pressure Linked Equations

UDS.....Upwind Differencing Scheme

WCHB..... Wall-cooled Hydrothermal Burner

CHAPTER 1: INTRODUCTION

1.1 BACKGROUND And MOTIVATION

Despite the resurgence of renewable energy technology in recent years, fossil fuel remains the automatic choice of power production and transportation systems (ground, marine, and aviation) due to their extraordinary energy density compared to other sources of energy (Fig. 1.1). According to recent data from International Energy Association (IEA), around 80% of the world's energy production comes from fossil fuel combustion, as presented in Fig. 1.2. The dependence on fossil fuel and energy conversion via combustion will continue in the near future as the global energy demand is expected to grow more than 20% over the next two decades [2].

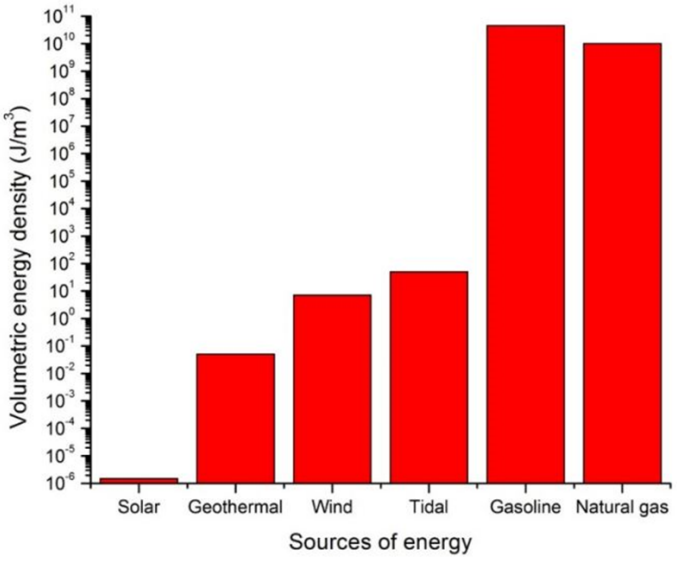

Figure 1.1 Comparison of energy density for different energy sources [3]

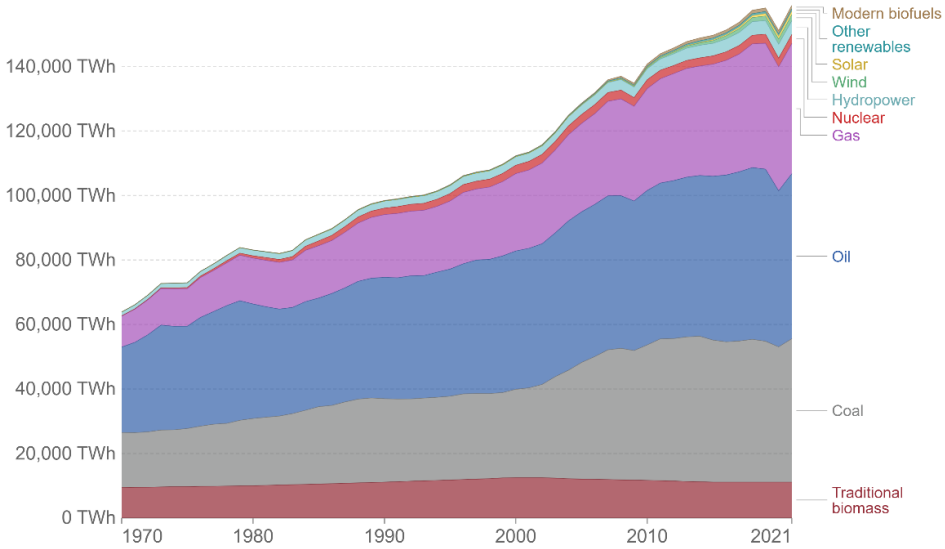

Figure 1.2 World total energy supply by source in Terawatt-hour (TWh), 1970-2021 [4].

Combustion technology is often scrutinized for contributing to harmful emissions, posing detrimental effects on the environment and human health. According to the U.S. Environmental Protection Agency (EPA), fossil fuel combustion (burning) for energy accounted for 74% of total U.S. greenhouse gas (GHG) emissions in 2019, as shown in Fig. 1.3. Therefore, modern combustion research simultaneously seeks higher conversion efficiency and lower emission to meet the increasing regulatory constraints.

To mitigate the two-fold challenges (i.e., efficiency and emission), next-generation engine development efforts have focused on alternative techniques for cleaner engine combustion and power cycle. In this avenue, reduced/low-temperature flame formations have been a topic of great research interest. In the last two decades, significant developments have been made in clean combustion strategies that involve reduced flame temperature, such as homogenous charge compression ignition (HCCI) [5, 6], partially

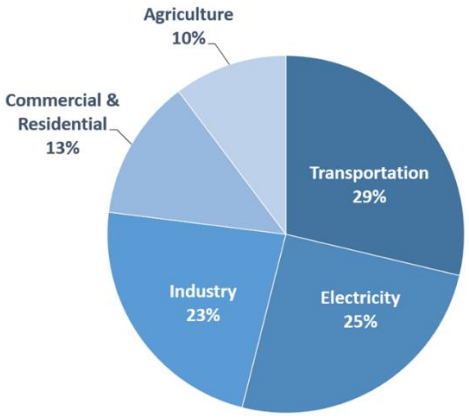

Figure 1.3 U.S. GHG emissions by economic sector, 2019 U.S. EPA [7]

premixed compression ignition (PPCI) [8], and reactivity-controlled compression ignition (RCCI) [9, 10]. For example, Kokjohn et al. [9] demonstrated that compared to conventional diesel combustion, RCCI results in reduction in NO_x by nearly three orders of magnitude, six times lower soot, and ~17% higher gross indicated efficiency. However, these novel combustion techniques come within the trade-off between efficiency and emission parameters. For example, HCCI combustion can achieve higher thermal efficiency (~40%) [11, 12] than a conventional SI engine (~30%) [13]. HCCI also produces less NO_x compared to SI engines, but HC and CO emissions are higher due to the partial oxidation process. Sudheesh and Mallikarjuna [14] showed that CO emission from HCCI combustion could be ~65% higher than a SI engine. Historically, fundamental insights regarding combustion dynamics are studied in standardized canonical settings such as shock tubes [15], rapid compression machines (RCM) [16], flow reactors, jet-stirred reactors (JSR) [17], burner stabilized premixed flame [18] and opposed/counterflow diffusion flame [19]. Although these idealized canonical experiments are far from practical combustion scenarios, they offer unique opportunities to independently study ignition,

flame formation, species evolution, and associated chemical kinetics. For instance, shock tubes and rapid compression machines are used to measure ignition delay time and time-resolved speciation profile, whereas jet-stirred reactors and flow reactors provide species evolution. A well-defined burner stabilized premixed flame is typically studied to investigate flame speed (i.e., burning velocity), heat release, and emission characteristics, while a counterflow burner offers the opportunity to study the flame strength (i.e., extinction limit) for both premixed and non-premixed oxidation. Besides, these idealized experiments can be modeled with simple zero or one-dimensional assumptions. So, the numerical modeling and computational efforts become tractable and inexpensive. Hence they can be utilized to benchmark the chemical kinetic models for the oxidation of different fuels [20, 21].

Historically, idealized experiments and associated numerical modeling have been widely limited to the study of hot flames. Investigations on reduced flame temperature-based novel combustion strategies often encounter rigorous challenges under these canonical configurations. For instance, Mittal et al. [22] investigated the validity of the zero-dimensional approach in modeling RCM experiments of n-heptane oxidation under conditions of two-stage ignitions and negative temperature coefficient (NTC) response. Based on the comparison of the two-dimensional CFD simulations and zero-dimensional (0-D) calculations over the entire NTC regime, they reported that the 0-D calculations accurately predict the first-stage ignition delays but result in a higher pressure rise in the first-stage ignition and consequently a smaller total ignition delay time. This discrepancy was attributed to the multidimensional effect caused by the roll-up vortex, non-uniform heat release, and piston cervice inside an RCM. In their work on the ignition of syngas-air

and hydrogen-air mixtures at low temperatures, Dryer and Chaos [23] reported that two-stage ignition phenomena exhibit many multidimensional characteristics, which leads to discrepancies up to several orders of magnitude between predictions and measurements. Similarly, a widely used one-dimensional model to simulate a counterflow burner can reasonably predict hot flame extinction characteristics. However, it shows significant disagreement with the experimental measurement of the low-temperature flame [24, 25] because the flow conditions (i.e., Reynolds number) and the flame structure (finite flame thickness) make the 1-D assumptions questionable.

Therefore, there is a need for multidimensional numerical studies for the reacting flow systems to complement- a) low-temperature flame modeling, b) identify the source of non-ideality triggered by multidimensional transport, and c) improve fundamental understanding of flame dynamics in these arrangements by obtaining critical insights into these combustion regimes. This dissertation delves into the multidimensional reacting flow modeling that can improve the fundamental knowledge of these low-temperature combustion systems where the effects of multidimensional transport are and can be significant.

1.2 OBJECTIVES

The dissertation focuses on the development of multidimensional, multi-physics models to study combustion phenomena in non-idealized scenarios. The objectives are as follows:

- Assemble a multi-physics mathematical model composed of coupled mass, momentum, enthalpy, and species transport to study chemically reacting flow systems. Utilize the proposed numerical framework to simulate cool

flame/low-temperature combustion in the canonical counter flow configuration.

- Investigate the non-ideality of counterflow flame configurations under low-temperature combustion conditions.
- Assemble a multi-physics mathematical model to simulate combustion under supercritical pressure conditions.
- Simulate hydrothermal flame of methanol combustion by incorporating multi-step chemistry in the reacting flow model and investigate the potential/possible low-temperature flame in supercritical water medium.

1.3 ORGANIZATION OF THE DISSERTATION

The existing knowledge gap regarding reduced-temperature flame modeling and the role of multidimensional transport was the intrinsic motivation to pursue this work. The dissertation is organized as follows:

Chapter 1 introduces the background and scope of this study from a global perspective and then narrows it down to specific problem statements that this work intends to pursue.

In chapter 2, the categorical descriptions of the mathematical framework for the modeling of reacting flow system have been presented. The conservation equations for mass, momentum, enthalpy, and chemical species transport are provided. The details of the calculation procedures of transport properties are discussed. The deviation of ideal gas behavior at high-pressure system has been discussed. The real gas equation-of-state has been described.

Chapter 3 provides a detailed description of numerical methodologies implemented to develop the simulation framework for reacting flow system. First, the finite volume method (FVM) is presented briefly. The numerical schemes and interpolation methods are presented. Finally, the solution algorithm for the transient coupled multi-physics multidimensional numerical model utilized in this study is described.

In chapter 4, simulations of counterflow diffusion flame formation are articulated. It first discusses the historical development of quasi-one-dimensional theory to model counterflow flame and its inadequacy in simulating cool flame formation. The specific counterflow geometry and computational domains used in this study are described in detail. This chapter provides results and analyses from the simulations of dimethyl ether cool flame formation under sets of parametric conditions (i.e., fuel loading and global strain rate, Reynolds number, and Richardson number). The flame structure and extinction characteristics have been studied for atmospheric and high-pressure conditions.

Chapter 5 presents the details of problem schematics and computational domains for the simulation of methanol hydrothermal flame combustions. The flame structure of the methanol flame in supercritical water medium has been investigated for different fuel loading conditions. The importance of multi-step chemistry and real gas behavior has been discussed. This chapter articulates the role of fuel loading on flame structures. The effect of the chemical kinetic parameters is also discussed.

Finally, chapter 6 provides the summary and conclusion of this dissertation, highlighting the major contribution. This chapter serves as the closure of the dissertation by providing recommendations for future research in this avenue.

CHAPTER 2: MATHEMATICAL FRAMEWORK OF MULTIDIMENSIONAL REACTING FLOW MODEL

2.1 INTRODUCTION

This chapter presents the mathematical model used to simulate the reacting flow system. The two-dimensional axisymmetric model comprises of time-dependent compressible mass, momentum, species, and enthalpy conservation equations. In the first section, the conservation equations are described categorically. Then the details of the calculation procedure of transport properties and chemical source terms are presented. Finally, the applicability of ideal gas law in reacting flow systems has been described, and several equations of state are presented to model non-ideal/real gas behavior.

2.2 CONSERVATION OF MASS, MOMENTUM, AND ENTHALPY

The mass and momentum conservation of a transient compressible flow is described by the following equations:

Conservation of mass:

$$\frac{\partial \rho}{\partial t} + \nabla . \left(\rho \vec{u} \right) = 0 \tag{2.1}$$

where, ρ is the mass averaged density, t is time and $\vec{u}$ is the bulk fluid velocity.

Conservation of momentum:

$$\frac{\partial \left(\rho \vec{u} \right)}{\partial t} + \nabla . \left(\rho \vec{u} \vec{u} \right) = -\nabla p + \nabla . \boldsymbol{\tau} + \rho \boldsymbol{g} \tag{2.2}$$

Where, p is the pressure, and g is the gravitational acceleration. The strain rate tensor is expressed by

$$\boldsymbol{\tau} = \mu\left(\nabla\vec{u} + \left(\nabla\vec{u}\right)^T - \frac{2}{3}\boldsymbol{I}\nabla.\vec{u}\right) \tag{2.3}$$

Where, $\boldsymbol{I}$ is the identity tension and μ is the dynamic viscosity.

Transport of energy is formulated in terms of the total enthalpy as follows:

$$\frac{\partial\left(\rho h\right)}{\partial t} + \nabla.\rho\vec{u}h = -\nabla.\vec{q} + \frac{\partial p}{\partial t} - \dot{q}_{reaction} \tag{2.4}$$

Where, λ is the mixture-averaged heat conductivity, $\dot{q}_{reaction}$ is heat source/sink term for chemical reaction. In this dissertation, the viscous work, radiation, and the Dufour effect are neglected. The total enthalpy h is the sum of sensible enthalpy h_s and chemical enthalpy h_c:

$$h = h_s + h_c = \int_{T_o}^{T} C_p\left(T\right)dT + \sum_{k=1}^{N}\Delta h_{f,k}^0 Y_k \tag{2.5}$$

Where, c_p is the mixture average isobaric heat capacity and $h_{f,k}^0$ is the heat of formation of species k at 298 K. Finally, assuming negligible radiative loss, viscous dissipation, and expressing $\vec{q} = \left(\lambda\nabla T\right)$ and $\dot{q}_{reaction} = \sum_{k=1}^{N} h_k^0\dot{\omega}_k$, the energy equation becomes:

$$\frac{\partial\left(\rho h_s\right)}{\partial t} + \nabla.\rho\vec{u}h_s = -\nabla.\left(\lambda\nabla T\right) - \sum_{k=1}^{N}\nabla.\left(h_{s,k}\vec{j}_k\right) + \frac{\partial p}{\partial t} - \sum_{k=1}^{N} h_k^0\dot{\omega}_k \tag{2.6}$$

Where, λ are mixture heat conductivity and $\dot{\omega}_k$ is the chemical source/sink term for species k. The calculation of the chemical source term is presented later in this chapter. After the energy equation is solved, the temperature is recovered from the enthalpy and the specific heat ($T = h/c_p(T)$). Since the specific heat is a function of the temperature, a

numerical method is required to find a solution for the temperature. This is iteratively solved by employing the Newton's method [26]:

$$T^{n+1} = T^n + \frac{(h_{calculated} - h\left(T^n\right)}{c_p\left(T^n\right)} \tag{2.7}$$

Where, n is the iteration number, $h_{calculated}$ is the new enthalpy solved by the energy equation, $h(T^n)$ and $c_p(T^n)$ are the enthalpy based on previous solution, T^n. The iteration is continued until a relative tolerance of 0.05 is reached.

2.3 Conservation of Chemical Species

The transport of chemical species is described as follows:

$$\frac{\partial\left(\rho Y_k\right)}{\partial t} + \nabla.\left[\rho\left(\vec{u} + \vec{u}_c\right)Y_k\right] = \dot{\omega}_k - \nabla.\vec{j}_k, k = 1,2,\ldots N-1 \tag{2.8}$$

Where, Y_k is the mass fraction of species k and $\dot{\omega}_k$ is its chemical source term, N is the number of species. The diffusive mass flux $\vec{j}_k$ is derived from the expression applying mixture-averaged diffusion:

$$\vec{j}_k = -\rho D_{m,k}\nabla Y_k - Y_k \rho D_{m,k}\frac{1}{\bar{M}}\nabla\bar{M} \tag{2.9}$$

Where, $\bar{M}$ is the mean molecular weight, $D_{m,k}$ is the molecular diffusivity of species k which can be calculated from the following expression:

$$D_{m,k} = \frac{1 - Y_k}{\sum_{j \neq k}\frac{X_j}{D_{j,k}}} \tag{2.10}$$

Where, X_j is the mole fraction of species j and $D_{j,k}$ is the binary diffusion coefficient determined from Chapman-Enskog theory [27] to resolve non-unity Lewis number conditions.

2.4 CHEMICAL SOURCE TERM CALCULATION

The chemical source term, $\dot{\omega}_k$, for species and energy transport is calculated as follows:

$$\dot{\omega}_k = M_k \sum_r (\nu''_{k,r} - \nu'_{k,r}) \left(\dot{r}'_r - r''_r \right) \tag{2.11}$$

$$\dot{r}_r = k_r \prod_k C_k^{e_{k,r}} \tag{2.12}$$

$$k_r = A_r(T) \exp\left(-\frac{E_{a,r}}{RT} \right) \tag{2.13}$$

where, $k_r, A_r, \beta_r \; and \; E_{a,r}$ are the rate constant, pre-exponential factor, empirical parameter, and activation energy for the r[th] reaction respectively. $\dot{r}_r$ is the total rate of production, ν is the stoichiometric coefficient and $C_k = \frac{Y_k}{M_k} \rho$ is the molar concentration of species k.

In equations 2.16 through 2.18, superscripts '/' and '//' stand for forward and backward reactions, respectively, and subscripts '*r*' and '*k*' stand for reaction and species, respectively. The parameters $k_r, A_r, \beta_r \; and \; E_{a,r}$ are read from the chemical kinetic model file provided.

2.5 TURBULENCE MODELING

For resolving the turbulence effects a $k-\epsilon$ model has been used with recommended value of 0.9 for Pr_t [28]. The turbulence kinetic energy, k and its rate of dissipation, ϵ , are obtained from the following transport equations:

$$\frac{\partial}{\partial x_i} \left(\rho k u_i \right) = \frac{\partial}{\partial x_j} \left[\left(\mu + \frac{\mu_t}{\sigma_k} \right) \frac{\partial k}{\partial x_j} \right] + G_k - \rho \epsilon \tag{2.14}$$

$$\frac{\partial}{\partial x_i} \left(\rho \epsilon u_i \right) = \frac{\partial}{\partial x_j} \left[\left(\mu + \frac{\mu_t}{\sigma_\epsilon} \right) \frac{\partial \epsilon}{\partial x_j} \right] + C_{1\epsilon} \frac{\epsilon}{k} G_k - C_{2\epsilon} \frac{\rho \epsilon^2}{k} \tag{2.15}$$

where G_k is the turbulent kinetic energy generation term due to velocity gradient and is expressed as:

$$G_k = -\rho\overline{u_i' u_j'}\frac{\partial u_j}{\partial x_i} \tag{2.16}$$

Turbulent viscosity, μ_t is defined as

$$\mu_t = \frac{\rho C_\mu k^2}{\epsilon} \tag{2.17}$$

The model constants have the following values [29]:

$$C_{1\epsilon} = 1.44, C_{2\epsilon} = 1.92, C_\mu = 0.09,\ \sigma_k = 1.0, \sigma_\epsilon = 1.3 \tag{2.18}$$

2.6 EQUATION OF STATE

To close the system of partial differential equations (Eq. 2.1, 2.2, 2.9, 2.13) for the compressible reacting flow simulation, the relation of pressure, density, and temperature is derived from the equation of state. The equation of states for the ideal and non-ideal gas are described in this section.

2.6.1 IDEAL VS. NON-IDEAL GAS

An ideal gas is a gas that behaves according to the ideal gas law (i.e., $pV=R_uT$), where R_u is the universal gas constant. According to Boyle's law, the product of pressure (p) and volume (V) is a constant at any given temperature(T). The fundamental assumptions of the ideal gas are i) the volume of gas molecules is negligible compared to the total volume of the system, ii) particles participate in perfectly elastic collisions, and iii) the system is dilute, so the particles do not interact with each other except to collide. These assumptions become invalid under one or both of these physical conditions: i) very high pressure and ii) very low temperature [30].

Real gases show deviations from the perfect gas law because molecules interact with one another. As illustrated in Fig. 2.1, repulsive forces are significant when molecules are in close contact. At high pressure, the cumulative volume of gas the molecules become comparable to the total volume of the system; and the short-range interactions become significant. So, the ideal gas assumption becomes invalid. Similarly, at a very low temperature, the gas molecules travel with a very low mean speed, and intermolecular attraction force becomes dominant, resulting in a deviation from ideal gas behavior.

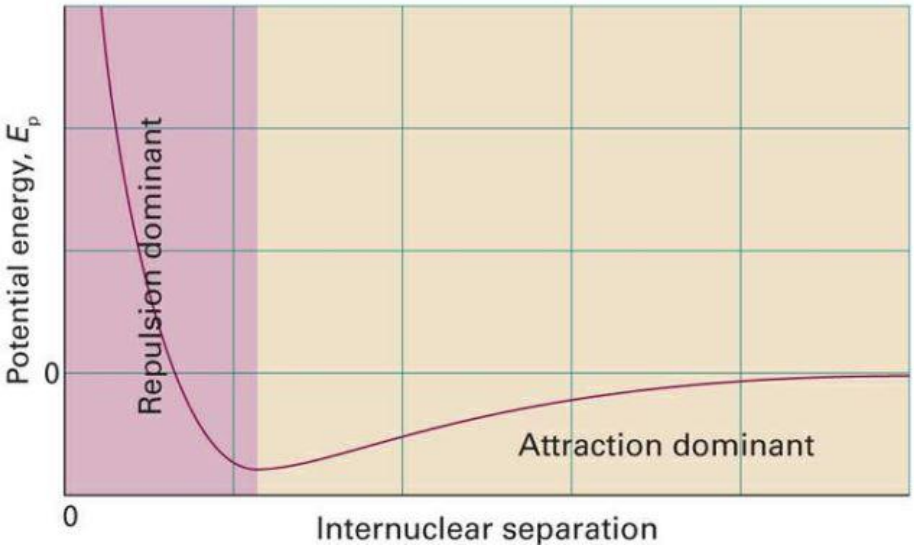

Figure 2.1: The dependence of the potential energy of two molecules on their internuclear separation [30]

The effect of pressure on the non-ideal gas behavior can be further realized by examining the experimental isotherms of carbon dioxide presented in Fig. 2.2. At low pressures, when the system occupies a large volume, the molecules are so far apart for most of the time that the intermolecular forces play no significant role, and the gas behaves perfectly. At moderate pressures, when the average separation of the molecules is only a few molecular diameters, the attractive forces dominate the repulsive forces. In this case,

the gas can be expected to be more compressible than a perfect gas because the forces help to draw the molecules together. At high pressures, the average separation of the molecules is small, and the repulsive forces dominate. The gas can be expected to be less compressible because now the forces help to drive the molecules apart. In other words, at a very high pressure the volume of gas molecules is not negligible, and the inter-molecular forces become significant. Both these phenomena make the perfect gas assumptions invalid. So, gas molecules behave non-ideally.

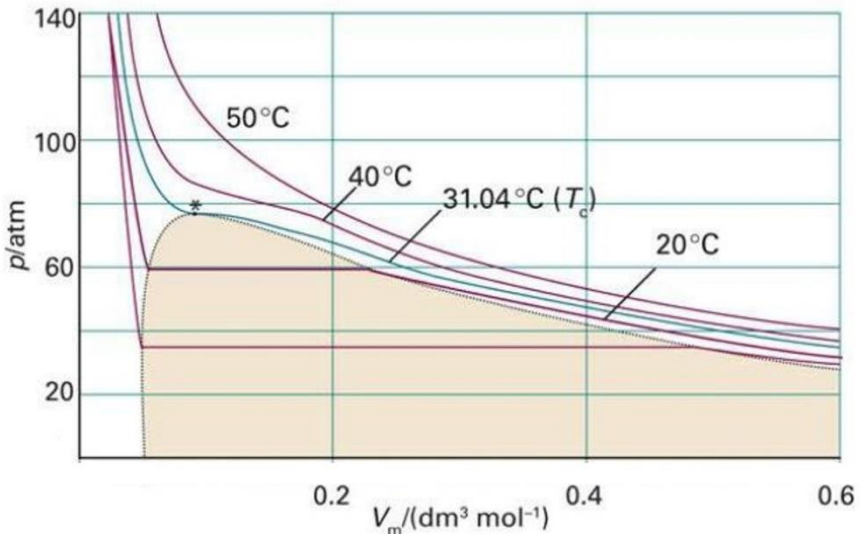

Figure 2.2: Molar volume of carbon dioxide vs. pressure for different temperatures [30]

2.6.2 REAL GAS MODELING

At supercritical conditions, there is a significant deviation from ideal gas behavior. Hence a suitable equation of state (EOS) is required that relates pressure, temperature, and specific volume of fluid at that condition. There are several models of real gas EOS, among which cubic form of equation states has been most widely used in the combustion research community in recent years [31]. Zhu and Reitz [32] proposed that a general form of a cubic equation of state can be expressed as:

$$p = \frac{RT}{V-b} - \frac{a}{V^2 + qbV + wb^2} \tag{2.19}$$

Where p is the pressure, T is the temperature, V is the volume, R is the universal gas constant, w and q are constants that depend upon the type of cubic EOS. In this study, Peng-Robinson (PR) cubic EOS [33] has been implemented to model the hydrothermal flame in the supercritical reactor. The parameters associated with PR-EOS are listed below:

$$q = 2,\ w = -1 \tag{2.20}$$

$$b = \frac{0.07880 RT_c}{P_c} \tag{2.21}$$

$$a = \frac{0.45724 R^2 T_c^2}{P_c}\left[1 + \kappa\left\{1 - \left(\frac{T}{T_c}\right)^{0.5}\right\}\right]^2 \tag{2.22}$$

$$\kappa = 0.37464 + 1.5422\omega - 0.26992\omega^2 \tag{2.23}$$

Where T_c, P_c and ω represent critical temperature, critical pressure, and acentric factor of the fluid, respectively. For multi-component system, Peng and Robinson [33] proposed a binary mixing rule to calculate a and b:

$$a = \sum_{i,j} x_i x_j a_{ij} \tag{2.24}$$

$$b = \sum_i x_i b_i \tag{2.25}$$

$$a_{ij} = \left(1 - \delta_{ij}\right) a_i^{0.5} a_j^{0.5} \tag{2.26}$$

Where δ_{ij} is an empirical binary interaction coefficient associated with the interaction between component i and j.

Several methods [34, 35] have been proposed in the literature to determine the critical properties of molecules and radicals from their intermolecular potential parameters. For example, Zheng et al. [31, 36] provided a thorough outline to calculate the critical properties of individual species from their intermolecular potential data provided in transport data in CHEMKIN format. For the computation of the critical properties of a real-gas mixture, we have employed a pseudocritical method [37, 38]. Pseudocritical rules provide a means to determine reduced properties for mixtures from the corresponding state properties of the individual species. The simplest form of calculating the pseudocritical constants C_{cm} for a real gas mixture can be expressed as:

$$C_{cm} = \sum_{i=1}^{k} x_i C_{ci} \tag{2.27}$$

Where, x_i is the mole fraction of component i, k is the number of components, and C_{ci} is the critical constants (temperature, pressure, specific volume or acentric factor) of the component i.

CHAPTER 3: NUMERICAL MODELING

3.1 INTRODUCTION

The conservation equations described in Chapter 2 are numerically solved in a coupled manner by the finite volume method (FVM) approach. The FVM is a discretization technique for partial differential equations that uses volume integral formulation of the problem with a finite partitioning set of control volumes (cells) [39-41]. In this chapter, a brief description of the FVM method is presented. The numerical methods for resolving the unsteady problem via time integral are then discussed. Finally, a general solution algorithm for the sets of discretized equations is presented.

3.2 FINITE VOLUME METHOD (FVM)

In the FVM approach, the computational domain is divided into a finite number of adjoining control volumes (i.e., cells). Fig. 3.1 shows two control volumes with centers P and N, connected through face f. $\mathbf{S_f}$ represents the direction normal to the face outward of the control volume with center P. The conservation equations are applied to each cell in integral form. First, let us consider a general transport equation presented below:

$$\underbrace{\frac{\partial}{\partial t}(\rho\phi)}_{\text{Transient term}} + \overbrace{\nabla.(\rho\mathbf{u}\phi)}^{\text{Advection term}} = \underbrace{-\nabla.(\lambda\nabla\phi)}_{\text{Diffusion term}} + \overbrace{q'''}^{\text{Source term}} \tag{3.1}$$

where, ϕ, λ and q''' are the conserved variable, transport coefficient, and volumetric source term, respectively. Integrating over the stationary parts of the transport equation and transforming the volume (V) integral of the divergence term to surface (S) integral using Gauss's divergence theorem [42], we get:

$$\int_S \rho\phi \mathbf{v}.d\mathbf{S} = \int_S \lambda \nabla \phi.d\mathbf{S} + \int_V q'''dV \tag{3.2}$$

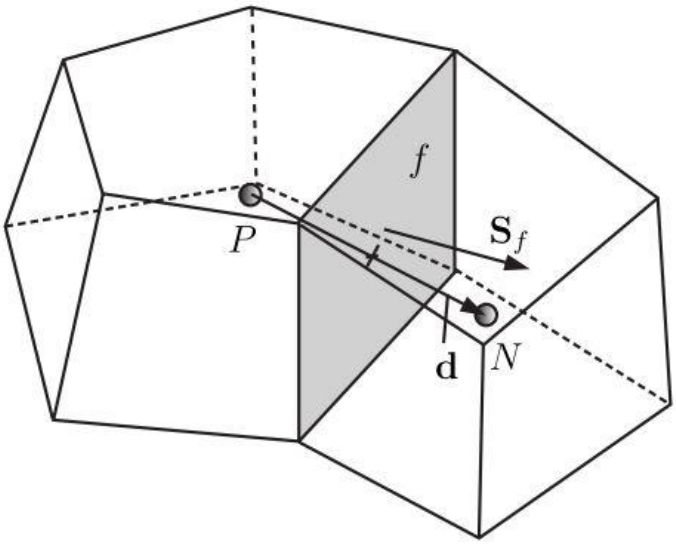

Figure 3.1: Schematic representation of two adjacent cells with FVM discretization parameters.

3.2.1 Approximation of Surface Integrals

The integrals need to be approximated to form the algebraic equation for the control volumes. The next flux through the control volume boundary can be obtained by adding the integral over the volume faces together:

$$\int_S \mathbf{w}.d\mathbf{S} = \sum_k \int_{S_k} \mathbf{w} d\mathbf{S}_k \tag{3.3}$$

where, ***w*** represents the vector form of the convective or the diffusive shown the integral form of the control volume equation.

3.2.2 APPROXIMATION OF VOLUME INTEGRAL

Source terms in the transport equations require integration over the volume of the cell. The simplest second-order approximation can be obtained by replacing the volume integral by the product of the mean value of the integrand, which is approximated as the value at the center of the control volume:

$$\int_V q''' dV = \bar{q}\Delta V \approx q_p \Delta V \tag{3.4}$$

where, q_p is the value of q at the cell center. This quantity is easily calculated; since all variables are available at node P, no interpolation is necessary. The above approximation becomes exact if q is either constant or varies linearly within the cell. Different higher order approximations can be found in [41]. The second-order approximation is employed in this dissertation work.

3.2.3 INTERPOLATION SCHEMES FOR FACE AND CELL-CENTER VALUES

The approximations to the integrals require the values of variables at locations other than computational nodes (cell centers). The value of ϕ and its gradient normal to the cell face at one or more locations on the cell surface are needed to calculate the convective and diffusive fluxes. Volume integrals of the source terms may also require these values. They have to be expressed in terms of the nodal values by interpolation. There are several interpolation schemes that can be derived. For brevity, the two most common interpolation schemes, upwind interpolation (UDS) and linear interpolation (CDS) are described here.

In UDS, flux at the face *f*, ϕ_f is approximated by its value at the upstream of *f* using a forward or backward difference approach depending upon the flow direction. Mathematically it can be presented as:

$$\phi_f = \phi_P \ for \boldsymbol{v}.\boldsymbol{S_f} > 0 \tag{3.5}$$

$$\phi_f = \phi_N \ for \boldsymbol{v}.\boldsymbol{S_f} < 0 \tag{3.6}$$

In CDS, ϕ_f at the control volume face center is the linear interpolation between the two nearest nodes:

$$\phi_f = \phi_N \frac{x_f - x_P}{x_N - x_P} + \phi_P \left(1 - \frac{x_f - x_P}{x_N - x_P}\right) \tag{3.7}$$

3.3 TIME INTEGRAL AND OPERATOR SPLITTING

The conserved variables must be integrated over time to solve the time-dependent problem. So, the temporal term in the conservation equations needs to be discretized. The solution of the transient flows is parabolic in time. This means that a conserved variable (e.g., momentum) at a given instant will only influence the solution in the future (i.e., unidirectional influence). Therefore, the solution advances in a marching manner. Let us consider the following first-order ordinary differential equation with an initial condition:

$$\frac{d\phi}{dt} = f(\phi, t); \phi(t_o) = \phi_o \tag{3.8}$$

Integrating over time from $t = t_o$ to $t = t_f$

$$\int_{t_o}^{t_f} \frac{d\phi}{dt} dt = \int_{t_o}^{t_f} f dt \tag{3.9}$$

Or,

$$\phi(t_n) - \phi(t_o) = \int_{t_o}^{t_f} f dt \tag{3.10}$$

Putting the initial condition, we yield:

$$\phi\left(t_f\right) = \phi_o + \int_{t_o}^{t_f} f dt \tag{3.11}$$

An approximation of the integral on the right-hand side is required to calculate the value of ϕ at discrete time values. There are several approaches for temporal discretization in computation fluid dynamics analyses, such as Euler forward (explicit), Euler backward (implicit), leapfrog method, Crack-Nicolson method, etc. In a reacting flow system, different reactions have different time scales. Besides, the discretization of source terms for various species will generate nonlinear terms, which will introduce additional difficulty in the solution procedure and make the system of equations very stiff [43]. To encounter this, Euler backward time schemes are used because of the numerical stability [44]. A necessary condition for the solution convergence is the Courant-Frederichs-Lewy (CFL) condition [45]. It is defined by the Courant number with the following expressions:

$$C_o = \frac{|u|\Delta t}{\Delta x} \leq C_{max} \tag{3.12}$$

In this dissertation, for the simulations conducted in OpenFOAM, C_{max} = 0.1 has been utilized.

In reacting flow systems, the chemical time scales are typically much smaller than the non-reactive physics involved (i.e., flow and heat transfer). Therefore, in the transient simulations, the time step used by the solvers must be small enough to resolve the chemical species conversion (i.e., production and consumption of species via chemical reactions). This makes the simulations computationally expensive. An operator-splitting technique is used to mitigate this challenge [46, 47]. In this technique, the governing equations are split into subdivisions, each having a separate operator to resolve corresponding physics. In the numerical analyses of the reacting flow system, two different time steps are chosen: Δt_{CFD}

and Δt_{chem}, where Δt_{CFD} is the time step taken by the 'non-reactive CFD solver', whereas, within in 'CFD time step' much smaller Δt_{chem} is utilized to integrate the system of chemical reactions. To solve the reaction terms, CVODE solver from SUNDIALS package was coupled with OpenFOAM. SUNDIALS is a library of highly optimized ODE solvers developed by Hindmarsh and coworkers at Lawrence Livermore National Laboratory [48, 49]. At the beginning of each time step, the CVODE solver is used to integrate the state over the CFD time step for each cell and uses methods designed for stiff systems of differential equations. Thereby, much smaller time steps Δt_{chem}, that are adaptively chosen by Sundials, can be used to integrate the system of chemical reactions within the Δt_{CFD}. Details of the implementation of the operator splitting technique in reacting flow numerical code can be found in [50-52].

3.4 SOLUTION ALGORITHM

As mentioned in Chapter 1, this dissertation comprises of numerical investigation of counterflow cool flame and hydrothermal flame formation. For the first part (i.e., counterflow cool flame), a multi-physics numerical model has been assembled in OpenFOAM [53] CFD package coupled with the chemical kinetic solution tool Cantera [54]. For hydrothermal flame simulation, ANSYS Fluent [55] platform coupled with CHEMKIN package[56] has been employed. Details of the coupling between these CFD solvers and the chemical kinetic solvers are discussed in respective chapters for counterflow and hydrothermal flame. In this section, the general fluid flow solution algorithm for OpenFOAM and Fluent are discussed.

3.4.1 ITERATIVE SCHEME FOR TIME-ADVANCEMENT

For time-dependent flows, the discretized form of the generic transport equations are solved iteratively for a given time-step until the convergence criteria are met. Thus, advancing the solutions by one time step typically requires a number of outer iterations, as shown in Fig. 3.2

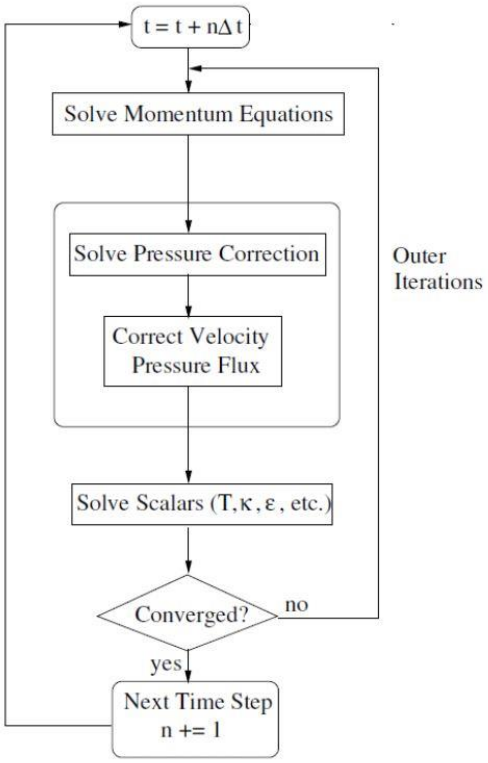

Figure 3.2: Iterative scheme for time advancement [57]

4.4.2 PRESSURE-VELOCITY COUPLING

For simulations of both the counterflow and hydrothermal flame, pressure-based solvers have been utilized to resolve the bulk fluid velocity. A critical part of the solver is the pressure velocity coupling. There are several pressure-velocity coupling methods available in OpenFOAM and ANSYS Fluent. In OpenFOAM reacting flow solver, PISO (Pressure-Implicit with Splitting Operator) algorithm [58, 59] is used. An overview of the

implementation of the PISO algorithm in OpenFOAM fluid flow solver is presented in Fig. 3.3.

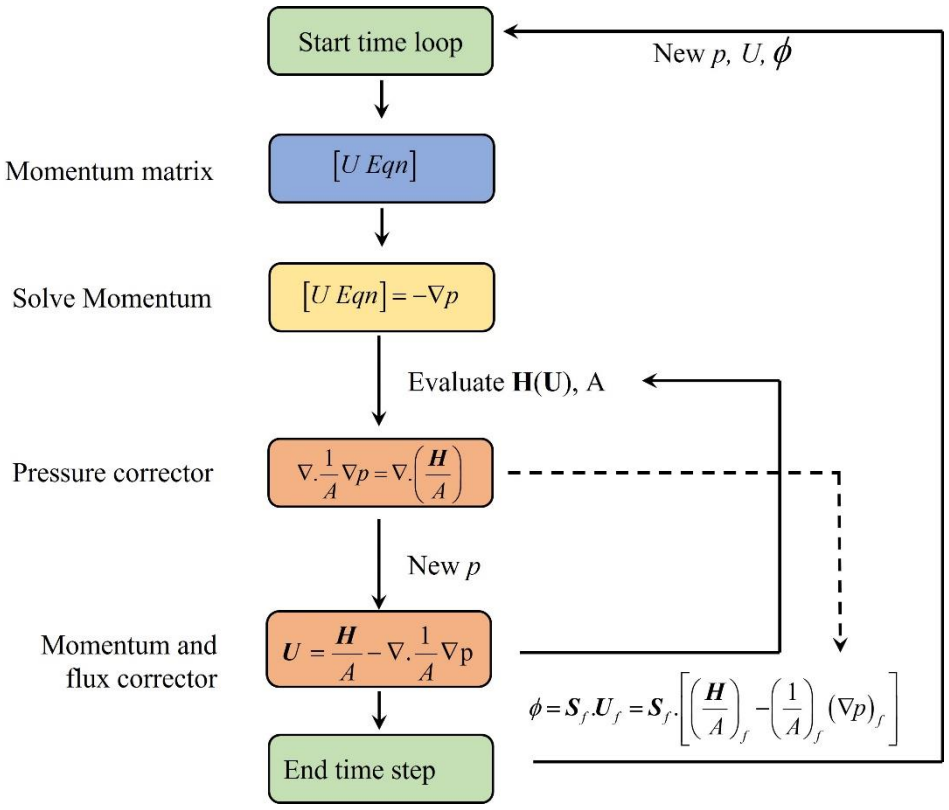

Figure 3.3: Workflow of pressure velocity coupling

In PISO algorithm, first, the momentum equation is written in explicit form, and then all the terms are discretized using the FVM schemes except the pressure term.

$$\frac{\partial \rho \boldsymbol{U}}{\partial t} + \nabla.\left(\rho \boldsymbol{U}\boldsymbol{U}\right) - \nabla.\mu\nabla\boldsymbol{U} = -\nabla p \tag{3.13}$$

$$\left[U\ Eqn\right] = -\nabla p \tag{3.14}$$

where $\left[U\ Eqn\right]$ is the matrix formed by the discretized equation of the momentum equation except the pressure gradient. $\left[U\ Eqn\right]$ can be expressed by the following expression:

$$\left[U\ Eqn\right] = A\boldsymbol{U} - \boldsymbol{H} \tag{3.15}$$

where, A is the diagonal matrix of the $[U\ Eqn]$ and $\boldsymbol{U}$ is the solution of the N-S equation, and $\boldsymbol{H}$ is the residual matrix representing the contribution from the pressure term in the solution. Inserting the expression of $[U\ Eqn]$ in the Eqn. 3.15, multiplying it by (1/**A**) and re-arranging, we get the momentum correction equation as follows:

$$\boldsymbol{U} = \frac{\boldsymbol{H}}{A} - \nabla . \frac{1}{A} \nabla \mathrm{p} \tag{3.16}$$

Taking the divergence of Eqn 3.16 and applying mass continuity ($\nabla . U = 0$), a 'pressure corrector equation' is derived:

$$\nabla . \frac{1}{A} \nabla p = \nabla . \left(\frac{\boldsymbol{H}}{A} \right) \tag{3.17}$$

After the pressure correction, the velocity field should also be corrected. This stage is called the 'momentum and flux correction'. In this step, first, the flux ϕ at the cell faces (*f*) is corrected via following interpolation scheme [60]:

$$\phi = \boldsymbol{S}_f . \boldsymbol{U}_f = \boldsymbol{S}_f . \left[\left(\frac{\boldsymbol{H}}{A} \right)_f - \left(\frac{1}{A} \right)_f (\nabla p)_f \right] \tag{3.18}$$

Finally, the velocity is corrected by adding the calculated pressure gradient to the estimated velocity at the previous step.

$$U_{new} = U_{old} - \frac{1}{A} \nabla p \tag{3.19}$$

The above procedure is repeated until the velocities and pressure satisfy both momentum and mass conservation.

CHAPTER 4: NON-PREMIXED COOL FLAME OF DIMETHYL ETHER (DME) COMBUSTION IN COUNTERFLOW GEOMETRY

4.1 BACKGROUND AND MOTIVATION

The study of low-temperature combustion (LTC) and its relationship to cool flame kinetics has become a major area of research in recent years due to its potential to improve thermal efficiency, increase fuel flexibility, and reduce pollutant emissions in advanced and legacy internal combustion engines [61]. Despite notable laboratory-scale demonstrations, such as homogeneous charge compression ignition (HCCI) [62] and reactivity-controlled compression ignition (RCCI) engines [63]), a lack of fundamental understanding continues to limit the implementation of LTC technology in reciprocating engines and the gas turbine engines [64]. One major limitation in this field is the inadequate understanding of the multidimensional aspects of the oxidation process in the low-temperature regime. This lack of understanding is primarily due to a shortage of multidimensional numerical studies investigating transport-coupled reacting flow systems and associated flame dynamics.

Low-temperature combustion has been investigated in several canonical configurations [65], but among them, opposed/counterflow diffusion flame and microgravity droplet combustion allow studying transport coupled low-temperature kinetics. Ju and coworkers extensively used the opposed flow diffusion flame configuration

to conduct experimental LTC studies for various fuels [24, 66]. Won et al. [19] experimentally demonstrated a self-sustaining cool diffusion flame of n-heptane at the atmospheric condition in counterflow geometry. Further studies have reported the presence of stable, cool flames in pure dimethyl ether (DME) and DME-methane (CH4) blends in both premixed and non-premixed configurations [24, 25]. Recently, Yehia et al. [67] demonstrated the existence of a self-sustaining low-temperature "warm" diffusion flame of dibutyl ether in the form of a "multistage" diffusion flame nestled between a cool and hot flame. Additionally, independent modeling work has been conducted to gain insight into LTC characteristics, with studies such as Law and Zhao [68] investigating the effect of strain rate on cool flame dynamics and concluding that under low and moderate strain rate conditions (i.e., longer residence time), cool flames can form as a result of NTC-affected n-heptane/air oxidation.

Numerical modeling of the counterflow diffusion flame experiments has been mostly centered upon the OPPDIFF module of the CHEMKIN package [56] that considers the arrangements as a quasi-one-dimensional (1D) configuration. The quasi-1D theory was first formally introduced by Seshadri and William [1] and was derived based on two key assumptions:

i) Zero radial gradients of all scalar variables, i.e., they only vary along the axis of symmetry

ii) The flow field can be resolved via a self-similarity solution, i.e., radial component of the velocity can be recovered from a linear self-similarity function along the radial direction (plug flow assumption).

The quasi-1D theory has been validated and well-established for large diameter (typically 25 mm or greater) nozzles and high Reynolds number conditions through a series of experiments conducted by Puri et al. [69, 70], and models developed by Smooke et al. [71]. However, these quasi-1D theory-based numerical models have produced inconsistent predictions when the experiments do not ascertain the radially uniform velocity profile at the nozzle exits. Physical scenarios that lead to deviations from the plug flow assumption include small diameter nozzles, low Reynolds numbers, and finite flame thickness [72]. A contoured converging nozzle with a large area ratio has been proposed to achieve uniform exit velocity for small-diameter nozzles [73, 74]. However, Rolon et al. [75] demonstrated that even a converging nozzle can still result in a non-uniform axial velocity as the nozzle separation distance is gradually reduced, and a critical separation distance is necessary to maintain the near-plug flow condition. It was also shown that for non-ideal conditions, quasi-1D modeling can still be used by imposing a radial velocity gradient at the nozzle exits [76]. Later, Sarnacki et al. [77] experimentally measured the deviation from the plug flow velocity profile for methane, ethylene, and n-butane-air counterflow flames. The measurement showed a dip in the axial velocity profile at the nozzle exit, indicating the presence of a finite radial velocity gradient. They concluded that the quasi-1D model would require experimental measurements as input for accurate velocity boundary conditions in order to simulate counterflow experiments where radial non-uniformity is prominent.

Unlike hot flame, cool flame possesses finite flame thickness due to a thicker reaction zone which has the potential to perturb the velocity profile at the nozzle exits [78-80]. Furthermore, the experiments are typically conducted at a strain rate lower in order of magnitude (i.e., low Reynolds number) compared to the hot flame experiments. Both these

configurations make the underpinning assumption of the quasi-one-dimensional theory questionable. A finite radial velocity gradient (Vr) value can be imposed at the nozzle exits in the one-dimensional simulation to counterbalance this non-ideality in a counterflow cool flame experiment. For example, to simulate their DME cool flames where the global strain rates varied from ~60 s^{-1} to ~120 s^{-1}, Reuter et al. [25] progressively increased the radial velocity gradient to match the cool flame's measured temperature profiles. The radial velocity gradient V_r, which corrects the deviation from the plug flow profile, was increased linearly with the global strain rate. However, the V_r was only imposed on the fuel side boundary condition, whereas the oxidizer side boundary condition was unaltered. A similar approach was taken for dibutyl ether (DBE) flames, but the radial velocity gradient was prescribed on both the oxidizer and fuel stream [67]. While these approaches allowed the numerical investigation to match the measurements to some degree, they do not provide a comprehensive understanding of the underlying coupling between fluid flow and flame dynamics.

Based on the discussion above, one can clearly see a need for the multidimensional assessment of cool flame formation in counterflow geometries. In this study, a self-consistent two-dimensional (2D) axisymmetric reacting flow model has been developed to simulate counterflow cool flame. This research aims to fill the gap in the knowledge of the multidimensional aspects of the oxidation process in the low-temperature regime and to provide a foundation for future numerical modeling studies of reacting flow simulations of cool flame formation.

4.2 FUNDAMENTALS OF THE LOW-TEMPERATURE FLAMES

Whereas ‘cool flame’ was accidentally discovered almost 200 years ago [81], in recent years, there has been renewed interest in this topic due to its importance in controlling engine knock, ignition timing, emissions, and efficiency [65]. Additionally, the discovery of long-duration cool flame burning of isolated droplets on the International Space Station in 2012 has further triggered interest in low-temperature combustion [82]. In order to fully grasp the intricacies of counterflow cool flame, it is crucial to understand the fundamentals of both hot and cool flames, as well as the high and low-temperature chemistry that governs them.

The chemistry that governs the hot flame formation has been extensively studied and established in the literature [83]. The H_2-O_2 chain branching sequence plays a crucial role in dictating high-temperature chemistry. This can be observed by examining the explosion limit of a stoichiometric H_2-O_2 (as depicted in Fig. 4.1). At low pressures, the first explosion limit is determined by the competition

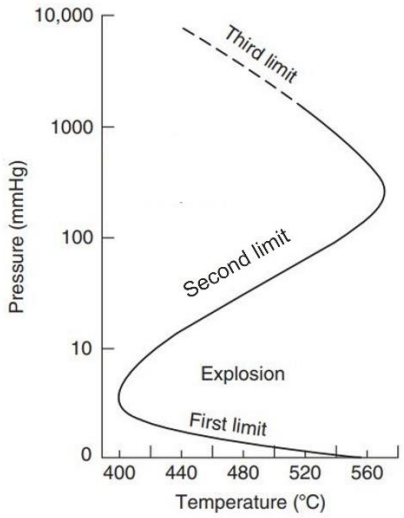

Figure 4.1 Explosion limit of a stoichiometric H_2-O_2 system [84]

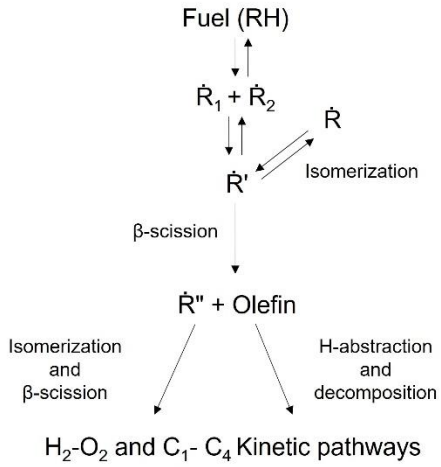

Figure 4.2 General pathway of high-temperature reaction pathway of hydrocarbons (summarized from [84])

between the chain branching reaction H + O_2 = OH + O and radical termination. As pressure increases, the second limit is determined by the competition between the chain-branching reaction H + O_2 = OH + O and the effectively chain-terminating reaction H + O_2 + M = HO_2 + M. At even higher pressures, reactions such as H_2O_2 + M = OH + OH + M and HO_2 + H_2 = H_2O_2 + H become important, leading to the destabilization of HO_2 and the third explosion limit. In summary, the H_2-O_2 system, particularly the reaction H + O2 = OH + O, controls the chain-branching of all hydrocarbons and oxygenates at high temperatures [84]. A brief schematic of the high-temperature pathway is presented in Fig. 4.2.

Low-temperature combustion follows much more complex reaction pathways. [85]. Before presenting the reaction sequence of low-temperature chemistry, it is worthwhile to

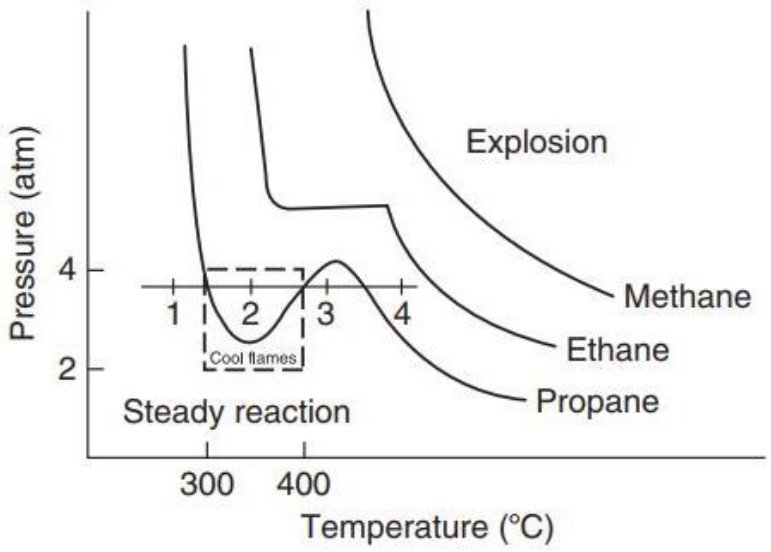

Figure 4.3 General representation of the explosion limits of stoichiometric hydrocarbon-air mixture [84]

to understand the general explosion limit of the hydrocarbons presented in Fig. 4.3. The shift of the curve for larger hydrocarbons can be attributed to their tendency to break down more readily, providing a pool of radicals to initiate fast reactions. The nature of the propane mechanism is different from that of the H_2-O_2 reaction when one compares this explosion curve with the H_2-O_2 pressure peninsula. The dip in the propane-air curve drops and goes slightly to the left for higher-order paraffins [84]. Semenov [86] reported that the negative temperature coefficient (NTC) (denoted by the dashed box in Fig. 4.3) could be illustrated by hypothesizing unstable species that are produced as intermediates and then undergo different reactions according to the temperature. The chemical mechanism used to study this NTC feature of the explosion limit is generally referred to as cool-flame chemistry.

The oxidation of hydrocarbons at low temperatures is governed by a chain-branching sequence known as peroxy chemistry, as illustrated in Fig. 4.4. The oxidation process begins with the abstraction of a hydrogen atom from the fuel molecule (RH) by a

radical, such as OH or HO_2, resulting in the formation of a fuel radical (R). The fuel radicals next combines with O_2 molecule to produce an alkylperoxy radical (RO_2). The RO_2 radical undergoes internal isomerization to form a hydroperoxyl alkyl radical (QOOH). Hydroperoxyl alkyl radical then forms a peroxy hydroperoxyl alkyl radical (O_2QOOH) via a second O_2 addition. Furthermore, QOOH can also decompose to form either one HO_2 radical and an alkene or one OH radical and a cyclic ether. In the main chain-branching sequence, the isomerization and decomposition of O_2QOOH produces ketohydroperoxide (KHP) and an OH radical.

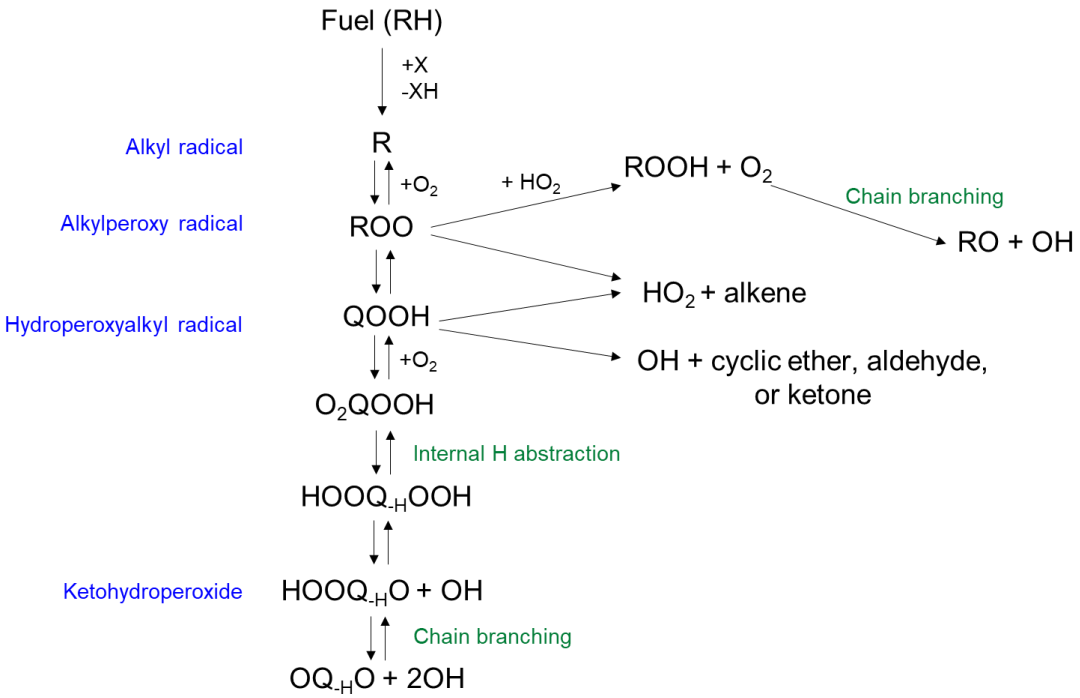

Figure 4.4 Schematic of the general low-temperature chemistry of large hydrocarbons, based on Glassman et al. [84] and Zador et al. [85]. 'X' indicates an oxidizer, or simply O_2, in this description.

The breakdown of KHP leads to the formation of a second OH radical and a ketoalkyloxy radical. Since the pathway from R → RO_2 → QOOH → O_2QOOH → ketoalkoxy radical + 2 OH produces multiple OH radicals, it qualifies as a low-temperature

chain-branching pathway. On the other hand, the reaction pathway from R → RO_2 → QOOH → cyclic ether + OH produces only one active radical, so it qualifies as a chain propagating pathway. The R → RO_2 → alkene + HO_2 produces no active radicals at low temperatures and is a chain-terminating pathway.

The chain-branching pathway dominates at the low temperature. Raising the temperature leads to the reduction of the pressure for the mixture to become explosive, as illustrated in Fig. 4.3. However, as the temperature becomes higher, the chain-propagating pathway (QOOH → cyclic ether + OH), the chain-terminating pathway (RO_2 → alkene + HO_2), and the reaction RO_2 → R + O_2 become more competitive with the chain-branching pathway. Research by Townend [87] has shown that the combination of these effects results in a reduction in the formation of RO_2, the lowered formation of O_2QOOH for branching, and ultimately the formation of the negative temperature coefficient (NTC) regime. The recent work by Farouk and Dryer [88] and Nayagam et al. [89] have confirmed that the cool flame can be sustained due to the existence of this NTC regime.

4.3 FUNDAMENTALS OF COUNTERFLOW/OPPOSED DIFFUSION FLAME

Counterflow configuration provides a unique opportunity to study the premixed and non-premixed flame formation and analyze its thermo-chemical dynamics under the effect of stretch [90]. It was first developed in 1959 by Potter and Butler with pipe/tube flow arrangement to study non-premixed flame formed between two opposing jets [91]. In a subsequent development, Padya et al. conducted a similar experiment but used a conditioning screen/matrix near the nozzle exits to attain a uniform velocity profile [92]. The fundamental idea behind these arrangements (screen/matrix) was to achieve a plug flow velocity profile instead of a parabolic one, so the flow could be characterized as one-

dimensional. These two techniques are referred to as Type I and Type II counterflow burners in the comprehensive review of this topic by Tsuji [93], as illustrated in Fig. 4.5. In a recent development, the near-plug flow has been achieved by introducing contoured converging nozzle in their experiment by Won et al. [19] and Johnson et al. [72].

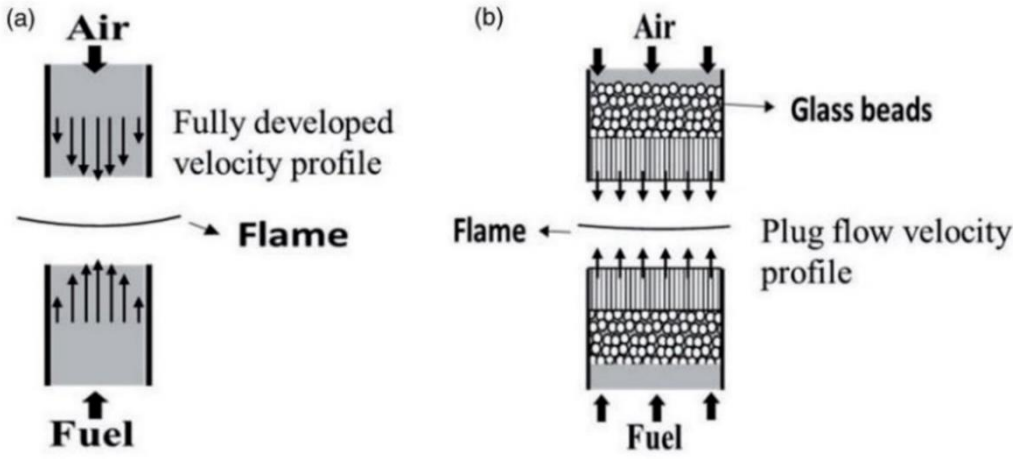

Figure 4.5 a) Type I and b) Type II counterflow burner [94]

Numerical modeling of counterflow flame experiments was initially conducted using the assumption of potential flow, as proposed by Dixon-Lewis et al. [95]. However, later research by Kee et al. [96] found that the plug flow assumption provided a better representation of laminar counterflow experiments. These two assumptions represent the extremes of boundary conditions at the nozzle exits, with potential flow assuming a constant velocity gradient and plug flow assuming a zero-velocity gradient, as illustrated in Fig. 4.6. However, experiments conducted by Chelliah et al. [97] and Sarnacki et al. [77] have shown that depending on the burner configuration parameters such as nozzle separation distance, nozzle diameter, and Reynolds number, the measurements may fall somewhere between the predictions of the plug and potential flow assumptions. In most cases, the measurements tend to be closer to the plug flow limit. In the case of cool flame,

the physical scenario deviates further from the plug flow assumption, as previously discussed.

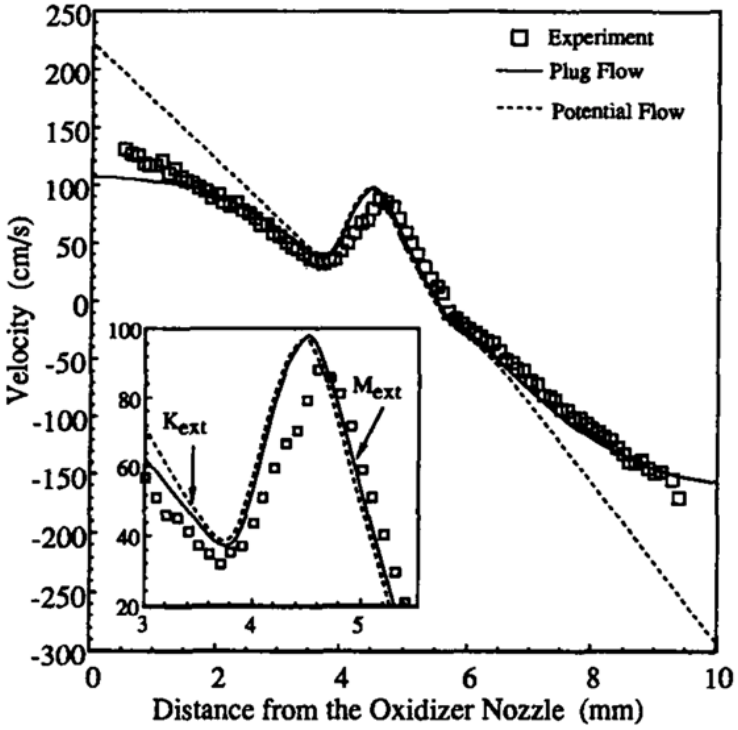

Figure 4.6 Comparison of axial velocity profiles by experimental measurement and model prediction with two extreme boundary conditions (plug and potential flow) for methane-air hot diffusion flame [97].

4.4 RECENT WORKS ON COUNTERFLOW COOL FLAME

The recent finding of cool flame in flame extinguishment (FLEX) experiments conducted on the International Space Station (ISS) has garnered renewed interest in the study of low-temperature chemistry and flame dynamics in counterflow configurations [90]. In their earlier work, Liu et al. [98] used numerical methods to investigate the formation of non-premixed n-heptane ignition in a counterflow configuration at elevated pressure. One of their key findings was that the formation of low-temperature flames under

a counterflow geometry is similar to the negative temperature coefficient (NTC) regime observed in homogeneous systems. Law and Zhao [68] computationally studied the effect of strain rate on counterflow flame formation of n-heptane/air. They concluded that under low and moderate strain rate conditions (i.e., longer residence time), cool flames can be observed due to NTC-affected ignition. A self-sustaining cool diffusion flame of n-heptane was experimentally demonstrated by Won et al. [8] in a counterflow configuration at atmospheric conditions [19]. Subsequently, the cool flame of dimethyl ether has been studied using various techniques, such as with and without ozone [79, 99], with blended methane (CH_4) [25, 100], in both premixed and non-premixed configurations. Recently, a counterflow 'multistage' diffusion flame has been reported by Yehia et al. [67]. Their work demonstrated the existence of a self-sustaining low-temperature 'warm' diffusion flame of dibutyl ether, existing between cool flame and hot flame regime.

The literature on multidimensional numerical analysis of counterflow flame formation is limited. In recent studies, Johnson et al. [72] performed two-dimensional axisymmetric numerical simulations to examine the applicability of the quasi-1D theory under various conditions including nozzle separation distance, global strain rate, and nozzle

(a) (b)

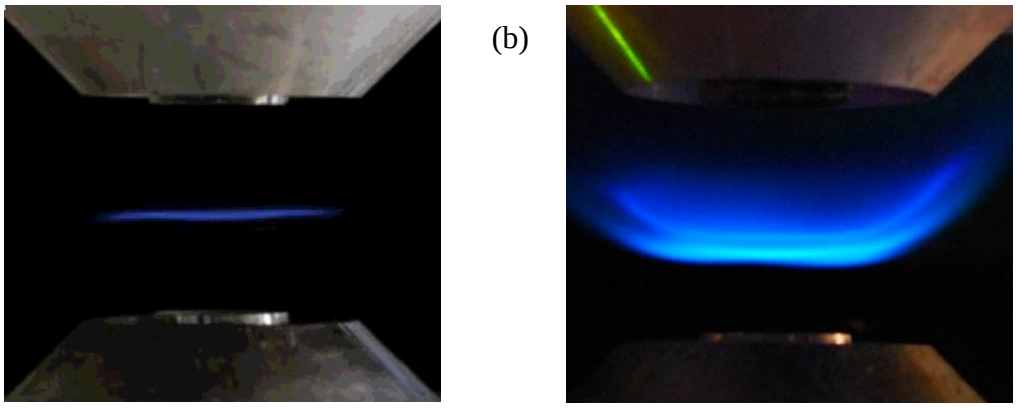

Figure 4.7: Visual image of (a) DME cool flame [25], (b) DBE multistage warm flame [67]

diameter. They found that for nozzle separation distances below the free-floating limit, the quasi-1D formulation could be maintained by prescribing a radial velocity boundary condition if radial gradients were insignificant. However, at low strain rate (<~100 s^{-1}) when the flame is supported by finite rate chemistry (such as low-temperature oxidation), conditions may arise where radial gradients become significant and need to be resolved. Katta and Roquemore [90] analyzed multidimensional aspects of counterflow cool flame of n-heptane shrouded by nitrogen co-flow. They observed that while the flame remained flat near the axis, it tended to show radial asymmetry farther along the radial direction. These findings highlight the need for multidimensional analyses in the study of cool flames in counterflow geometry, as the similarity solution approach based on the quasi-1D theory is inadequate for their analysis.

4.5 CHARACTERISTICS OF DIMETHYL ETHER (DME)

Fossil fuels remain the major energy source for power generation, transportation, and industrial applications worldwide. Crude oil, coal, and natural gas are the primary resources for world energy. In 2021, a daily average of 19.78 million barrels of petroleum was consumed in the U.S., which accounted for more than 20% of global consumption [101, 102]. Projections from the U.S. Energy Information Administration estimate that this consumption will continue to rise by 14% by 2050 [103]. Additionally, with the industrial growth in countries like India, China, and Russia, the world's energy demand is predicted to increase by more than 50% in the next two decades. [104]. This has led to a greater focus on finding substitute energy sources and alternative fuels.

Alternative fuels have been explored as a potential replacement for conventional liquid fuels like diesel and gasoline. While natural gas has been considered a viable option

[105-107], its use in automotive engines has been limited due to inconsistent ignition [108] and variations in gas composition which affect performance and emission [109]. Additionally, natural gas reserves are finite, making it an unsustainable alternative in the long term. Other options such as biofuels (bioethanol, biodiesel, biogasoline), hydrogen, and Fischer-Tropsch fuels have been examined, however, dimethyl ether (DME) appears to have the most potential as an alternative fuel based on its well-to-wheel efficiency and emission characteristics [110, 111].

Dimethyl ether (DME) is an odorless, non-toxic compound with a chemical formula of CH_3OCH_3. DME is highly flammable in ambient conditions and can be produced from coal and biomass via syngas [111, 112]. Due to the absence of a direct carbon-to-carbon bond, DME combustion is associated with low HC, CO, and NO_x emissions [113]. DME has a cetane number of ~55 (diesel: 40-50). Hence, it is considered a clean alternative to petroleum diesel fuel [111, 114, 115]. Furthermore, DME exhibits prominent negative temperature coefficient (NTC) characteristics with relatively tractable chemical kinetics [116, 117].

An overview of DME oxidation scheme is presented in Fig. 4.8. At low temperatures, methoxymethyl radicals (CH_3OCH_2) form an adduct methoxymethyl-peroxy radical ($CH_3OCH_2O_2$) with molecular oxygen. This adduct goes through an isomerization process to form hydroperoxyl methoxymethyl radical ($CH_2OCH_2O_2H$/QOOH), which can undergo β-scission producing two formaldehyde molecules and a hydroxyl radical ($CH_2OCH_2O_2H \rightarrow OH + 2CH_2O$). In addition, it can also form a peroxy-methoxymethyl-hydroperoxide radical ($O_2CH_2OCH_2O_2H$/O_2QOOH) by reacting with molecular oxygen. The peroxy-methoxymethyl-hydroperoxide goes through an isomerization process and

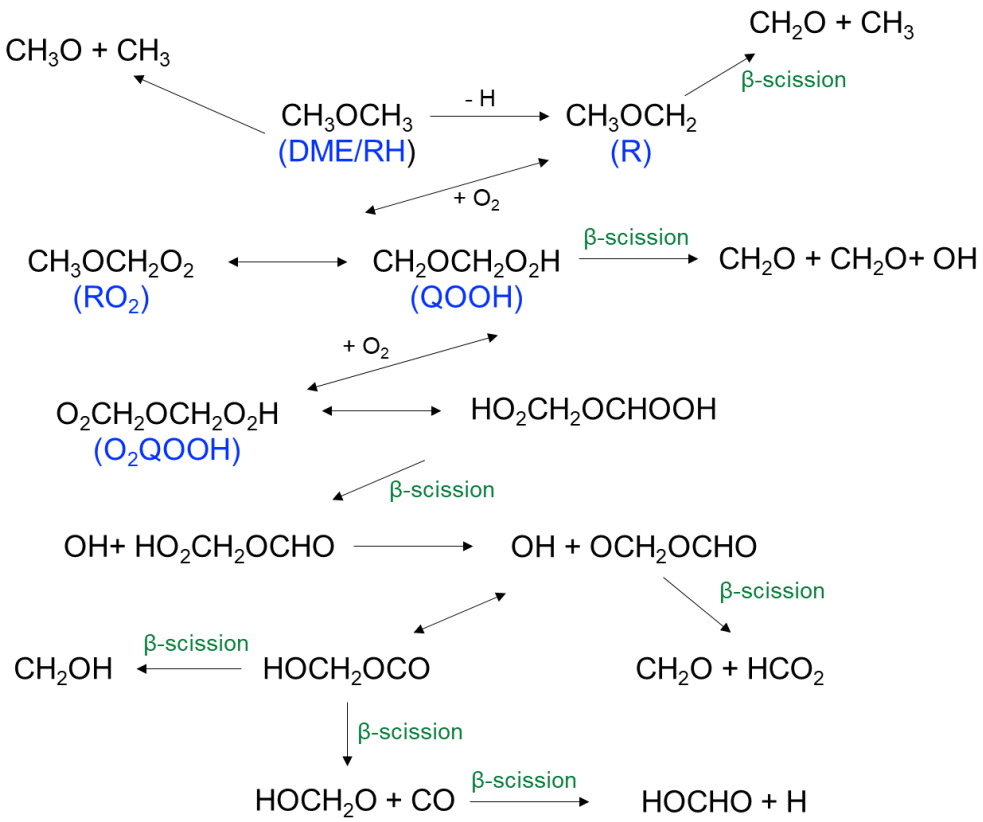

Figure 4.8: Chemical kinetic scheme for DME oxidation (summarized from Curran et al. [116])

produces one carbonyl-hydroperoxide molecule (HO_2CH_2OCHO) and one hydroxyl (OH) radical ($O_2CH_2OCH_2O_2H$ → HO_2CH_2OCHO + OH). The carbonyl-hydroperoxide molecule then decomposes into OCH_2OCHO molecule and another reactive hydroxyl radical (HO_2CH_2OCHO → OCH_2OCHO +OH). At temperature above ~600K, the β-scission of the hydroperoxyl methoxymethyl radical (QOOH) is more dominant, and the reactivity of the system decreases since only one reacting hydroxyl (OH) is formed in this pathway (in contrast to the release of two OH radicals through the isomerization of the peroxy-methoxymethyl-hydroperoxide, i.e., O_2QOOH). This leads to the negative temperature coefficient (NTC) region and the formation of low-temperature flame [118].

Due to this prominent NTC characteristic, DME is a very suitable candidate for studying cool flame formation.

4.6 SCHEMATIC OF THE PROBLEM GEOMETRY

The counterflow geometry for the numerical study is based on an existing experimental setup developed at Princeton University to investigate opposed-flow flames in different temperature regimes [19, 25, 119, 120]. In this work, we have simulated the counterflow cool flame experiments conducted by Reuter et al. [25] for dimethyl ether combustion. The schematics of the experimental setup and computational geometry are presented in Fig. 4.9 and 4.10, respectively. The counterflow burner consists of two opposing nozzles (1.3 cm in diameter) with a separation distance of 2.25 cm. Heated fuel and nitrogen (550 K) are ejected from the upper nozzle to meet an oxidizer jet (300K) coming from the lower nozzle. Both the nozzles are surrounded by outer nitrogen co-flow at their respective temperature and velocity (co-flow nozzle diameter 2.2 cm). The computational domain extends further downstream to capture the flame structure in the radial direction and to ensure minimal outlet effect on the solution.

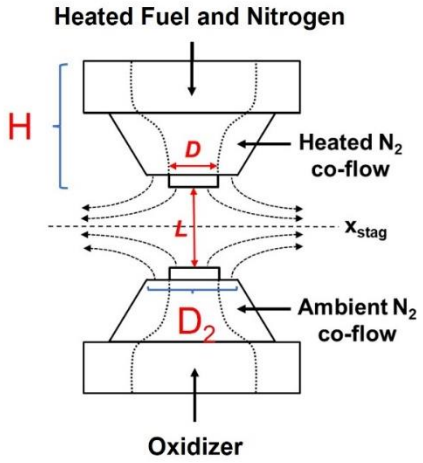

Figure 4.9: Schematic of the experimental setup [25]. L = 2.25 cm, D = 1.3 cm, D_2 = 2.2 cm, and H = 6.08 cm [25]

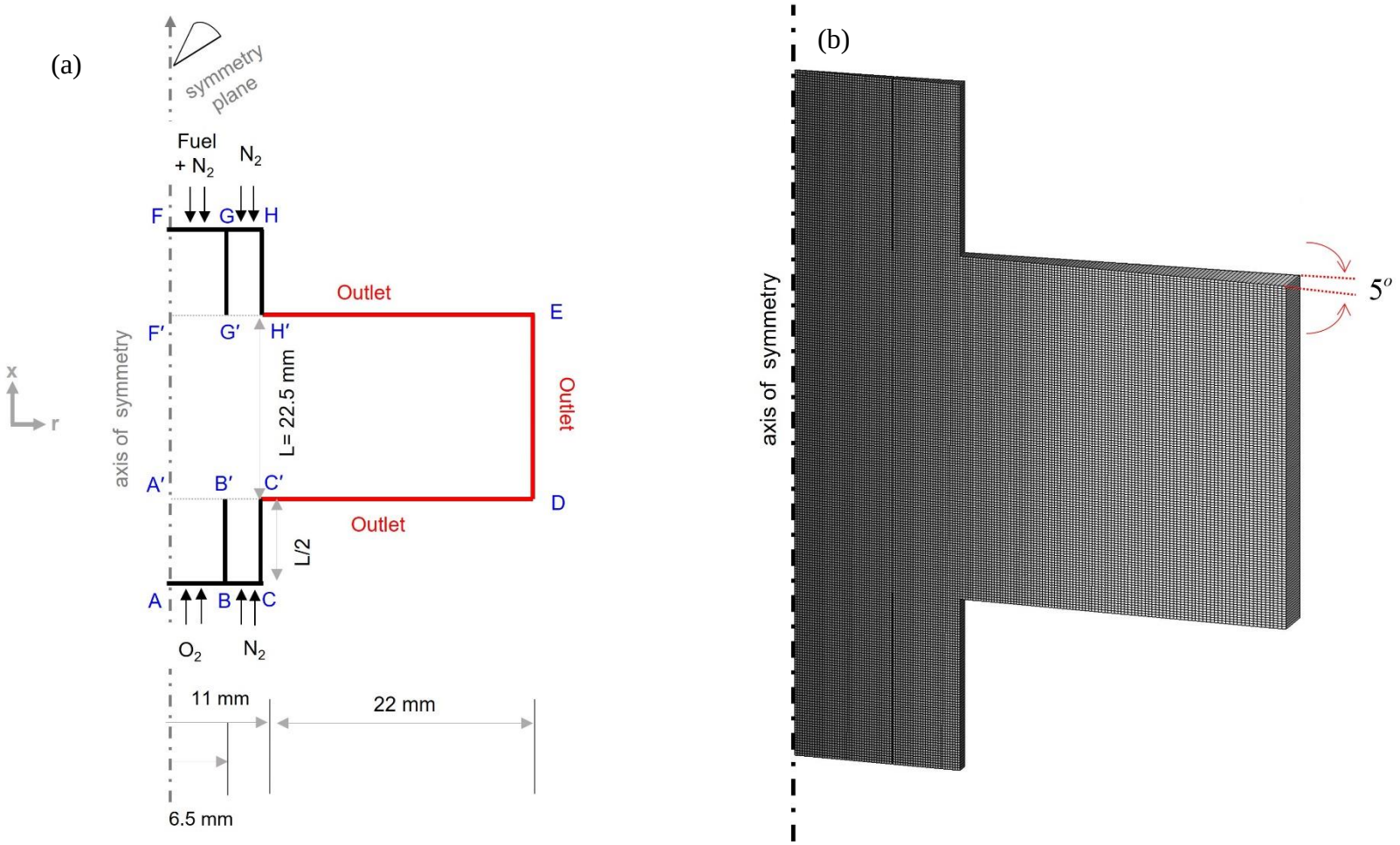

Figure 4.10 (a) Schematic of counterflow burner (dimensions are not in scale), (b) 2D-axisymmetric geometric model for computation

In the experiment, hydrodynamically converged nozzles were introduced to attain a uniform velocity profile at the exits [120]. As discussed previously (see sections 4.1 and 4.3), in the counterflow setup, the velocity at the nozzle exits can be affected by the thermal expansion of the flame, causing deviation from a uniform (top hat) distribution [72, 76, 77]. To account for this in the numerical simulation, entrance lengths with slip boundary conditions were included in the computational geometry near the nozzle exits (Fig. 4.10a: BB', CC,' GG', and HH'). The inlet velocity conditions were set at AB, BC, FG, GH, far from the nozzle exits (i.e., A'B', B'C', F'G', G'H' in Fig. 4.10a). The entrance channels with slip boundary conditions allow the velocity profile at the nozzle exits (Fig. 2.10 (a): A'B', B'C', F'G', G'H'). These entrance channels with slip boundary conditions allow the velocity profile at the nozzle exits to be affected by the flame in a self-consistent manner, allowing for an assessment of deviation from the plug flow condition due to the flame structure. The length of the entrance channels was chosen to ensure that the inlet boundary condition does not have an impact on the velocity profile at the nozzle exits.

A two-dimensional axisymmetric geometry specified by a wedge of a small angle (5 degrees) has been generated and meshed using Gmsh script, an open-source 3D mesh-generating platform [121]. A structured non-uniform mesh having higher spatial resolution near the mixing zones with only one mesh cell in the azimuthal direction has been implemented. The computational domain consists of 31,718 cells and 64,314 nodes with a minimum and maximum grid size of 163 μm and 326 μm, respectively. The cell sizes used for the analyses are chosen as such to ensure mesh-independent solutions.

4.7 BOUNDARY CONDITIONS AND SIMULATION PARAMETERS

A Dirichlet boundary condition is employed on both the inlets for velocity, temperature, and species described as follows. The lower nozzle was set to have a flow of ambient oxygen, while the upper nozzle was set to have a flow of a mixture of dimethyl ether and nitrogen at a temperature of 550K. Additionally, a uniform velocity boundary condition was applied to all the nozzle inlets, including the central and coaxial flows, using the global strain rate as a reference, which is defined as the density-weighted gradient of the axial flow velocity on the oxidizer side [1], i.e. $a = \frac{2U_O}{L}(1 + \frac{U_F\sqrt{\rho_F}}{U_O\sqrt{\rho_O}})$, where U_F and U_O are the velocities at the fuel and oxidizer side nozzle exits, ρ_F and ρ_O are the mixture densities at the respective exits, and L is the separation distance. With ascertaining the constraint that two streams are momentum-balanced, the global strain rate is simply $a = \frac{4U_o}{L}$. The outlet boundary is set in such a way that it can resolve any entrainment from the ambient. When there is no backflow at the outlet boundary, a zero-gradient condition for velocity outlet and a fixed value for pressure. Outlet is prescribed to exist at one-atmosphere pressure. In backflow situations with regions of negative velocity flux in the domain outlet, the normal inflow velocity is evaluated from the flux normal to the cells, and a zero-gradient condition is prescribed for outlet pressure. The temperature at the outlet boundary is switched between zero gradient and a fixed value of 300 K when backflow occurs. The species outlet boundary condition is switched between zero gradient and fixed mole fraction value for air (i.e., 0.23 and 0.77 for oxygen and nitrogen, respectively).

Finally, the three-dimensional case was simplified to a two-dimensional model with an axisymmetric structure by a wedge of 5 degrees along the axis-centerline as shown in

Fig. 4.10b. The details of the geometric entities and corresponding boundary conditions for velocity, species, and temperature are presented in Table 4.1.

Table 4.1: Geometric entities and boundary condition

Boundary	Boundary Condition	Boundary	Boundary Condition
AB (Oxidizer inlet)	$u_{ax} = U_o$ $T = 300K$ $X_{O_2} = 1$	BB′, CC′ (Oxidizer side entrance)	$-\bar{n}.\nabla\bar{u} = 0$ $T = 300K$ $-\bar{n}.\nabla Y_k = 0$
BC (Nitrogen inlet, oxidizer side)	$u_{ax} = U_o$ $T = 300K$ $X_{N_2} = 1$	GG′, HH′ (Fuel side entrance)	$-\bar{n}.\nabla\bar{u} = 0$ $T = 550K$ $-\bar{n}.\nabla Y_k = 0$
FG (Fuel inlet)	$u_{ax} = -U_F$ $T = 550K$ $X_{DME} = 0.1 \sim 0.6,$ $X_{N_2} = 0.9 \sim 0.4$	C′D, DE, EH′ (outlet)	$-\bar{n}.\nabla\bar{u} = 0$ $-\bar{n}.\nabla T = 0$ $-\bar{n}.\nabla Y_k = 0$
GH (Nitrogen inlet, fuel side)	$u_{ax} = -U_F$ $T = 550K$ $X_{N_2} = 1$	AF	Axis of symmetry

Simulations were conducted over a range of physical conditions and parameters to investigate various aspects of counterflow cool flame. Initial simulations were performed with non-reacting cases to understand how Reynolds number affects the entrainment of outer (co-flow) species in the central core. Then, chemically reacting cases were simulated at different fuel loading and global strain rate with and without the effect of gravity to investigate the formation and extinction of counterflow cool flame at atmospheric pressure. Lastly, simulations were conducted at 3 and 5 atmospheres to study flame extinction under those conditions. The different physical conditions and simulation parameters considered in this study are summarized in Table 4.2.

Table 4.2: Physical conditions and simulation parameters

Non-reacting flow (N_2-N_2 flow with different co-flow species)			
Pressure (atm)	Co-flow species		Reynolds number
1	Helium (He) Nitrogen (N_2) Argon (Ar)		8~300
Chemically reacting flow without buoyancy			
Pressure (atm)	Fuel (DME) loading	Reynolds number[1]	Global strain rate (s^{-1})
1	X_F = 0.587 (base case)	270~650	60~140
Chemically reacting flow without buoyancy			
Pressure (atm)	Fuel (DME) loading	Reynolds number[1]	Global strain rate (s^{-1})
1	X_F = 0.4~0.6	135~650	30~140
3	X_F = 0.1~0.4	700~6000[2]	50~350
5	X_F = 0.075~0.175	1375~5700[2]	60~250

4.8 Mathematical and Numerical Modeling

The mathematical model consists of time-dependent equations of compressible mass, momentum, enthalpy, and species conservation described in chapter 2. In the counterflow cool flame study, simulations have been conducted using the direct numerical solutions (DNS) (i.e., no turbulence model has been implemented). For each case, time-dependent computation has been carried out until a steady-state solution is achieved.

The conservation equations have been discretized in the finite volume method (FVM) presented in chapter 3. The sets of discretized equations are solved in the OpenFOAM [122, 123] platform, an open-source C++ framework for conducting

[1] Reynolds number has been calculated using the conditions prescribed at the oxidizer-side nozzle exit.
[2] No turbulence model was implemented in this study. Computations have been conducted using the direct numerical solutions (DNS) described in chapter 3.

multiphysics simulations. This work incorporates a DNS reacting flow solver developed by Zirwes et al [52, 124, 125] that has been constructed upon the OpenFOAM's native reactingFoam solver. Unlike the reactingFOAM which assumes the Lewis number to be unity (i.e, mass diffusivity (D) = thermal diffusivity (α)), this solver computes the transport coefficients by mixture-average diffusion approximation [126]. Along with the diffusion coefficient, the other transport coefficients for each species (i.e., viscosity (μ), thermal conductivity (λ), heat capacity (c_p)) are computed by Cantera toolkit [127] in python language platform [128]. The coupling between OpenFOAM and Cantera is shown in Fig. 4.11. Details can be found here [125].

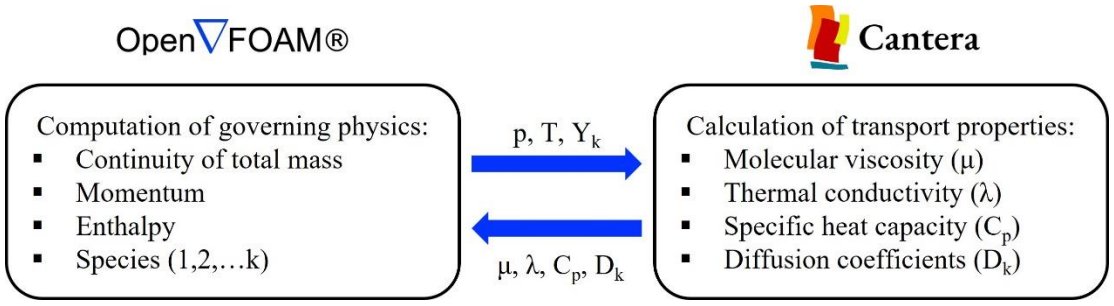

Figure 4.11: Coupling of OpenFOAM and Cantera in DNS reacting flow solver [125]

The discretized equations have been solved in coupled manner with Pressure-Implicit with Splitting Operator (PISO) algorithm. CVODE solver from SUNDIALS package has been embedded in the OpenFOAM solution framework to compute the reaction source term with an operator splitting technique described in chapter 3. The gradient terms have been discretized using a cell-based linear approach. The divergence terms in the momentum, enthalpy, and species equations have been treated with strictly bounded flux-limited schemes. The Laplacian term is treated with a linear interpolation of the surface normal gradient correction scheme. Euler backward implicit scheme is used for

time integration. Simulations have been conducted with variable time stepping. The simulation is launched with a minimum time step value of 10^{-8} s. The time step value is then adjusted according to the CFL number ($Co = u\Delta t/\Delta x$) and Fourier number ($Fo = \alpha\Delta t/\Delta x^2$), where Δt is the simulation time step, and α is the thermal diffusivity. Δx is calculated from the cubic root of the cell volume. The maximum value of Co and Fo used in this study are 0.1 and 0.15, respectively (corresponding to a maximum time step value of $\sim 10^{-5}$ s).

The discretized momentum, enthalpy and species transport equations are solved using Stabilized Preconditioned (bi-)conjugate gradient (PBiCGStab) solver [129] with asymmetric diagonal incomplete-LU (DILU) preconditioner [130] with an absolute tolerance of 10^{-8}. For the pressure correction, Preconditioned (bi-)conjugate gradient (PCG) solver with the symmetric diagonal incomplete-Cholesky (DIC) preconditioner [131] with absolute tolerance of 10^{-9}. For the pressure velocity coupling (PISO), three inner and one outer loop are used for the momentum correction without any relaxation treatment.

The chemical kinetic mechanism of dimethyl ether oxidation has been well examined in the literature. In this study, the HPMech-v3.3 model from Princeton University [25] has been incorporated in the OpenFOAM platform. The kinetic model consists of 130 chemical species and 893 reactions and has been well-tested for low-temperature oxidation in multiple studies conducted recently [132-135]. For the counterflow cool flame simulations at 1, 3 and 5 atm pressure, the kinetic model has been converted to the corresponding pressure condition by generalized polynomial (PLOG) fitting method [136, 137] using a Perl script-based software developed in University of Galway [138].

For one-dimensional simulation, OPPDIF [139] module of CHEMKIN package [56] with a modified arc-length continuation method [140, 141] has been employed. It is important to note that no velocity gradient has been imposed at the nozzle exits in the CHEMKIN simulations.

4.9 Results and Discussions

4.9.1 Non-reacting Counterflow Study

Simulations were conducted to study the effect of various physical conditions and parameters on counterflow cool flame formation. The study started with non-reacting cases in which a simplified geometry was used (Fig. 4.12) to investigate the entrainment of outer species into the central core for different Reynolds number conditions. The opposed flow of nitrogen (N_2) has been simulated with three different co-flow species i.e., helium (He), dummy nitrogen (N_2*) and Argon (Ar). The goal was to understand how the entrainment

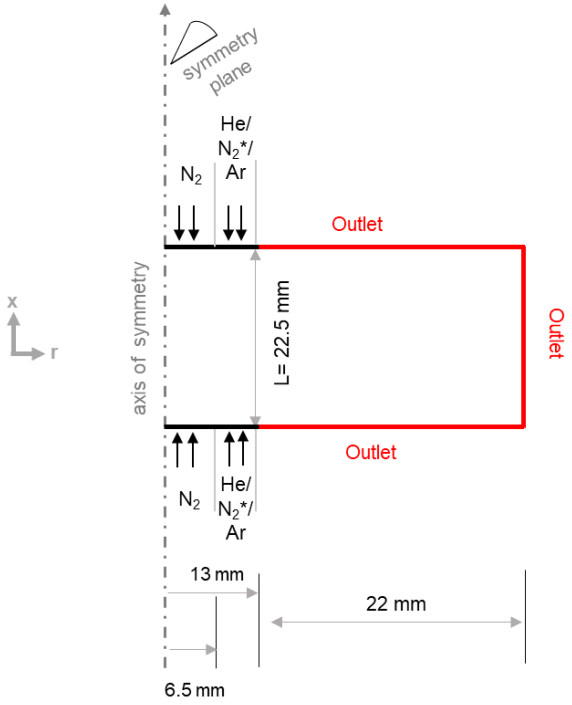

Figure 4.12: Schematic of the simplified geometry for studying coflow infiltration

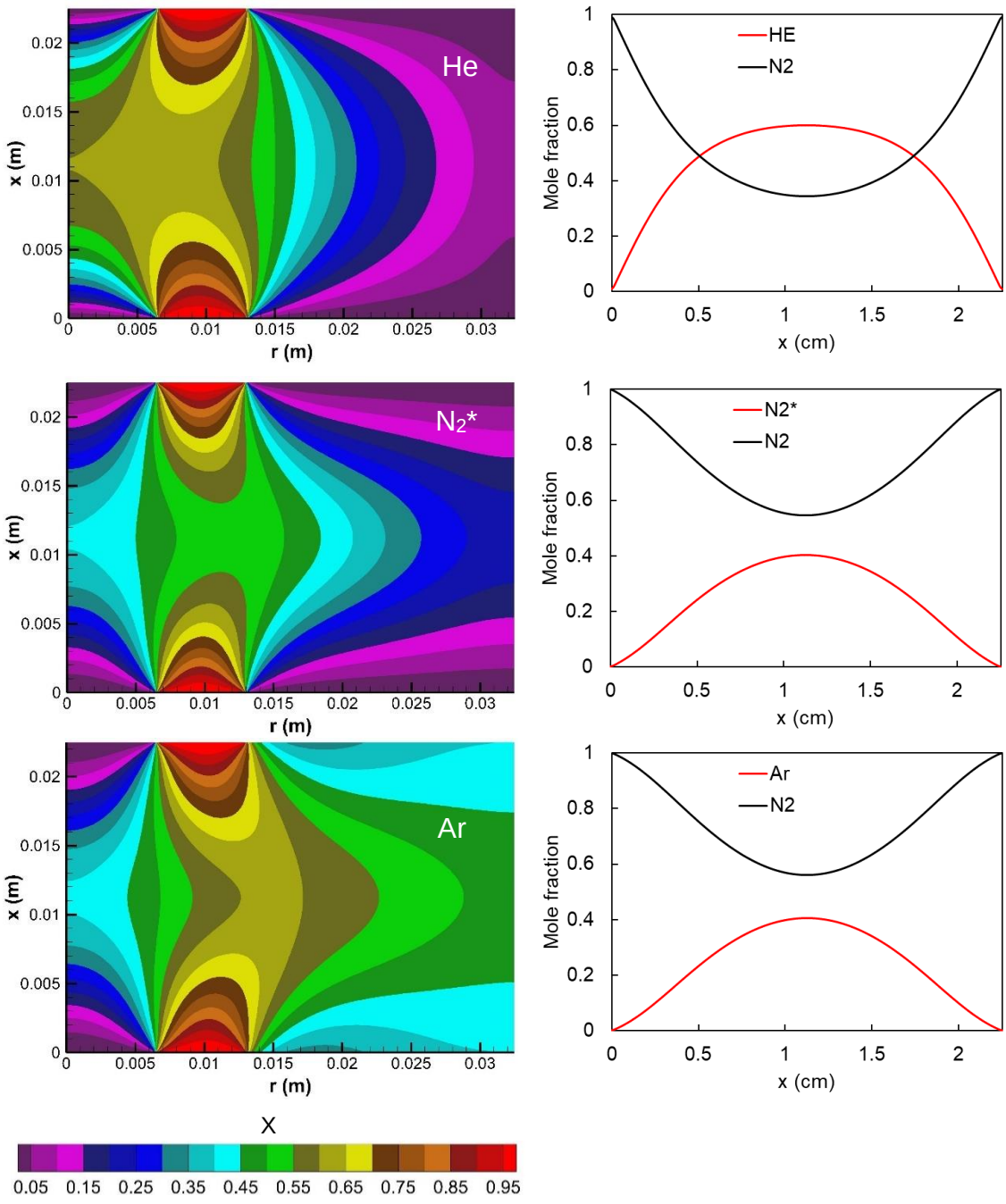

Figure 4.13: Contour co-flow species (left column) and corresponding axial distribution of central (N_2) and co-flow species (He, N_2*, Ar). $U_{upper\ (central)} = U_{upper\ (co\text{-}flow)} = U_{bottom\ (central)} = U_{bottom\ (co\text{-}flow)} = 0.1$ m/s, Re ~ 8 (isothermal case @300K).

of these different species, with varying molecular weights, affect the central flow. This will provide a basic understanding on whether the counterflow flame is affected by the

entrainment of outer species at any given Reynolds number condition. For simplicity, buoyancy effect has been neglected here and temperature isothermal (300K) boundary condition has been prescribed.

Fig. 4.13 shows the contour of co-flow species and axial distribution of co-flow and central flow species for N_2- N_2 counterflow at Re ~8. It is found that when helium is used as the co-flow species in the counterflow of nitrogen, there is the highest level of infiltration with a maximum mole fraction of ~0.6 on the center-axis. On the other hand, the maximum mole fraction for co-flow nitrogen and argon are ~0.403 and 0.407, respectively. This can be explained as follows. The expression of mass diffusivity (D) from the Chapman-Enskog theory is, $D = \frac{AT^{1.5}}{p\sigma^2 \Omega \sqrt{\mathrm{M}}}$, where, A is an empirical coefficient, T is the absolute temperature, M is the molar mass, ρ is the density, σ is the collision diameter, Ω is the temperature dependent collision integral and M is the molecular weight [83, 142]. The ratios of the co-flow to the center species in this study are found to be the followings: i) $D_{He}/D_{N_2} = (M_{N_2}/ M_{He})^{0.5} = (28/4)^{0.5} \sim 2.65$, ii) $D_{N_2}/D_{N_2} = 1$, and iii) $D_{Ar}/D_{N_2} = (M_{N_2}/ M_{Ar})^{0.5} = (28/40)^{0.5} \sim 0.83$. Due to its higher mass diffusivity, helium is able to penetrate and diffuse into the central core, reaching the center-line axis. As the co-flow species become heavier, the amount of entrainment decreases.

Simulations were performed at higher Reynolds numbers to investigate the balance between convective and diffusive transport. The maximum mole fraction of the co-flow species on the center-line axis was plotted as a function of Reynolds number in Fig. 4.14. It is found that once a critical Reynolds number is reached, the diffusive mass transport of the co-flow species dominated by the convective effect of the central flow and the entrainment is diminished. For Argon and nitrogen, the critical Reynolds number is found

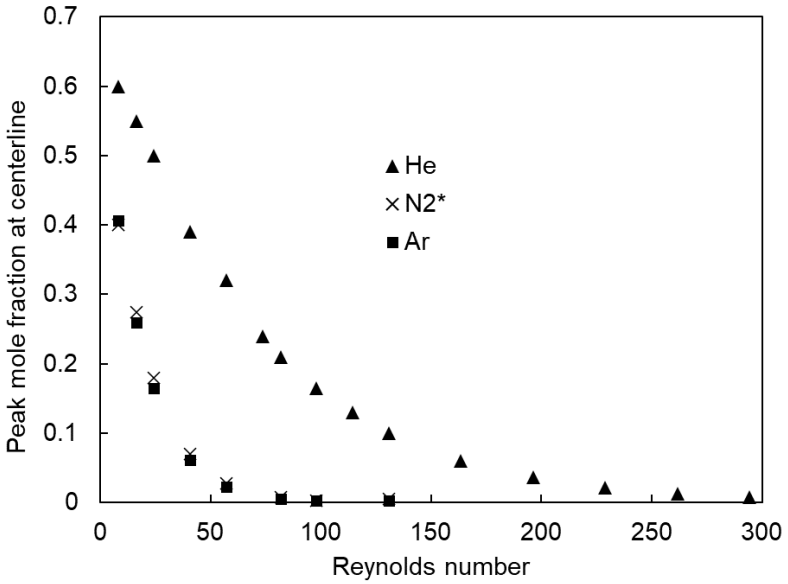

Figure 4.14: Peak mole fraction of the co-flow species on centerline-axis as a function of Reynolds number (N_2-N_2 opposed flow)

to be ~100 and for helium it is ~300. It is important to note that for the DME counterflow studies, the minimum Reynolds number applied is ~270 for a maximum fuel loading of 60% (i.e., X_{DME} = 0.6). For a DME-O_2 opposed flow and N_2 co-flow, the conservative value of the mass diffusivity ratio can be calculated by considering the molecular weight of the heaviest combination of DME- N_2 mixture at the fuel side (60% DME and 40% N_2), i.e., $D_{N_2}/D_{DME-N_2}=[(X_{DME}M_{DME}+X_{N_2}M_{N_2})/M_{N_2}]^{0.5}$ = 0[(0.6×46+0.4×28)/28] $^{0.5}$ ~ 1. 17. It indicates that the co-flow does not significantly affect the flame characteristics at the center-line location in the range of Reynolds number studied. However, in the experiment, co-flow is used to stabilize the flame and prevent its radial propagation. In accordance with the experimental setup, co-flow was incorporated in all the counterflow reacting flow simulations in this study (Fig. 4.10)

4.9.2 COUNTERFLOW COOL FLAME: COMPARISON BETWEEN 1D AND 2D SIMULATION

The 2D-axisymmetric counterflow reacting flow model accounts for two important physical characteristics not considered in the conventional 1D model in CHEMKIN, i.e., radial transport and buoyancy effects. In the following sections, the impact of buoyancy on counterflow flame formation will be discussed. Comparisons will also be made between 2D-axisymmetric OpenFOAM predictions with and without buoyancy, and 1D CHEMKIN calculations to provide a clear understanding of the effects.

Fig.4.15 shows the distribution of temperature, streamline, chemical heat release rate (HRR) and formaldehyde (CH_2O) computed by the 2D-axisymmetric model with (right-hand figures) and without (left-hand figures) the buoyancy effect under identical conditions. It is evident from the streamline distribution (Fig. 4.15a) that the stagnation plane forms at the axis midpoint position for the case without buoyancy due to the constraint of a momentum-balanced boundary condition. The flame is located slightly away from the stagnation plane towards the fuel-side and remains flat along the radial direction. Far downstream, the flame front deviates slightly to the upward direction due to the edge effect. With buoyancy been accounted for, the stagnation plane is further lifted to the upward direction and closer to fuel-side due to the density variation. The stagnation plane is formed at ~ 2.65 mm from the axis midpoint which is a deviation of 23% compared to the case without buoyancy (0% refers the stagnation plane formed at the axis midpoint, i.e., x = 1.125 cm or 11.25 mm). Furthermore, downstream, the flame continues to move upward as it travels radially. The variation of temperature, heat release rate and formaldehyde distribution along the radial direction is evident when buoyancy effect is incorporated (right-hand plots, Fig. 4.15)

(a)

(b)

(c)

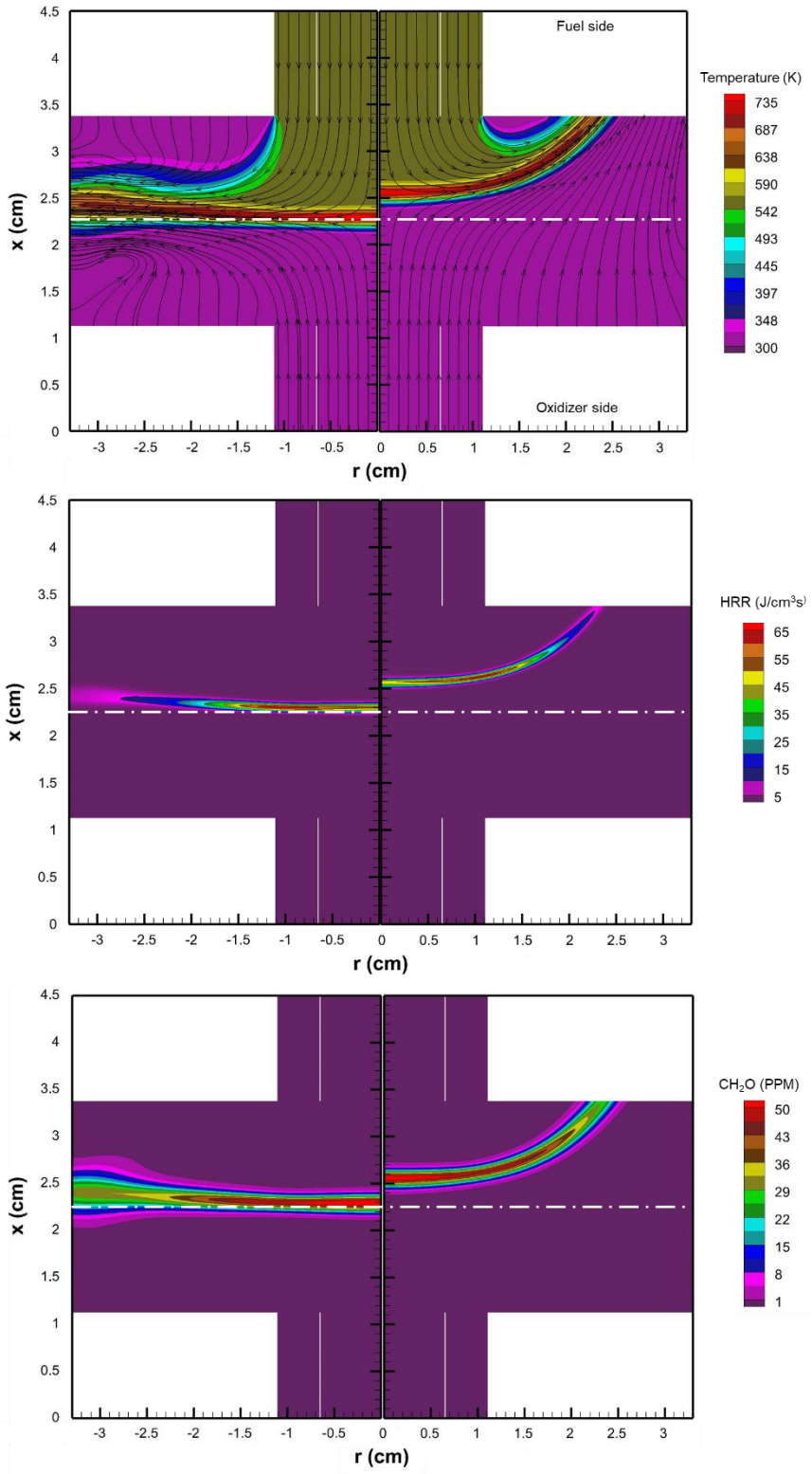

Figure 4.15: DME cool flame without (left halves) and with (right halves) buoyancy under. identical conditions (X_{DME} = 0.587, U_F = 62.3 cm/s, U_O = 50.9 cm/s, a ~ 90 s^{-1}). (a) Temperature distribution and streamlines, (b) Heat release rate (HRR), and (c) formaldehyde (CH_2O) concentration. White dot-dashed line marks the axis midpoint.

(a)

(b)

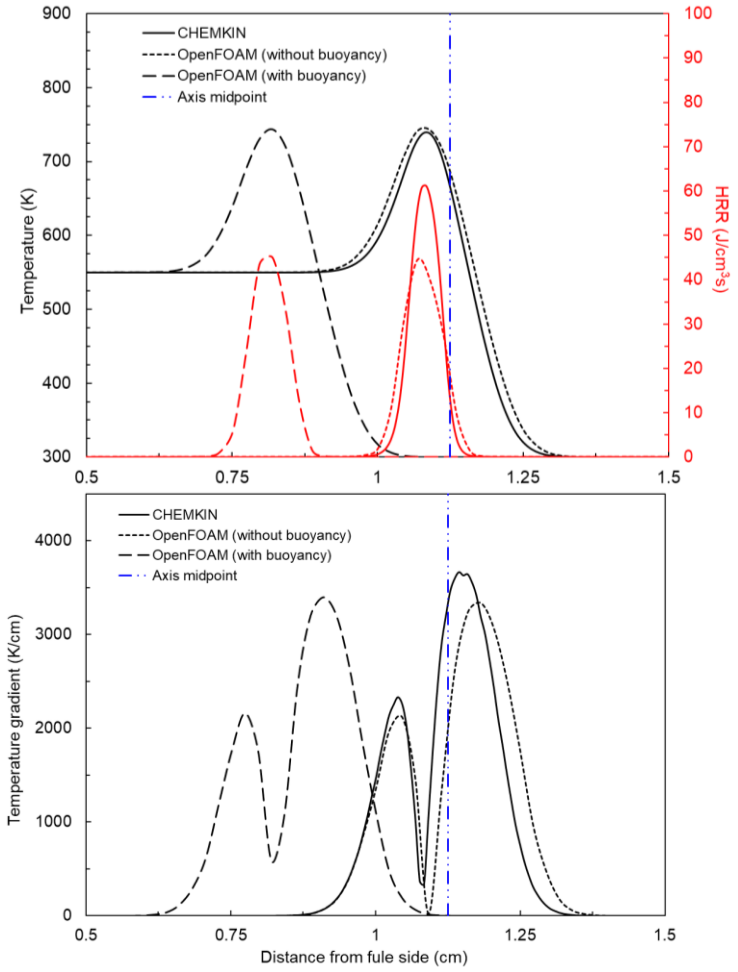

Figure 4.16: Computed axial distribution of (a) temperature and heat release rate (HRR), (b) temperature gradient for 2D (with and without buoyancy) and 1D simulation. DME cool flame (X_{DME} = 0.587, U_F = 62.3 cm/s, U_O = 50.9 cm/s, a ~ 90 s^{-1}).

For further elucidation, centerline distributions of temperature, heat release rate, velocity and velocity gradient have been plotted both for the with and without gravity and compared against the CHEMKIN prediction (Fig. 4.16-4.17). The peak temperature for 1D and 2D without and with buoyancy are found to be withing ~4K difference (737K, 741.75 and 743.5 K, respectively. However, flame structure appears to be thinner in 1D prediction compared to the 2D simulations. The peak temperature location is almost the same for the 1D and 2D without buoyancy cases, i.e., ~0.4 mm from the axis midpoint. When buoyancy

is incorporated, the peak temperature is location at x = 0.82 cm which is 3.05 mm from the axis midpoint. Therefore, the buoyancy appears to be the dominating factor that dictates the location of the flame on the centerline and its structure along the radial direction. The peak chemical heat release rate for 2D without and with buoyancy is found to be similar, i.e., ~45 J/cm^{3}s. The peak HRR is ~75 J/cm^{3}s for the 1D calculation although the peak temperature appears almost identical. The axial temperature gradient (|dT/dx|) has been examined to explain this (Fig. 4.16b). The flame temperature of the flame is determined by the balance between the chemical heat release and the diffusive heat loss on the either side of the flame. In 1D simulation, the flame is thinner than the 2D simulation flame. Therefore, temperature gradient across the flame is higher and diffusive loss is greater ($Q_{diffusion}$ ~ dT/dx) which reduces the overall flame temperature. The computed peak temperature gradients are found to be ~3800 K/cm and 2300 K/cm, respectively, for 1D and 2D calculation.

The position of the stagnation plane depends on the momentum balance between the opposing streams, velocity conditions at the nozzle exits and their deviation from ideal plug flow conditions. In 1D analyses, the deviation from ideal plug flow condition is typically incorporated by imposing a finite velocity gradient that can match the measured flame temperature profile over a range of strain rates [25]. On the contrary, the 2D axisymmetric model in this study allows the perturbation to be resolved without any imposition of any additional boundary conditions. To realize this, the axial velocity and its gradient has been plotted for CHEMKIN and OpenFOAM calculations in Fig. 4.17. In the CHEMKIN model, since buoyancy is not accounted for, the stagnation plane is formed near the axis midpoint location (x = L/2 = 1.125 cm)) due to the constraint of the

(a)

(b)

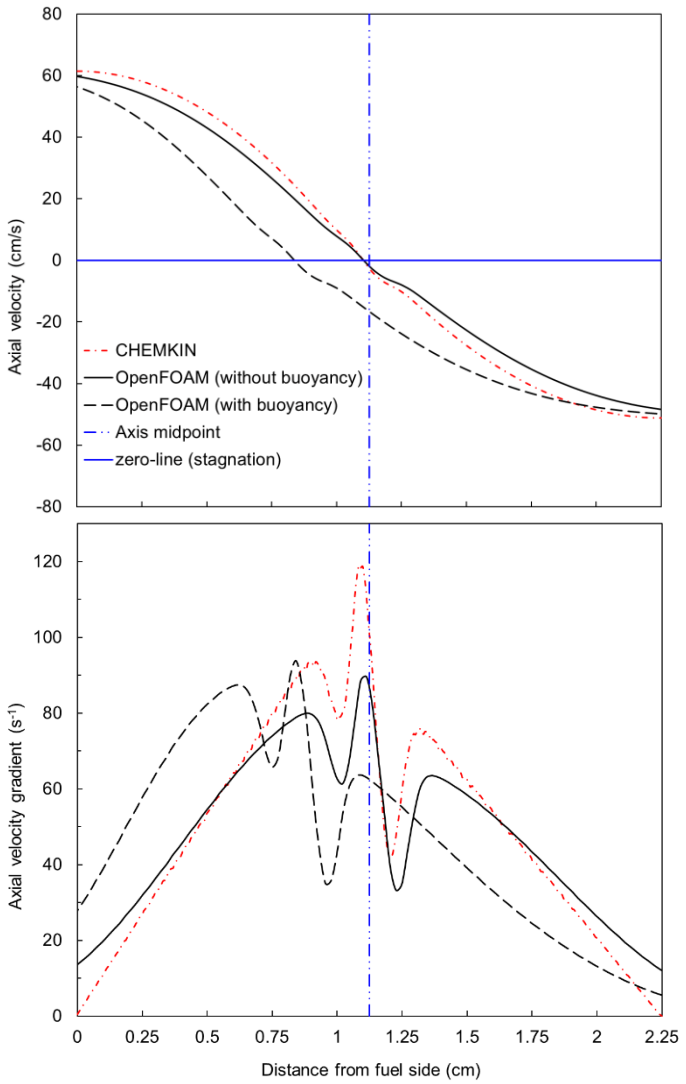

Figure 4.17: Computed axial distribution of (a) axial velocity and (b) axial velocity gradient for 2D (with and without buoyancy) and 1D simulation. DME cool flame (X_{DME} = 0.587, U_F = 62.3 cm/s, U_O = 50.9 cm/s, a ~ 90 s^{-1}).

momentum-balanced boundary conditions. The velocity gradient at the nozzle exits is zero (Fig. 4.17b) since no finite value was imposed. The 2D simulation also results in the stagnation plane formed at the axis midpoint location when gravity was not accounted for (Fig. 4.17a). However, a closer look at Fig. 4.17b reveals that the solution retains a non-zero velocity gradient value of ~16 s^{-1} at both the nozzle exits. In OpenFOAM simulation, the extended entrance channels allow the velocity at the nozzle exits to be perturbed by the

flame. Since the perturbation is identical on both sides, 2D model without buoyancy retains the momentum-balanced condition and forms the stagnation plane at the axis midpoint. On the other hand, when buoyancy effect is incorporated, the stagnation plane is formed above the axis mid-position (at x ~0.86 cm, Fig. 4.17a). The flame, heated fuel and nitrogen are lighter than the ambient oxidizer coming from the bottom burner. So, due to the buoyancy, the stagnation plane is shifted upward, and the flame resides on the fuel-side of the chamber. This results in the velocity at the fuel-side nozzle exit being affected by the flame more than that of the oxidizer-side nozzle exit, resulting in different velocity gradients at the two nozzle exits. The velocity gradients at the nozzle exits at the fuel-side and oxidizer-side are found to be ~28 s^{-1} and ~7 s^{-1}, respectively. The velocity perturbation at the nozzle exits can be further demonstrated by plotting the computed axial and radial component of the velocity as a function radial distance at the fuel-side nozzle exits for the 2D simulations along with the plug flow boundary conditions for the 1D simulations (Fig. 4.18). 2D simulations predict the existence of an axisymmetric dip in the axial velocity profile manifesting the velocity gradient at the nozzle exits. The amount of the dip is found to be ~4.5% and ~11% for the case without and with gravity, respectively. Furthermore, both the axial and radial velocity exhibit non-uniform distribution along the radial distance signifying the two-dimensional characteristics of the system (Fig. 4.18b). The radial component of the velocity increases linearly up to a certain distance in radial direction to compensate the dip of the axial velocity. It then shows a decreasing trend following the increase of the axial component of the velocity to conserve the continuity. It should be noted that, in both cases at $r \approx 6$ mm, a sudden decrease in the axial velocity (and increase of the radial velocity) is observed. This is due to the momentum mismatch between the

main/central flow and the co-flow. Co-flow N_2 has the same velocity as the corresponding main nozzle, but their density is different which causes a momentum mismatch at the outer edge of the main nozzle. In conclusion, it can be stated that the 2D axisymmetric model is able to capture deviation of the plug flow condition at the nozzle exit exhibit a non-uniformity in the radial direction.

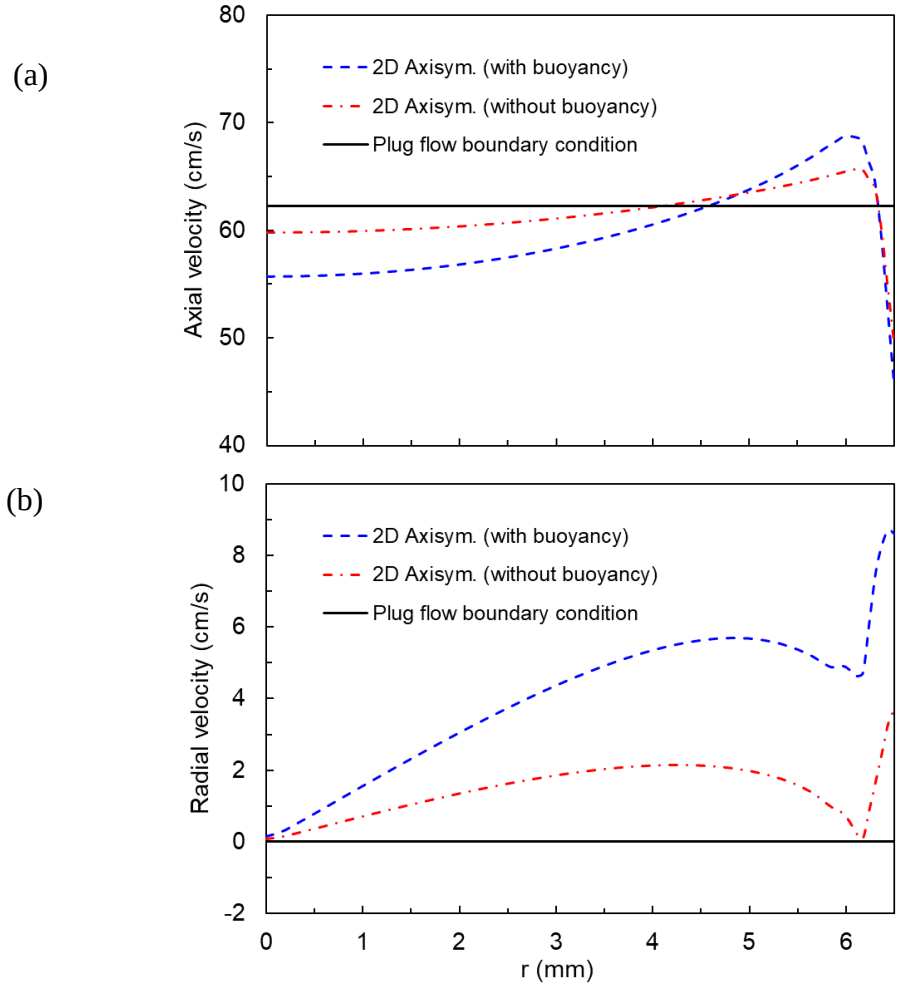

Figure 4.18: Computed radial distribution of (a) axial and (b) radial velocity for 2D (with and without buoyancy) and plug flow velocity boundary condition at the fuel-side nozzle exit. DME cool flame (X_{DME} = 0.587, U_F = 62.3 cm/s, U_O = 50.9 cm/s, a ~ 90 s^{-1}).

The amount of reactant leakage is significant for cool flame. The reactants diffuse across the stagnation plane to form a sustainable reacting zone that dictates the flame

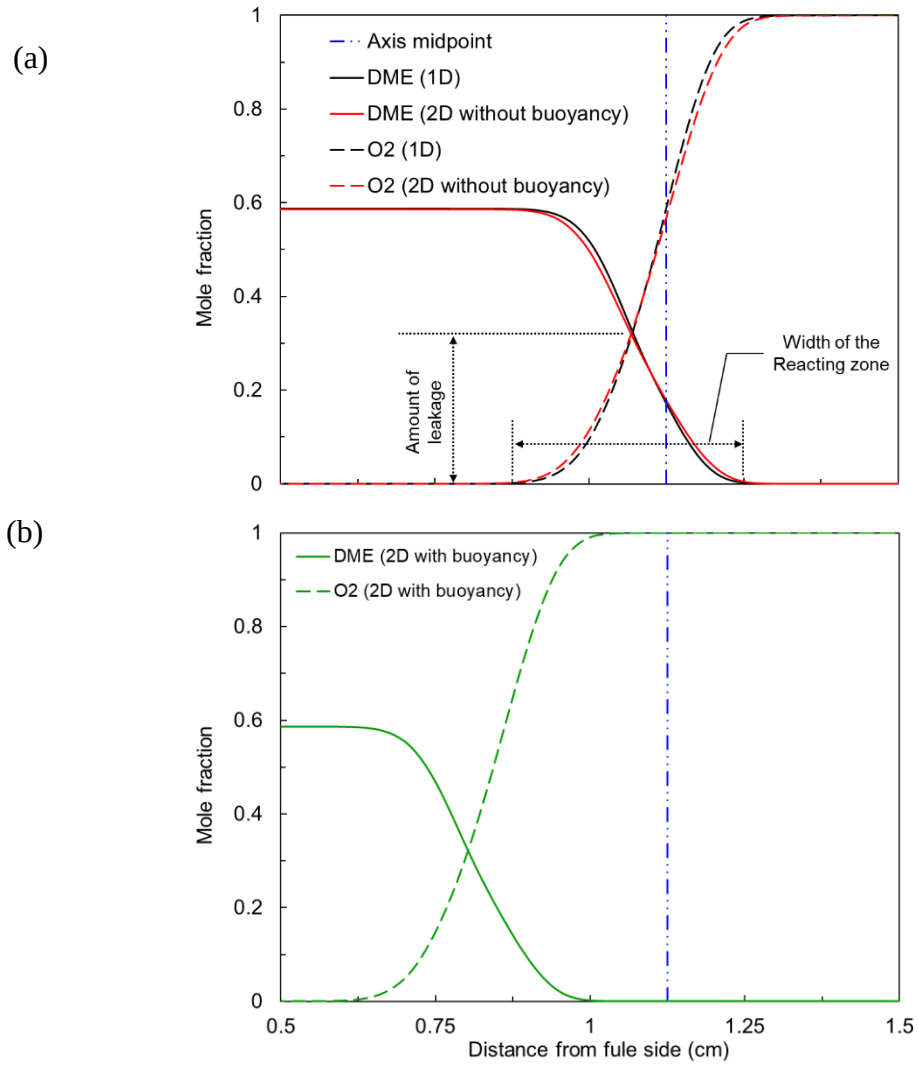

Figure 4.19: Reactant leakage comparison among (a)1D and 2D without buoyancy, (b) 2D with buoyancy for DME cool flame (X_{DME} = 0.587, U_F = 62.3 cm/s, U_O = 50.9 cm/s, a ~ 90 s^{-1}). The methods of determining the amount of leakage and width of the reacting zone are annotated in (a).

structure. Fig. 4.19 shows the comparison of reactant leakage between 1D and 2D model prediction. The amount of fuel leakage and the width of the reacting zone have been analyzed. In this study, the DME mole fraction at the intersection of the DME and O_2 axial distribution is defined as the amount of the fuel leakage, whereas the distance between the locations within where the DME and O_2 are fully consumed is defined as the width of the

reacting zone (see Fig. 4.19a for the visualization of the methods). It is observed that in all these three scenarios, mole fraction of DME at the intersection of DME and O_2 is ~0.32. Thus, the percentage of fuel leakage is found to be $X_{DME\ (intersection)}/\ X_{DME\ (maximum)}$ or 0.32/0.587, i.e., 54.%. However, the width of the reacting zone shows variation between 1D and 2D computation. For 1D simulation it is found to be ~4.8 mm, whereas for both with and without buoyancy effect, the 2D simulation shows a reacting zone of ~5.2 mm which is ~8% thicker. It can be attributed to the associated boundary condition perturbations. The 2D model allows the velocity to be perturbed by the flame resulting in a wider mixing zone. So, the diffusion across the mixing zone is better presented by the 2D model. Fig. 4.19a shows that the 2D model captures a lower gradient of the species mole fraction exhibiting in a much for diffusion dominant transport compared to the 1D model.

4.9.3 CHEMICAL CHARACTER OF DME COOL FLAMES

To gain a thorough understanding of the multidimensional, transport-coupled DME cool flame chemistry in counterflow geometry, the following case has been chosen as the base case for analysis: $X_{DME} = 0.587$, $U_F = 62.3$ cm/s, $U_O = 50.9$ cm/s, a ~ 90 s^{-1}. To identify the important species that govern the DME low temperature oxidation in counterflow configuration, first the major reactions that contribute the most to the overall heat release rates are sorted from CHEMKIN simulations. Fig. 4.20 shows the normalized heat production of the top ten reactions that contribute to the majority (~86%) of the peak chemical heat release integrated over the centerline axis. Oxidation of methoxy methyl, CH_3OCH_2 (rxn# 812 and rxn#883), contributes to ~37% of the total heat release rate

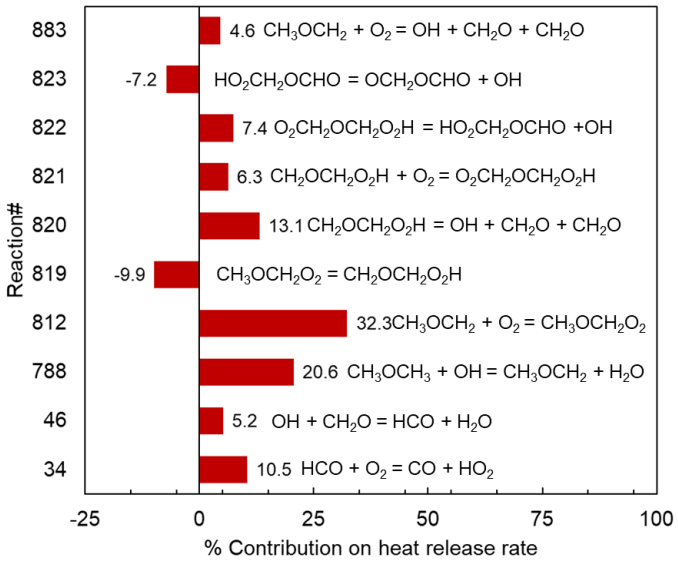

Figure 4.20: Major reactions and their contributions to the peak heat release rate in DME cool flame in CHEMKIN simulation (X_{DME} = 0.587, U_F = 62.3 cm/s, U_O = 50.9 cm/s, a ~ 90 s^{-1})

(HRR). The reaction between DME and OH is the second-largest contributor to the heat release rate in the cool flame that produces the methoxy methyl radical (rxn# 788: CH_3OCH_3 + OH = CH_3OCH_2 + H_2O). The oxidation of methoxy methyl produces methoxymethyl-peroxy radical (rxn# 812: CH_3OCH_2 + O_2 = $CH_3OCH_2O_2$), which forms the hydroperoxyl methoxymethyl radical ($CH_2OCH_2O_2H$ or QOOH) via internal isomerization (rxn# 819). The QOOH is an important low-temperature species that decomposes to two formaldehyde (CH_2O) and one hydroxyl (OH) radical (rxn# 820). The decomposition (β-scission) of QOOH is an exothermic reaction and contributes to ~13% of the total chemical heat release rate. QOOH can also be oxidized (rxn# 821) to form a peroxy methoxymethyl hydroperoxide ($O_2CH_2OCH_2O_2H$ or O_2QOOH) radical. This radical decomposes to one hydroxyl (OH) radical and one carbonyl-hydroperoxide (HO_2CH_2OCHO) molecule (rxn# 822). The carbonyl compound then decomposes and gives out one more hydroxyl (OH) radical (rxn#823: HO_2CH_2OCHO = OCH_2OCHO +

OH). The β-scission reaction that decomposes the QOOH radical is dominant at temperatures greater than 600K and responsible for the NTC behavior. It produces only one OH radical as opposed to two OH radicals produced in rxn# 821 through 823 [116, 118].

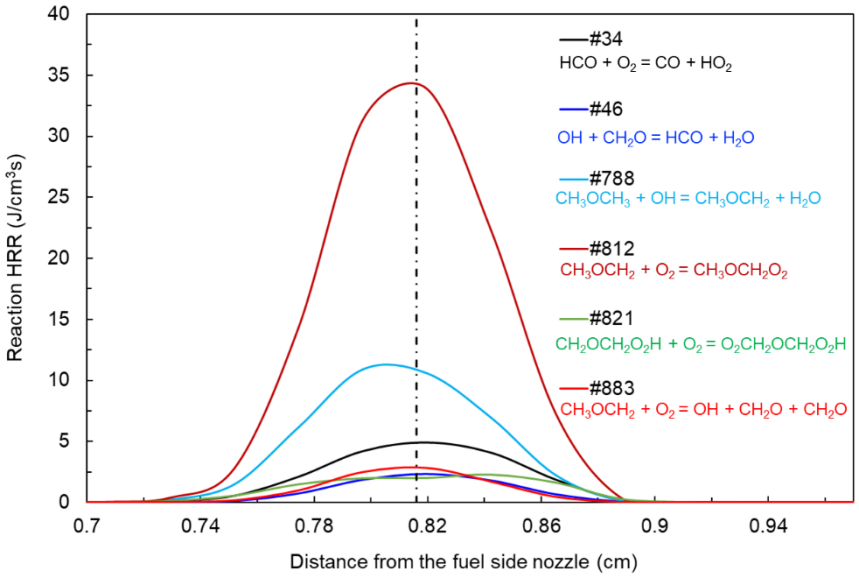

Figure 4. 21: Centerline distribution of the HRR from the major heat releasing reactions of DME cool flame (2D simulation with buoyancy, X_{DME} = 0.587, U_F = 62.3 cm/s, U_O = 50.9 cm/s, a ~ 90 s^{-1}). The dotted-black line marks the location of the peak temperature.

For further elucidation, the centerline distribution of heat productions from the major reactions has been calculated from 2D axisymmetric simulations (with buoyancy) of the base case (i.e., X_{DME} = 0.587, U_F = 62.3 cm/s, U_O = 50.9 cm/s, a ~ 90 s^{-1}), and have been presented in Fig. 4.21. The heat release by the reaction between DME and OH that forms of methoxy methyl radical (rxn# 788: $CH_3OCH_3 + OH = CH_3OCH_2 + H_2O$) is spatially skewed towards the fuel side of the reacting zone. The peak heat release by the is reaction is also located on the fuel-side (~0.2 cm from the peak temperature location) due to the availability of the DME. The heat release distribution by the formation of methoxymethyl-peroxy radical (rxn# 812: $CH_3OCH_2 + O_2 = CH_3OCH_2O_2$), which is the largest contributor

to the chemical heat release rate, is slightly skewed towards the fuel side of the flame. However, the location of the peak heat release by this reaction almost coincides with that of the peak temperature. Methoxymethyl-peroxy is the main source of the QOOH (via internal isomerization) that gives out two formaldehyde and one hydroxyl radical and governs the NTC behavior of DME oxidation. The heat release by the reaction $HCO + O_2 = CO + HO_2$ (rxn#34) exhibits a flatter distribution throughout the reacting zone, with a slight skewness along the oxidizer side preliminary due to the abondance of the oxygen. Similar flatter distribution is observed for the reaction $CH_3OCH_2 + O_2 = OH + CH_2O + CH_2O$ (rxn#883) but skewed slightly towards the fuel-side. This is because the CH_3OCH_2 comes from the decomposition of the primary fuel (i.e., DME) which has lower mass diffusivity lower than oxygen, thereby, shows less tendency to transport across the reacting zone. As described above, instead of breaking down to OH and CH_2O, QOOH can also be further oxidized to form O_2QOOH (rxn# 821). The heat release distribution of this reaction is lower and flatter with a dip at the peak temperature location. It is because this path is dominated by the decomposition of the QOOH via β-scission process in the NTC zone.

The major intermediates that contribute to the formation of DME cool flame and chemical heat release are examined in this section. The axial distribution of these species is presented in Fig. 4.22, for the base-case with buoyancy ($X_F = 0.587$, a = 90.5, p = 1 atm). It is observed that the CO, CO_2, CH_2O and H_2O form throughout the reacting zone with the peak axial location aligned with that of the temperature (Fig. 4.22a). The peak CH_2O mole fraction for the base case has been found to be ~60000 ppm (X ~0.06) whereas the peak OH was found to be below 1 ppm which is a manifestation of oxidation at low-

temperature regime. At low temperature, only a small amount of CO is converted to CO_2 since there is not enough OH to support CO + OH = CO_2 + H reaction. Therefore, a

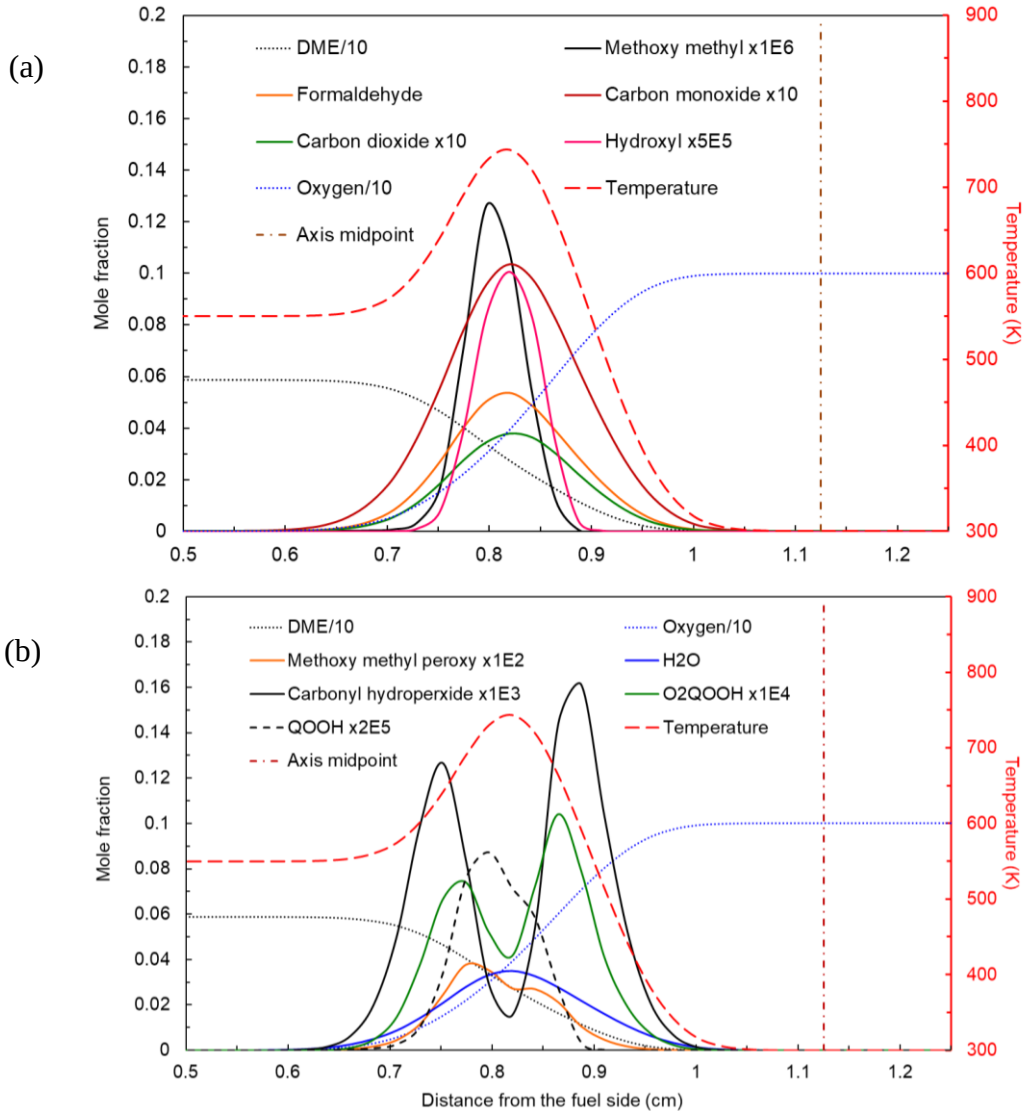

Figure 4.22: Centerline distribution of major species of DME cool flame with buoyancy (X_{DME} = 0.587, U_F = 62.3 cm/s, U_O = 50.9 cm/s, a ~ 90 s^{-1})

significant amount of CO is observed compared to CO_2 in the DME cool flame with a peak concentration of ~11000 and ~400 PPM, respectively. The hydroperoxyl methoxymethyl (QOOH) is formed offset towards the fuel side of the peak temperature location with a value of ~0.45 ppm (Fig. 4.22b). This is due to the abondance of DME which first gives

out the methoxy methyl (CH_3OCH_2) radical. Oxygen diffuses onto the fuel side of the reacting zone (due to having a higher mass diffusivity than DME) and forms methoxymethyl-peroxy radical ($CH_3OCH_2O_2$) reacting with the methoxymethyl radical. The internal isomerization of the methoxymethyl-peroxy eventually produces the hydroperoxyl methoxymethyl radical ($CH_2OCH_2O_2H$ or QOOH). It converts into the peroxy methoxymethyl hydroperoxide (O_2QOOH) by reacting with the oxygen. O_2QOOH exhibits double spike-like structures with the peaks located on the either side of the peak temperature location (Fig. 4.22b) and a dip in the center (aligned with the peak temperature location). Furthermore, due to the abondance of oxygen, the peak value at the oxidizer side is ~25% higher than the peak value on fuel side. The peak values on the oxidizer and fuel-side are found to be ~ 11and ~7.5 ppm, respectively, the minimum value of O_2QOOH is found at the center of the flame (~0.81 cm from the fuel side nozzle exit) since both DME and O_2 are gradually decomposed to sustain the flame.

The contour plots in Fig. 4.23 show that, except for CO and CH_2O, the peak values of all peroxy and hydroperoxyl intermediates are displaced from the centerline (i.e., downstream in the radial direction). To further clarify this observation, the distribution of major species at the centerline (r = 0 cm) has been compared with their distribution at an offset location (r = 1.1 cm) in Fig. 4.24. From Fig. 4.24a it can be observed that at r = 1.1 cm, there are still unreacted O_2 and DME. Moreover, in both location, mole fraction of DME at the intersection of DME and O_2 is ~0.32. The peak value of O_2QOOH at r = 1.1 cm (~14 PPM) is ~40% higher than that at the centerline (~10 ppm). Similarly, a ~35% increase in the peak value of QOOH is observed at r = 1.1 cm (Fig. 4.24b). Furthermore, it is observed from Fig. 4.24c that the methoxy methyl peak remains almost the same both at

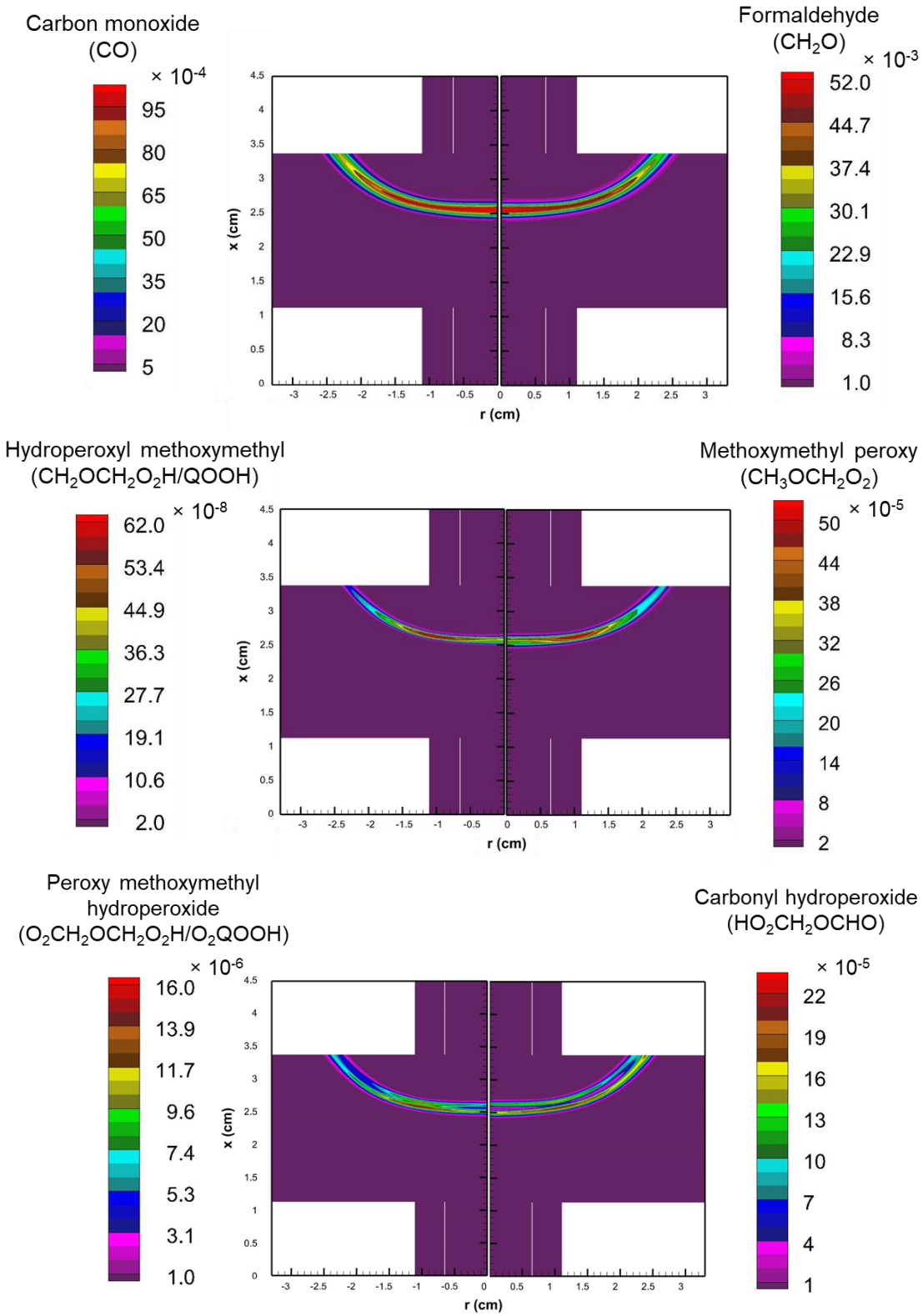

Figure 4.23: Contours of major intermediates of DME cool flame with buoyancy (X_{DME} = 0.587, U_F = 62.3 cm/s, U_O = 50.9 cm/s, a ~ 90 s^{-1})

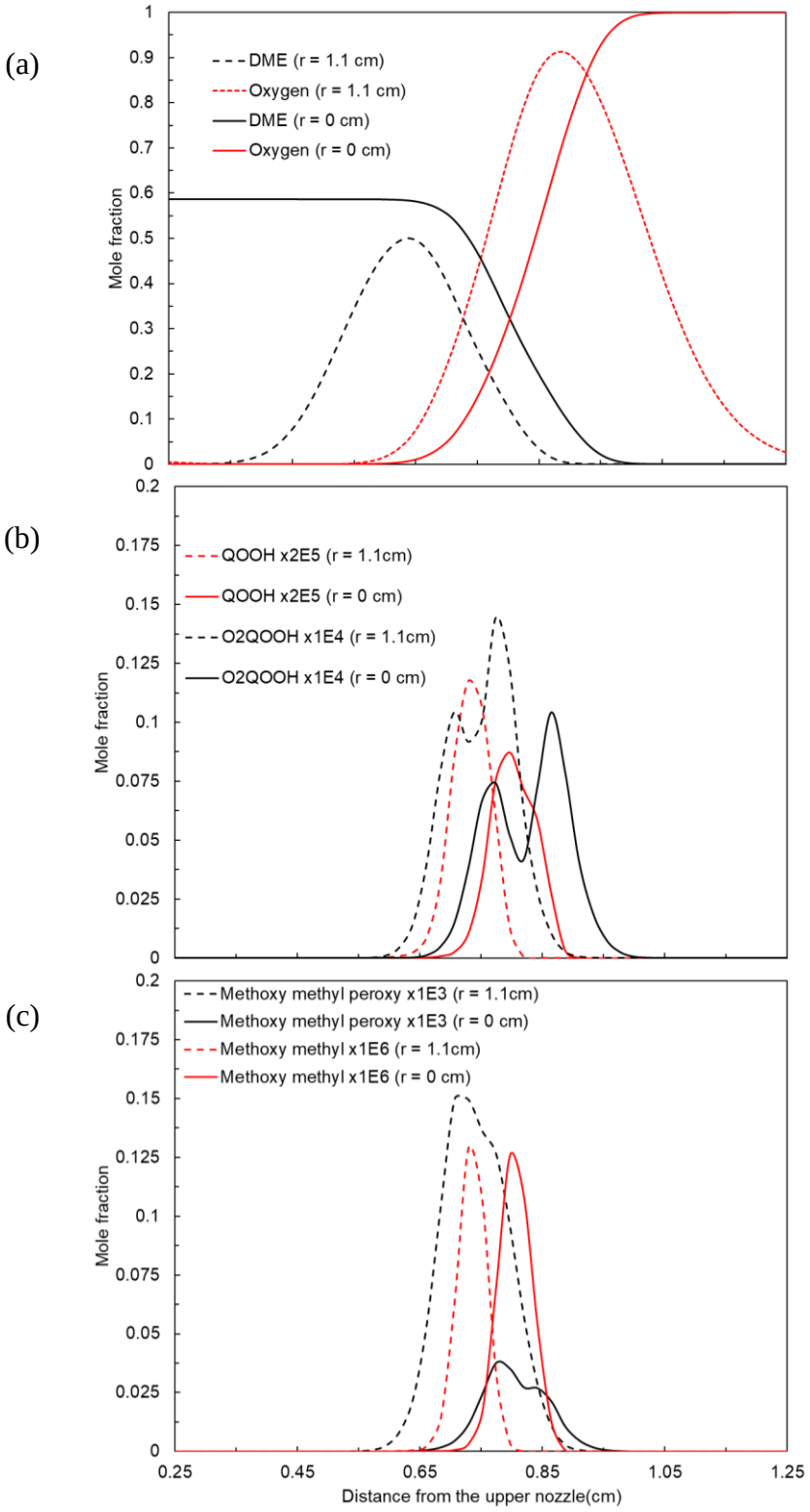

Figure 4.24: Distribution of major species at the centerline (r = 0 cm) and at an offset location (r = 1.1 cm). (2D simulation with buoyancy, X_{DME} = 0.587, U_F = 62.3 cm/s, U_O = 50.9 cm/s, a ~ 90 s^{-1})

the centerline and the offset position, whereas the peak value of the methoxy methyl peroxy increases from ~125 PPM to ~150 PPM (~20% increase). To explain this, contours of velocity magnitude, heat release rate (HRR) and rate of production of the key species are analyzed. Fig. 4.25 shows the contours of velocity magnitude, HRR, OH and CO_2. It can be observed that the HRR, CO_2 and OH also exhibit their maximum value at an offset location from the centerline. For further information, their distribution at r = 1.1 cm is plotted in Fig. 4.26. The peak value of HRR and the temperature at the centerline are ~44

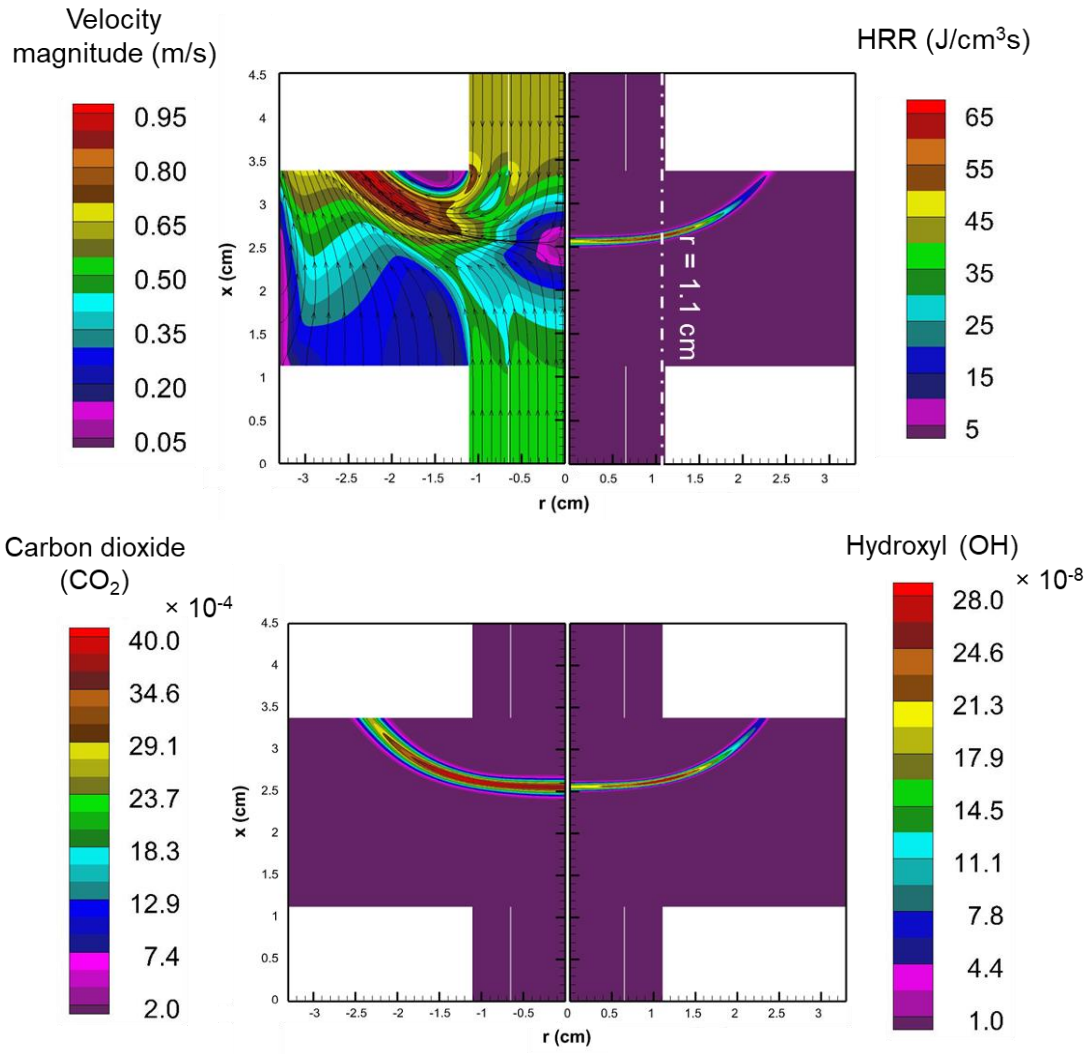

Fig. 4.25: Contours of velocity magnitude, HRR, CO_2 and OH of the DME cool flame with buoyancy (X_{DME} = 0.587, U_F = 62.3 cm/s, U_O = 50.9 cm/s, a ~ 90 s^{-1})

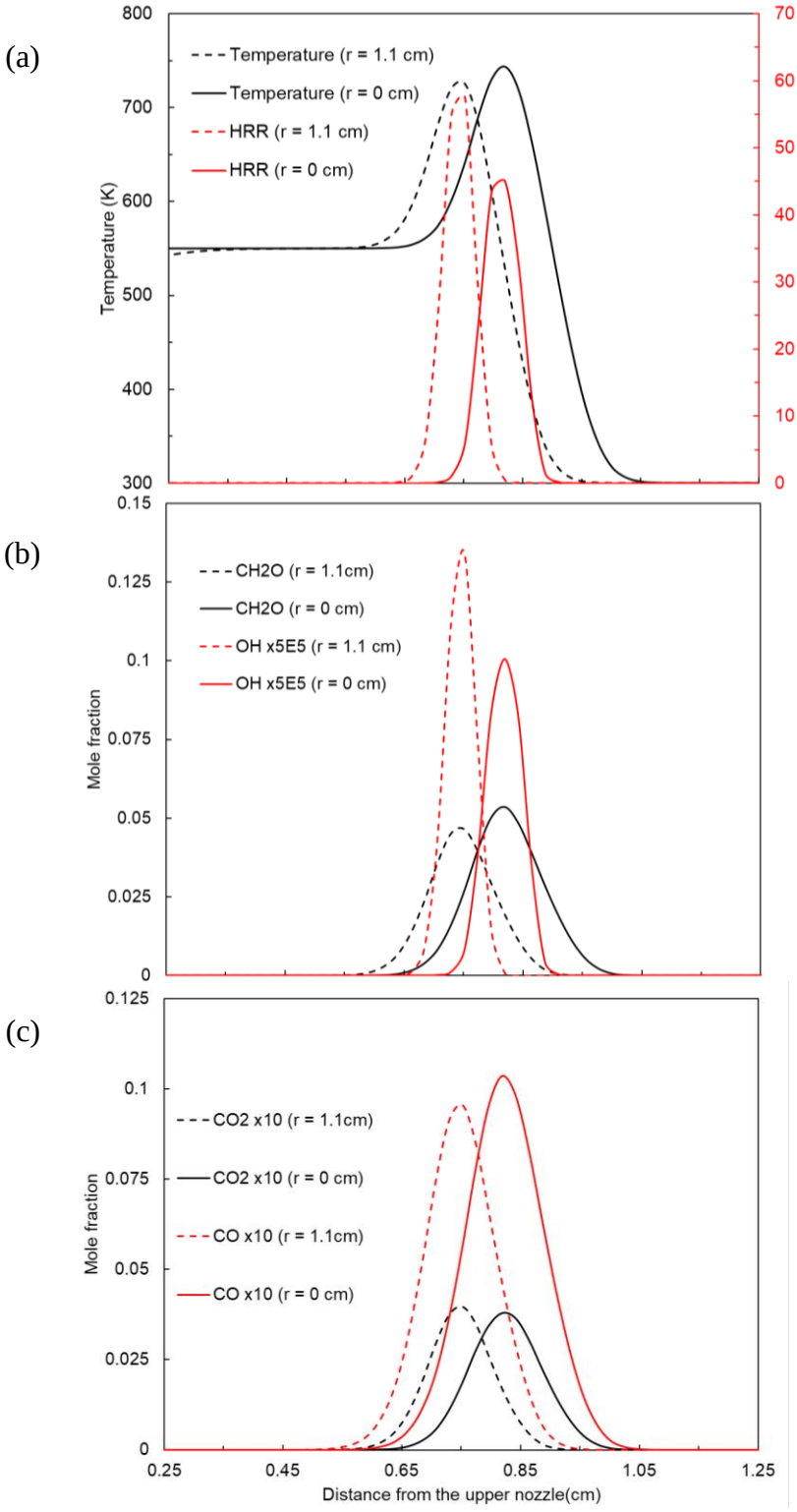

Figure 4.26: Distribution of major species at the centerline (r = 0 cm) and at an offset location (r = 1.1 cm). (2D simulation with buoyancy, X_{DME} = 0.587, U_F = 62.3 cm/s, U_O = 50.9 cm/s, a ~ 90 s^{-1})

J/cm^{3}s and 743K, respectively (Fig. 4.26a). While at r = 1.1 cm, the peak value of HRR is increased to ~58 J/cm^{3}s (~27% increase), the peak flame temperature is decreased to 725K. This can be examined by the contours of velocity magnitude and HRR in Fig. 4.25. The two opposing jets meet and form a stagnation point on the centerline. As a result, a jet is formed in the radial direction to conserve the continuity. The velocity of this jet is at a minimum on the centerline near the flame. As a result, convective effects are minimized on the centerline location. As the jet stream velocity increases downstream, the heat loss due to convection also increases, leading to a decrease in flame temperature despite an increase in the chemical heat release rate.

The peak CH_2O at the centerline and at the offset location is 53600 and 46500 PPM, respectively (~13% decrease) whereas the peak OH increases from ~0.2 to ~0.27 PPM (~35% increase). The increase in the total heat release (representing the overall reactivity) at that location can be attributed to the increase of OH radical pool. In Fig. 4.26C. we also observe a small increase (less than ~5%) of CO_2 production at r = 1.1 cm whereas the CO production is decreased from ~10500 PPM to ~9500PPM (~9.5%). To better understand this phenomenon, rate-of-production (ROP) analysis has been conducted to determine the contribution of the dominant reactions to the net production rates of the key species. first The ROP analyses are presented in Fig. 4.27. On the centerline (r = 0 cm), the hydroxyl production is dominated by the branching of QOOH (rxn# 820: QOOH= OH + 2CH_2O). At r = 1.1 cm, along with the QOOH breakdown, the carbonyl-hydroperoxide decomposition also contributes significantly to the OH radical pool. The reaction rate of the carbonyl-hydroperoxide decomposition (rxn #823: HO_2CH_2OCHO = OCHOCHO + OH) at r = 1.1 cm is ~4.5 times that at the centerline (Fig. 4.27b). The most dominant

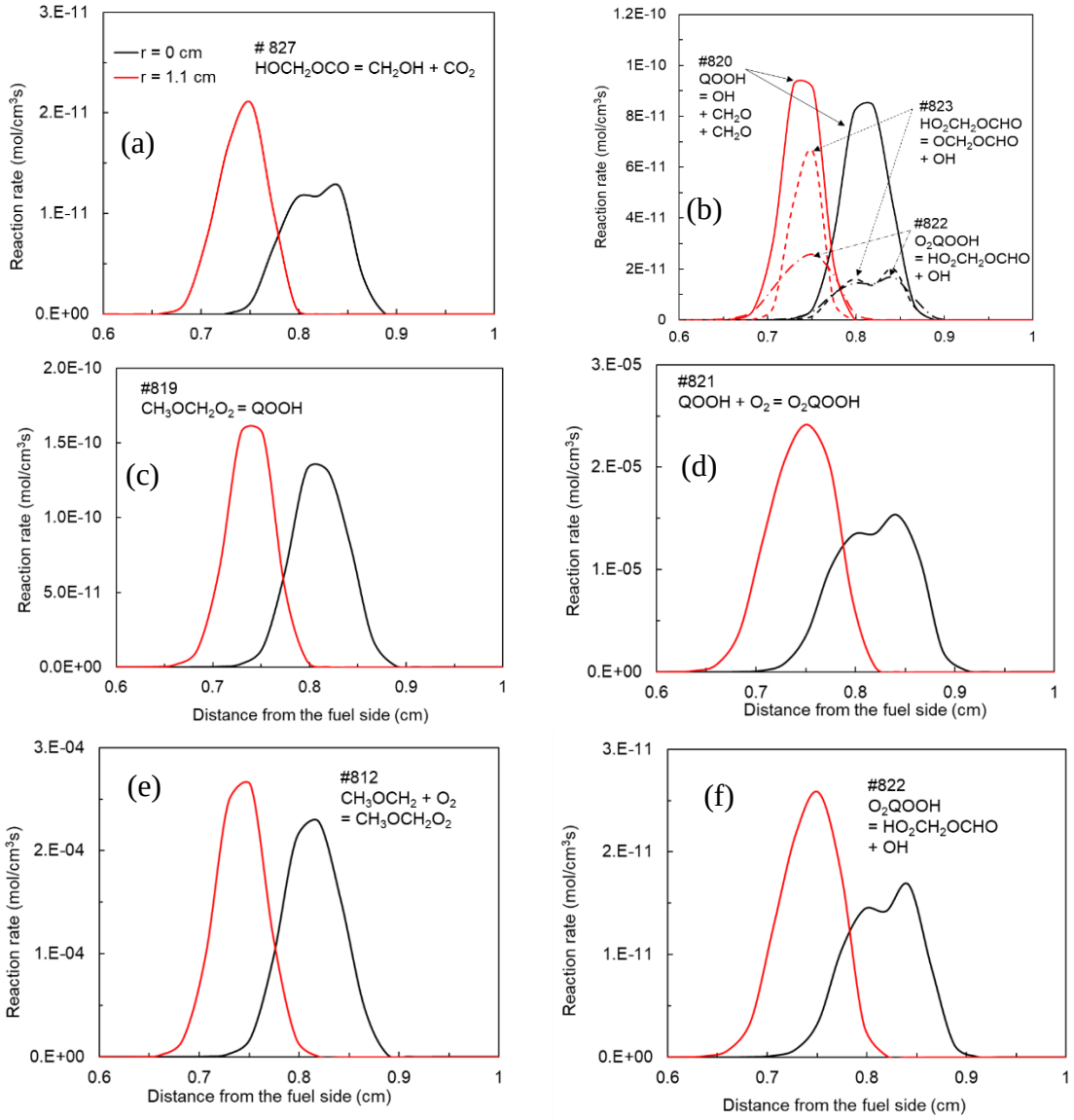

Figure: 4. 27: Rate of production analyses for (a) CO_2, (b) OH, (c) QOOH, (d) O_2QOOH, (e) $CH_3OCH_2O_2$, and (f) HO_2CH_2OCHO at r = 0 cm (black) and r = 1.1 cm (red). The associated major reaction(s) are mentioned appropriately on each graph. (2D simulation with buoyancy, X_{DME} = 0.587, U_F = 62.3 cm/s, U_O = 50.9 cm/s, a ~ 90 s^{-1})

reactions for the production of QOOH, O_2QOOH, methoxymethyl peroxy ($CH_3OCH_2O_2$) and the carbonyl-hydroperoxide (HO_2CH_2OCHO) exhibit enhanced reaction rates at the offset location (i.e., r = 1.1 cm). The peroxy branching routes, i.e., rxn# 821 (QOOH +O_2 = O_2QOOH) and rxn#822: (O_2QOOH = HO_2CH_2OCHO + OH) seem to be boosted by a

factor of ~1.4 and ~1.8, respectively. To summarize, the decomposition of QOOH, which is the dominant pathway for the NTC characteristics in DME oxidation (as discussed in section 4.5), typically produces one OH radical. However, at an offset location from the centerline, the peroxy branching of QOOH (rxn# 821 through #823) becomes significant, producing two OH radicals and leading to an increase in chemical heat release additional release of peroxy and hydroperoxyl intermediates.

4.9.4 Effect of Global Strain Rates

The counterflow flame offers fundamental insights into the detailed structure of diffusion flames with the variation of global strain rate. As described in section 4.7, the global strain rate can be described by, $a = \frac{2U_O}{L}(1 + \frac{U_F\sqrt{\rho_F}}{U_O\sqrt{\rho_O}})$, where U_F and U_O are the velocities at the fuel and oxidizer side nozzle exits, ρ_F and ρ_O are the mixture densities at the respective exits, and L is the separation distance. With ascertaining the constraint that two streams are momentum-balanced, the global strain rate is simply $a = \frac{4U_o}{L}$. In this study, the global strain rate has been varied by changing the value of U_O. Then the U_F is adjusted by applying the momentum-balance condition, i.e., $\rho_O U_O^2 = \rho_F U_F^2$. It is important to note that, in quasi-1D model of CHEMKIN, the stagnation plane location is determined by the momentum-balanced conditions (i.e., at the midpoint of the centerline). In contrast, in the 2D-axisymmetric model, this momentum-balance is accompanied by buoyancy effect, and the location of the stagnation plane is determined by the competition between inertial and buoyancy forces. To understand the combined effect of gravity (i.e., natural convection) and flow inertia in this context, the Richardson number (Ri) has been analyzed.

Richardson number is a dimensionless number that expresses the ratio of the natural and forced convection term [143]:

$$Ri = \frac{g\beta\left(T_{hot} - T_{\infty}\right)D}{V^2} \tag{3.20}$$

where g is the gravitational acceleration, β is the thermal expansion coefficient, T_{hot} is the peak flame temperature, T_{∞} is the ambient temperature, D is the characteristic length (nozzle diameter), and V is the flow velocity (in this case the velocity of the oxidizer side stream). For an ideal gas the thermal expansion coefficient can be determined as follows: $\beta = \frac{1}{\forall}\left(\frac{\partial \forall}{\partial T}\right)_p = \frac{1}{\forall}\frac{\partial}{\partial T}\left(\frac{RT}{p}\right) = \frac{1}{\forall}\frac{R}{p} = \frac{1}{T}$, where $\forall$ is the volume, T is temperature and R is the universal gas constant. Richardson number can also be expressed as the ratio of Grashof number, $Gr = \frac{g\beta\left(T_{hot} - T_{\infty}\right)D^3}{V^2}$ and Reynolds number, $Re = \frac{VD}{\nu}$ as:

$$Ri = \frac{Gr}{Re^2} \tag{3.21}$$

The characterization of a fluid flow system based on the Richardson number is presented in Table 4.3 [144]:

Table 4.3: Physical regime based on Richardson number

Ri < 0.1	Natural convection is negligible
0.1< Ri <10	Both natural and forced convection are important
Ri > 10	Forced convection is negligible

Fig. 4.28 illustrates the evolution of flame structure with the variation of the global strain rate for a fixed fuel loading (X_F = 0.587). At the lowest global strain rate studied (a~60 s^{-1}), the Richardson number is approximately 1.8, indicating that natural convection

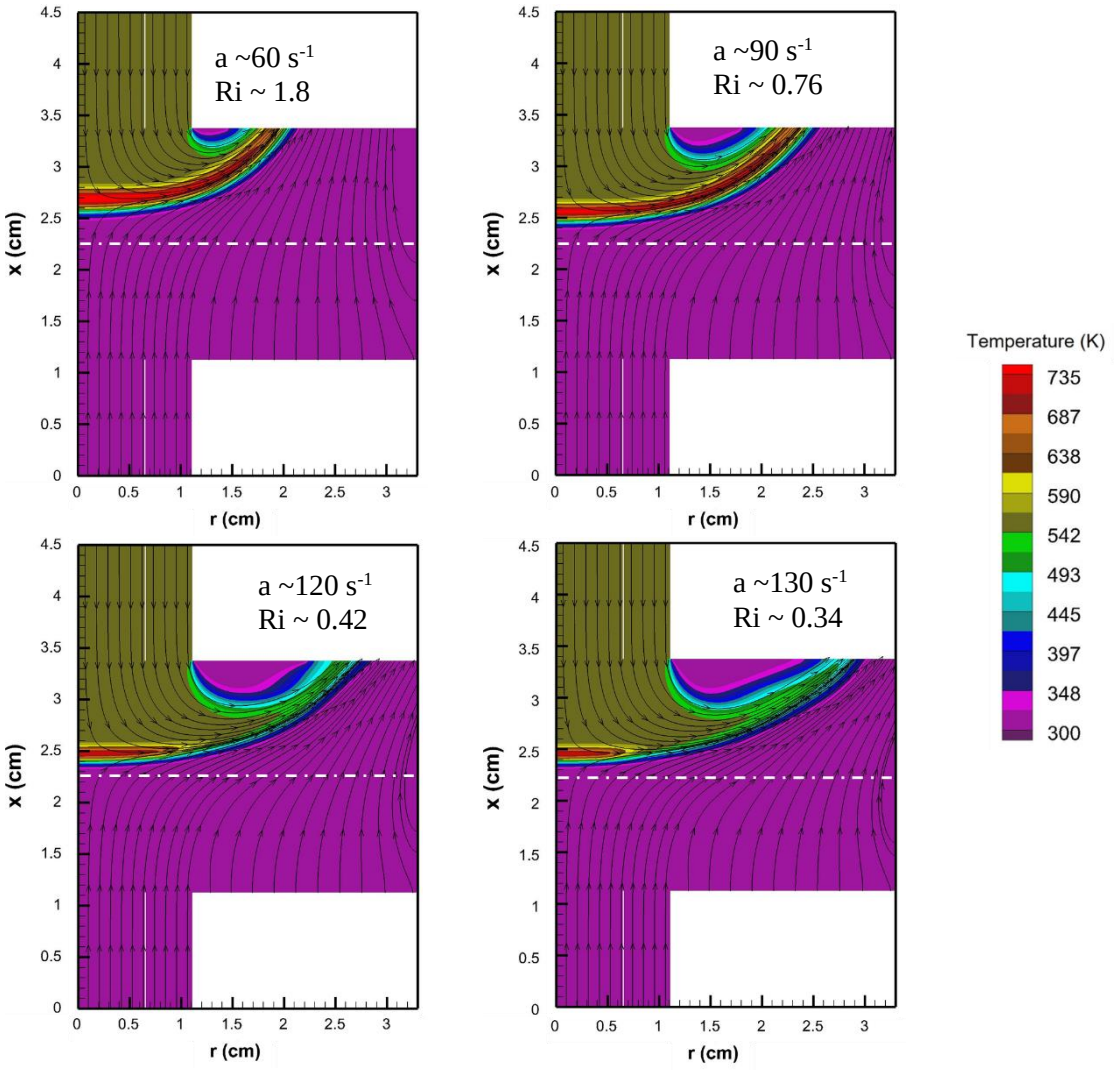

Figure 4.28: Temperature and streamline distribution of DME counterflow cool flame at different global strain rates (X_F = 0.587, p = 1 atm). Dashed-white line marks the midpoint of the centerline.

is significant. The flame is located at x ~ 2.7 cm, about 4.5 mm from the axis midpoint. As the global strain rate increases, the inertial effect becomes more prominent, and the flame shifts downward. At a ~130 s^{-1}(Ri ~ 0.34) the flame position is shifted to x ~ 2.4 cm (~1.5 mm from the axis midpoint). It is also worth noting that the flame structure changes significantly in both the axial and radial directions with the variations of the global strain rate. The flame becomes thinner and its spanwise length decreases dramatically as the

global strain rate increases. This is due in part to the N_2 co-flow, which affects flame propagation in the radial direction and diminishes the flame tip at higher strain rates. Simulations with a higher strain rate of ~137.5 s^{-1} for this fuel loading results in complete flame extinction.

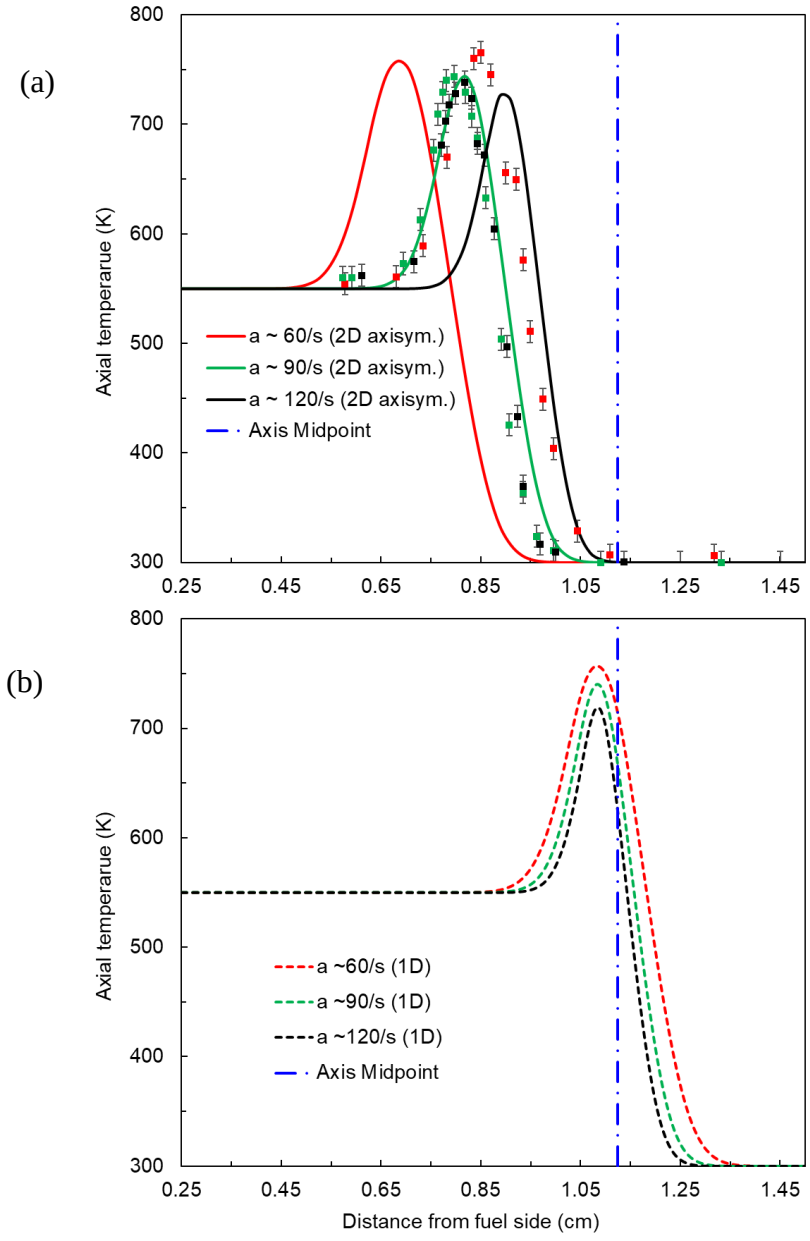

Figure 4.29: Comparison of the axial temperature distribution for different global strain rate conditions: (a) experiment (symbols) vs computed (2D axisym. OpenFOAM model with buoyancy), (b) computed (1D CHEMKIN OPPDIFF model). X_F = 0.587. p = 1 atm.

For further elucidation, the axial distribution of temperature at different global strain rates has been analyzed. The comparison between the 1D (CHEMKIN) and 2D axisymmetric (OpenFOAM, with buoyancy) model, along with experimental measurements, is shown in Fig. 4.29. Both models predict that the flame location is pushed farther from the fuel side as the global strain rate increases. The difference between the flame locations predicted by the 1D and 2D models is the largest (~ 4 mm).) at the lowest global strain rate studied (a ~ 60 s^{-1}). This difference tends to decrease as the strain rate increases. For a ~ 90 s^{-1} and ~ 120 s^{-1}, the difference is found to be 2.6 mm and 1.9 mm, respectively. This can be explained by the relationship of Reynolds and Richardson number with the global strain rate. The Reynolds number is proportional to the flow velocity, (i.e., global strain rate), while the Richardson number is inversely proportional to the square of the velocity (or the global strain rate). This means that as the global strain rate increases, the flow inertia increases linearly while the effect of buoyancy decreases quadratically. Since the 1D model does not consider the buoyancy effect, the difference in the flame location between the 1D and 2D models is greater at the lower strain rates and vice versa. Since the cool flame experiments are done in lower strain rates (i.e., higher Richardson numbers), multidimensional models with buoyancy effect are necessary to simulate them.

When compared with experimental data, the 2D model shows improved prediction of flame location in comparison to the 1D model. As shown in Figure 4.29, for the three cases presented (i.e., a ~60 s^{-1}, ~90 s^{-1} and ~120 s^{-1}) the average deviation of the peak temperature location between the measured and the computed values are ~2.67 mm and ~0.8 mm for the 1D and 2D models, respectively. Both models underpredict the peak centerline temperature, but the 2D model has a smaller discrepancy than the 1D model.

The average deviation of the peak temperature between the measured and computed values are ~11K and ~6K for 1D and 2D models, respectively. The deviation is higher at higher strain rates. The measured peak flame temperature is found to be 738K for a global strain rate of ~120 s^{-1}. 1D and 2D models underpredict the peak flame temperature by 20 K (i.e., T_{max} = 718 K) and 12 K (T_{max} = 726 K), respectively.

While the 2D model performs better than 1D in predicting the flame location, it is still not able to match the trend of the experimental data. The predicted trend of flame location vs. global strain rate can be explained by theoretical understanding of flow characteristics based on the Richardson number, however, it doesn't explain the experimental measurements. There is no physical interpretation provided in the experimental report for the variation of the measured flame location at different global strain rate conditions, making it difficult to understand the reason for the discrepancy between the 2D model predictions and the measurements.

Fig. 4.30 shows the peak axial (centerline) temperature as a function of the global strain rate for two different fuel loadings (X_F = 0.587 and X_F = 0.5) computed by 1D CHEMKIN and 2D OpenFOAM models. For both fuel loading conditions, the maximum temperature computed by OpenFOAM is higher than that computed by CHEMKIN. This is because the boundary conditions in the 2D model permit the thermal expansion of the flame to perturb the velocity profile at the nozzle exits, allowing the flame to push the incoming convective flux and expand the reacting zone. In contrast, in the 1D simulation, the flame is constrained by fixed boundary conditions, resulting in a thinner reacting zone with a steeper temperature gradient. For example, Fig. 4.31 compares the axial temperature gradient (|dT/dx|) for the 1D and 2D axisymmetric model prediction for a single case (X_{DME}

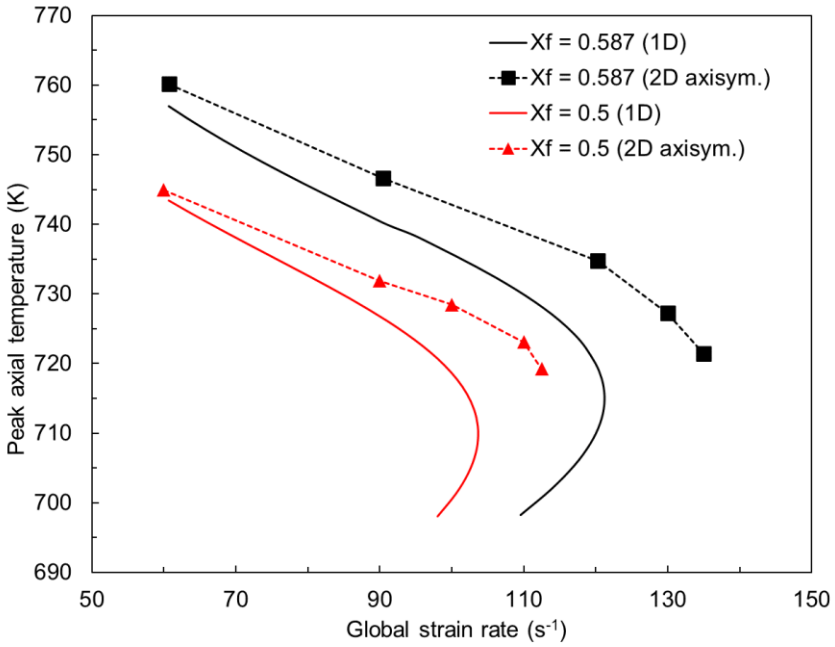

Figure 4.30: Comparison of predicted peak axial temperature as a function of global strain rate based on 1D (CHEMKIN OFFDIFF) and 2D axisymmetric (OpenFOAM, with buoyancy) model.

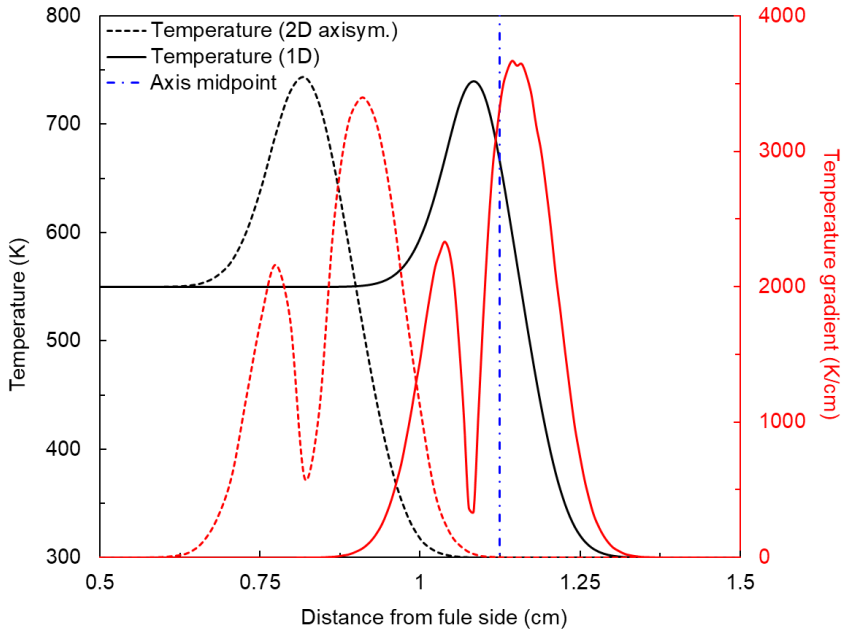

Figure 4.31: Computed axial distribution of temperature and temperature gradient for 2D (with buoyancy) and 1D simulation. DME cool flame (X_{DME} = 0.587, U_F = 62.3 cm/s, U_O = 50.9 cm/s, a ~ 90 s^{-1}).

= 0.587, a ~ 90 s^{-1}). The peak temperature gradients are approximately 3800 K/cm and 2300 K/cm for 1D and 2D simulations, respectively. As described in section 4.8.2., a higher temperature gradient across the flame leads to greater diffusive loss ($Q_{diffusion}$ ~ dT/dx) which reduces the overall flame temperature in 1D simulations.

Fig. 4.30 also shows that as the global strain rate increases, the difference in peak temperature between the 1D and 2D models becomes larger. For X_F = 0.587 the peak temperature difference between the two models is ~5K and ~16K at a ~ 60 s^{-1} and a ~120 s^{-1}, respectively. Similarly, For X_F = 0.5 the peak temperature difference between the two model is ~2.5 K and ~10K at a ~ 60 s^{-1} and a ~90 s^{-1}, respectively. This trend can be explained by examining the nozzle exit velocity perturbation caused by the cool flame, as shown in Fig. 4.32. The axial velocity gradient has been calculated at the nozzle exits at fuel-side $\left(\left. \frac{du_{ax}}{dx} \right|_{l=0} \right)$ and oxidizer-side $\left(\left. \frac{du_{ax}}{dx} \right|_{l=L} \right)$, where *l* is the distance from the fuel side nozzle exit. In all cases studied, the cool flame was observed on the fuel-side of the stagnation plane, resulting in the maximum perturbation of the nozzle exit velocity on the fuel-side. Consequently, the maximum perturbation of the nozzle exit velocity occurs at the fuel-side. At a global strain rate of ~60 s^{-1}, the axial velocity gradient at the fuel and oxidizer-side nozzle exits was approximately 25 s^{-1} and 1.5 s^{-1}, respectively. As the global strain rate increases, the flame is pushed farther from the fuel side due to higher inertia, but the axial velocity gradient continues to increase until it reaches a plateau as the flame location ceases to shift further. The increase in velocity perturbation with increasing global strain rate contributes to the discrepancy in peak flame temperature between the 1D and 2D model predictions shown in Fig. 4. 32.

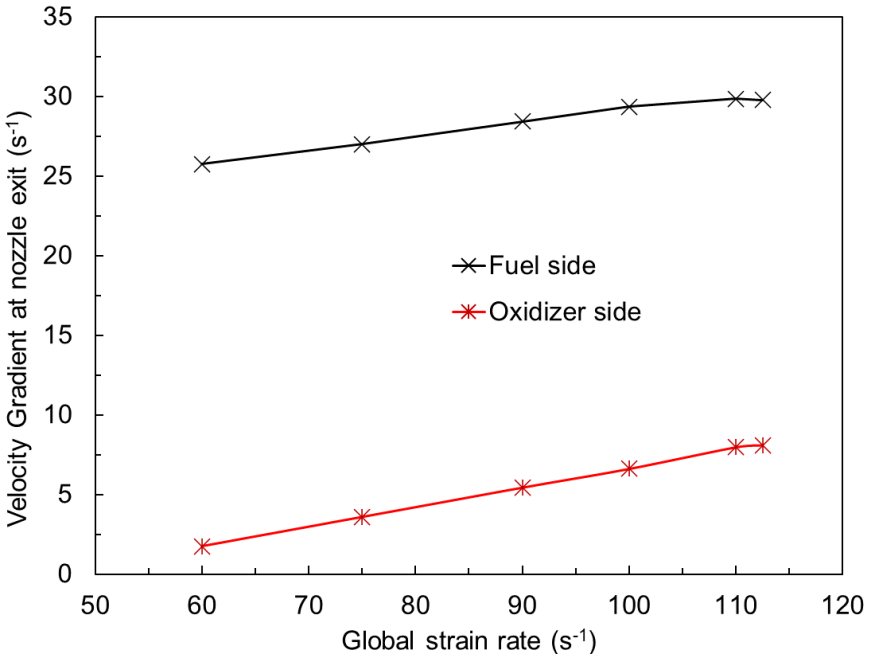

Figure 4.32: Axial velocity gradient at nozzle exits as a function of global strain rate (X_F = 0.5, p = 1 atm

The flame structure is affected by the global strain rate, as shown in Fig. 4.28 and Fig. 4.29. As the strain rate increases, the maximum flame temperature decreases, and the temperature profiles become thinner. For a quantitative understanding, the flame thickness is plotted as a function of global strain rate for a fixed fuel loading in Fig. 4.33a. The flame thickness was defined as the width of the maximum temperature gradients on the centerline, as shown in Fig. 4.33b. In both 1D and 2D simulations, the flame thickness decreases exponentially with the global strain rate. Slight deviation at the high strain rate is observed because of the sharp decrease in peak flame temperature near the extinction limits. Flame thickness predicted by the 2D model is greater than that by the 1D model. The 2D model predicts a greater flame thickness than the 1D model, with the difference between the two being larger at lower strain rates and vice versa. At lower strain rates, the buoyancy effect is more significant, and the 1D model does not take it into account, leading

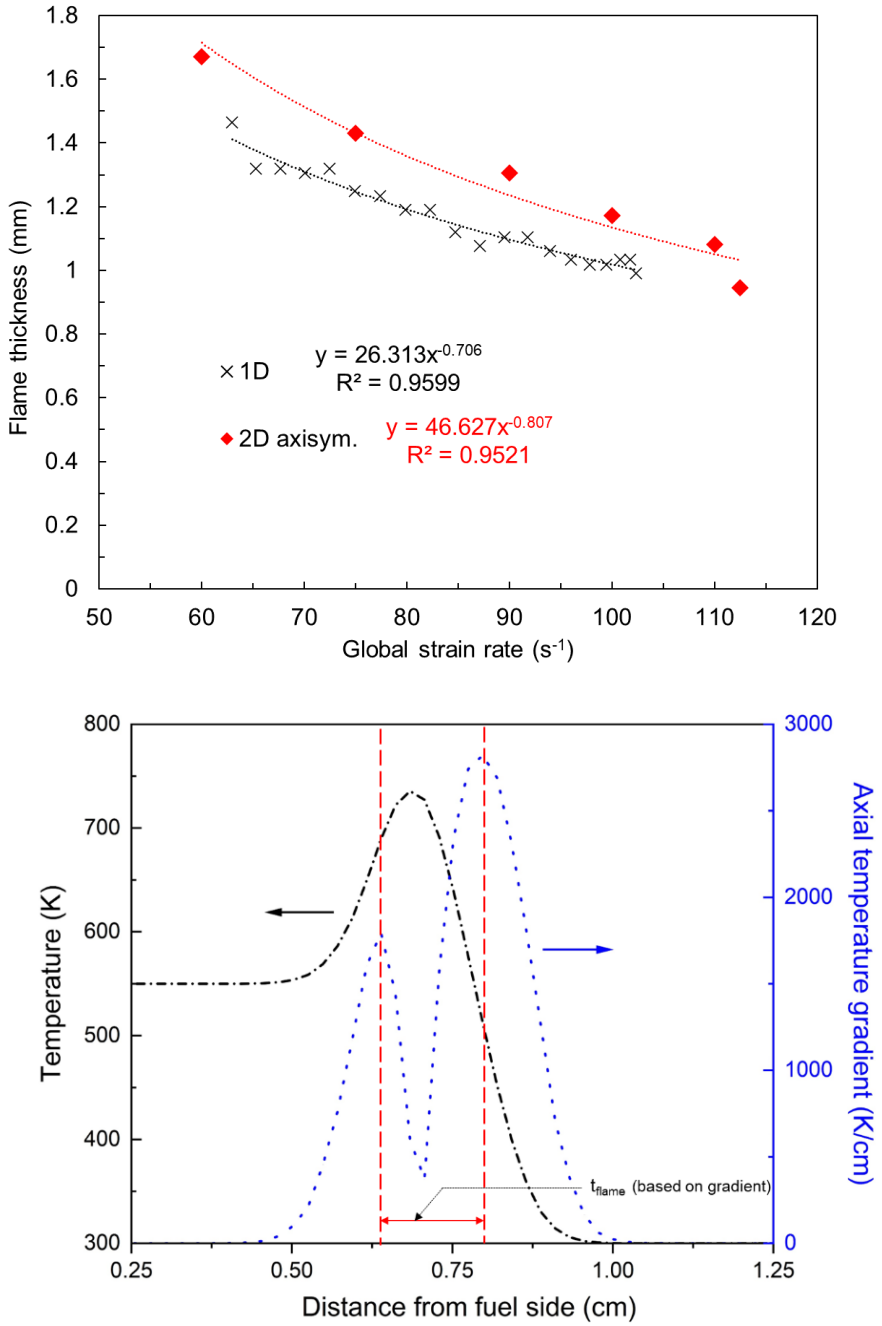

Figure 4.33: (a) Flame thickness as a function of global strain rate for 1D (CHEMKIN OPPDIFF) and 2D axisymmetric (OpenFOAM with buoyancy) simulation. (X_F = 0.5, p = 1 atm), (b) depiction of the definition of flame thickness considered in this study.

to a larger difference in the flame structure predictions between the 1D and 2D models. At a strain rate of ~75 s^{-1}, the flame thickness predicted by the 2D model is approximately

1.43 mm, which is approximately 15% larger than the 1D prediction (~1.248 mm). At a strain rate of approximately 100 s^{-1}, the difference is ~10%. It is important to note that in the 2D simulation, a stable flame was observed at a strain rate of ~112.5 s^{-1} while the flame extinguished beyond a global strain rate of ~100 s^{-1}.

The influence of global strain rate on the flame structure is further investigated by analyzing the distribution of the key species associated with the DME cool flame. Fig. 4.34 shows the centerline distribution of CO, CO_2, CH_2O, QOOH, O_2QOOH, CH_3OCH_2, $CH_3OCH_2O_2$ at various global strain rate conditions. Both CO and CH_2O, which are major products of low-temperature oxidation and form near the center of the reacting zone (see Fig. 4.22a), decrease with the increase of the global strain rate (Fig. 4.34a and 4.34c, respectively). The peak formaldehyde mole fraction decreases from ~52000 PPM (i.e., X_{CH_2O} ~ 0.052) to ~40000 PPM (i.e., X_{CH_2O} ~ 0.04), when the global strain rate is varied from ~60 s^{-1} to ~112.5 s^{-1}, i.e., a reduction of approximately 23%. Similarly, the peak CO mole fraction decreases from ~15000 PPM (i.e., X_{CO} ~ 0.015) to ~8500 PPM (i.e., X_{CO} ~ 0.0085) i.e., a reduction of approximately 23%. On the contrary, the peak CO_2 mole fraction increases from ~3500 PPM (i.e., X_{CO_2} ~ 0.0035) to ~4100 PPM (i.e., X_{CO_2} ~ 0.0041) i.e., an increase of approximately 17%. This is because the flame is pushed away from the oxidizer side by the higher inertial effect at higher global strain rates, exposing it to more oxygen-rich conditions. As a result, a significant amount of CO is converted to CO_2 due to the abundance of oxygen. Peak QOOH also increases about 90% but more QOOH converts to O_2QOOH due to higher presence of the oxygen. The peak O_2QOOH

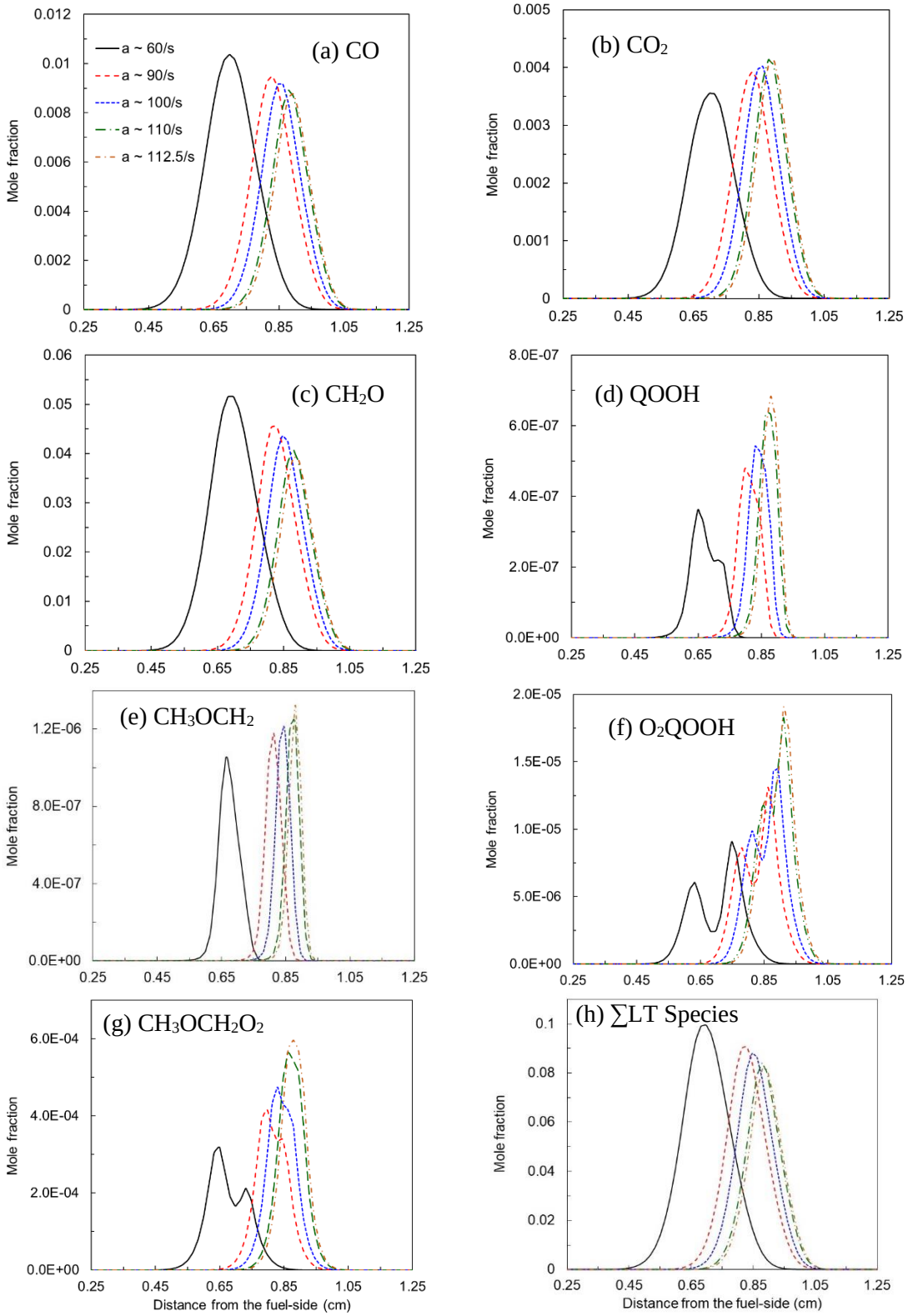

Figure 4.34: Centerline distribution of major low-temperature (LT) species of DME cool flame for different global strain rate conditions. 2D axisym. simulation, X_F = 0.5, 1 atm.

shows an increment of ~111% (from ~9 to ~19 PPM). The distribution of QOOH (Fig. 4.34d) further shows that the dual peak-like structure (a primary and a secondary peak on the fuel and oxidizer side, respectively) becomes thinner and diminishes to form a single peak at higher global strain rates. This is due to the increased conversion of QOOH to O_2QOOH as the reacting zone is pushed towards the oxidizer side. On the other hand, the double spike-like structure of O_2QOOH persists as the global strain rate increases but becomes thinner overall. As the global strain rate increases, the formation of methoxymethyl peroxy ($CH_3OCH_2O_2$) is also boosted due to the increase conversion of methoxymethyl (CH_3OCH_2) in the presence of abundant oxygen as the flame moves towards the oxidizer side. In summary, as the global strain rate increases, the flame structure changes due to the decrease in the stable products of low-temperature oxidation, such as (CO and CH_2O). This results in a reduction in the flame thickness initially. However, intermediate species like QOOH, O_2QOOH, and $CH_3OCH_2O_2$ increase in concentration on the oxidizer side as flame approaches the near-limit condition. As a result, the flame thickness i.e., width of the reacting zone levels off before it completely extinguishes. Because of this, the flame thickness shows an exponentially decreasing trend with the global strain rate.

4.9.5 Extinction Strain Rates of DME Cool Flame

The extinction limit for a DME cool flame at atmospheric pressure was computed and compared to experimental measurements by [25] in Fig. 4.35. To perform the extinction analysis in CHEMKIN, the Flame Extinction Simulator with the arc-continuation method [145] was used. In OpenFOAM, the global strain rate was gradually increased by adjusting the velocity boundary conditions at the fuel and oxidizer inlets,

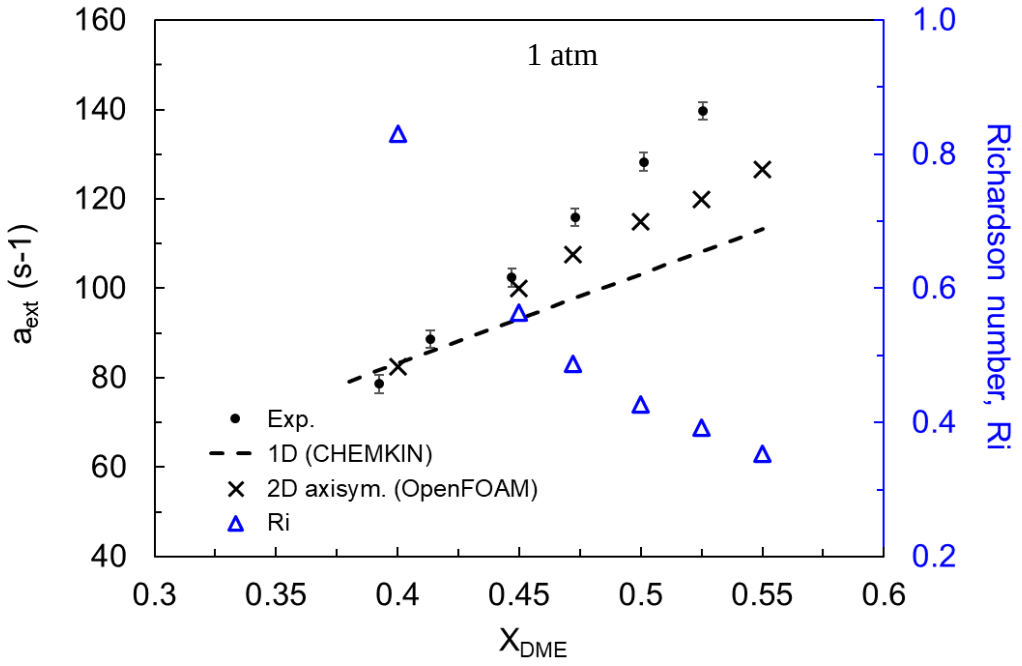

Figure 4.35: Comparison of measured and predicted extinction strain rate of DME counterflow cool flame as function of fuel loading (p = 1 atm)

while maintaining momentum balance, until the flame extinguished. The extinction strain rate (a_{ext}) increases with the fuel loading in a linear fashion. This is because as the fuel loading increases, the chemical heat release also increases, requiring a higher convective effect (i.e., strain rate) to extinguish the flame. The 1D and 2D model (with buoyancy) predictions deviate from the measured value at higher fuel loading conditions (i.e., X_F > 0.48), but the OpenFOAM model performs significantly better than the CHEMKIN 1D model in predicting the global extinction strain rate. For a fuel loading of X_F = 0.525, the difference between measurement and the 1D model prediction is ~40 s^{-1} (~30%), while the 2D model prediction is within 14% (~19 s^{-1}) of the measured extinction strain rate. The difference in the predictions can be attributed to the difference in peak flame temperature, with the 1D model underpredicting the peak flame temperature by a larger margin compared to the 2D model. For a fuel loading X_F = 0.587, the measured peak flame

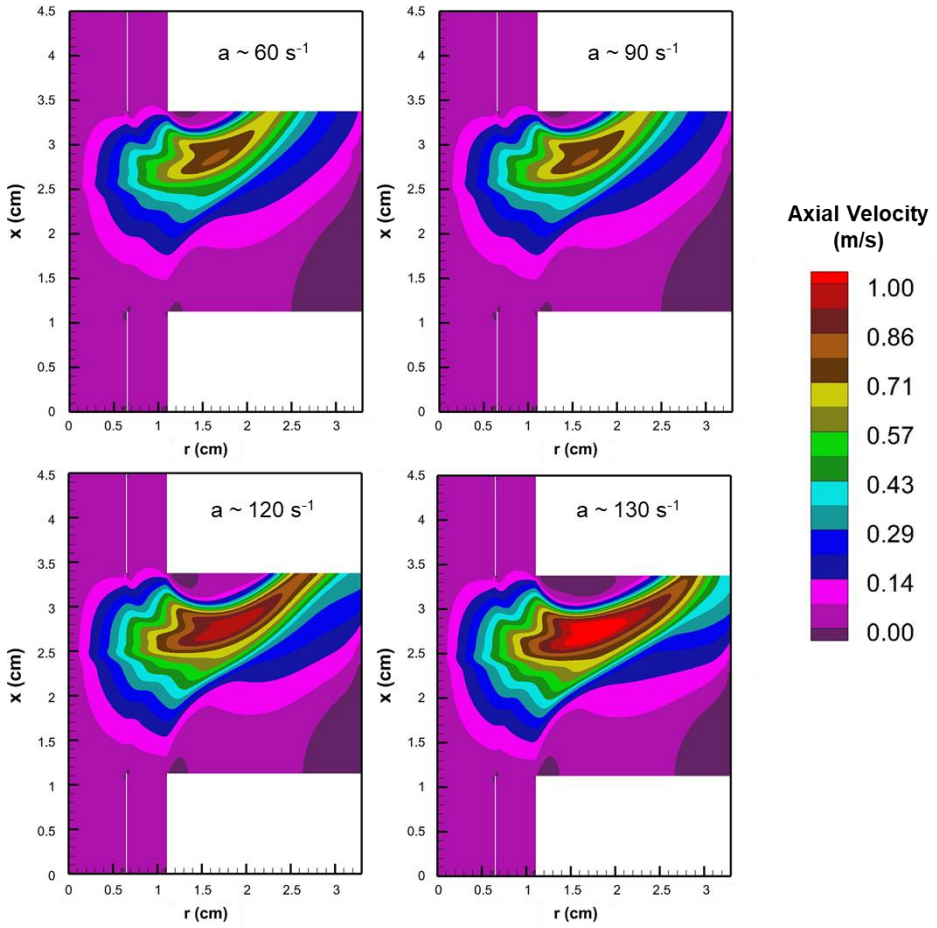

Figure 4.36: Axial component of the velocity of DME counterflow cool flame at different global strain rates (X_F = 0.587, p = 1 atm).

temperature is found to be 738K for a global strain rate of ~120 s^{-1}. 1D and 2D models underpredict the peak flame temperature by 20 K (i.e., T_{max} = 718 K) and 12 K (T_{max} = 726 K), respectively. It is worth noting that even though the 2D model performs better than the 1D model in predicting the global extinction strain rate, there are still deviations between the predictions and measurements. These deviations may be due to various factors such as differences in the assumed chemical mechanisms and uncertainty in the experimental measurements at higher strain rates. Fig. 4.36 shows the contours of the axial component of the velocity for different strain rate conditions at a fixed fuel loading. With the increase

of the strain rate (i.e., velocity), length of the entrainment zone (exhibited by the negative value of the axial velocity) near the co-flow outer region increases. Flame is affected by this ambient entrainment as it continues to exist along that region (see Fig. 4.28). So, at higher fuel loading, the predicted flame extinguishment may be affected due to the entrainment effect occurred at higher strain rates. Simulations have been conducted by increasing/decreasing the co-flow velocity by 10-20%. It resulted from the modification in flame structure near the tip to a complete extinguishment, exhibiting sensitivity towards co-flow velocity. Experimental uncertainties from the co-flow adjustment may be another reason for the discrepancy between measurement and predictions at higher strain rates. Further analyses can be performed should more experimental data become available.

Simulations were conducted at elevated pressures (3 and 5 atm) to examine the extinction limit of DME cool flames in a counterflow configuration. Results indicate that the extinction strain rate increases at elevated pressure. This is expected because molar concentration of the reactants are higher at elevated pressure [146] In particular, the cool flame extinction strain rate is proportional to *n*th power of oxygen, i.e., $[O_2]^n$ [80]. In their recent work on DME counterflow cool flame experiment at elevated pressure, Wang et al. [147] reported that the low temperature pathways, .i.e., oxygen addition to methoxymethyl radical (rxn #812 $CH_3OCH_2 + O_2 = CH_3OCH_2O_2$) and QOOH (rxn #821: $QOOH + O_2 = O_2QOOH$), are enhanced by increasing pressure.

Figure 4.37a illustrates the extinction strain rate of DME cool flames for 3 atm pressure as computed by both 1D and 2D (with buoyancy) models. It is observed that at 3 atm, the extinction strain rate predicted by the 2D model displays two distinct trends. At

low fuel loading (X_F = 0.1 to 0.2), the trend is similar to that observed at atmospheric pressure, with the 2D model predicting a higher extinction rate than the 1D model. However, as the fuel loading is further increased, the 2D model predictions appear to

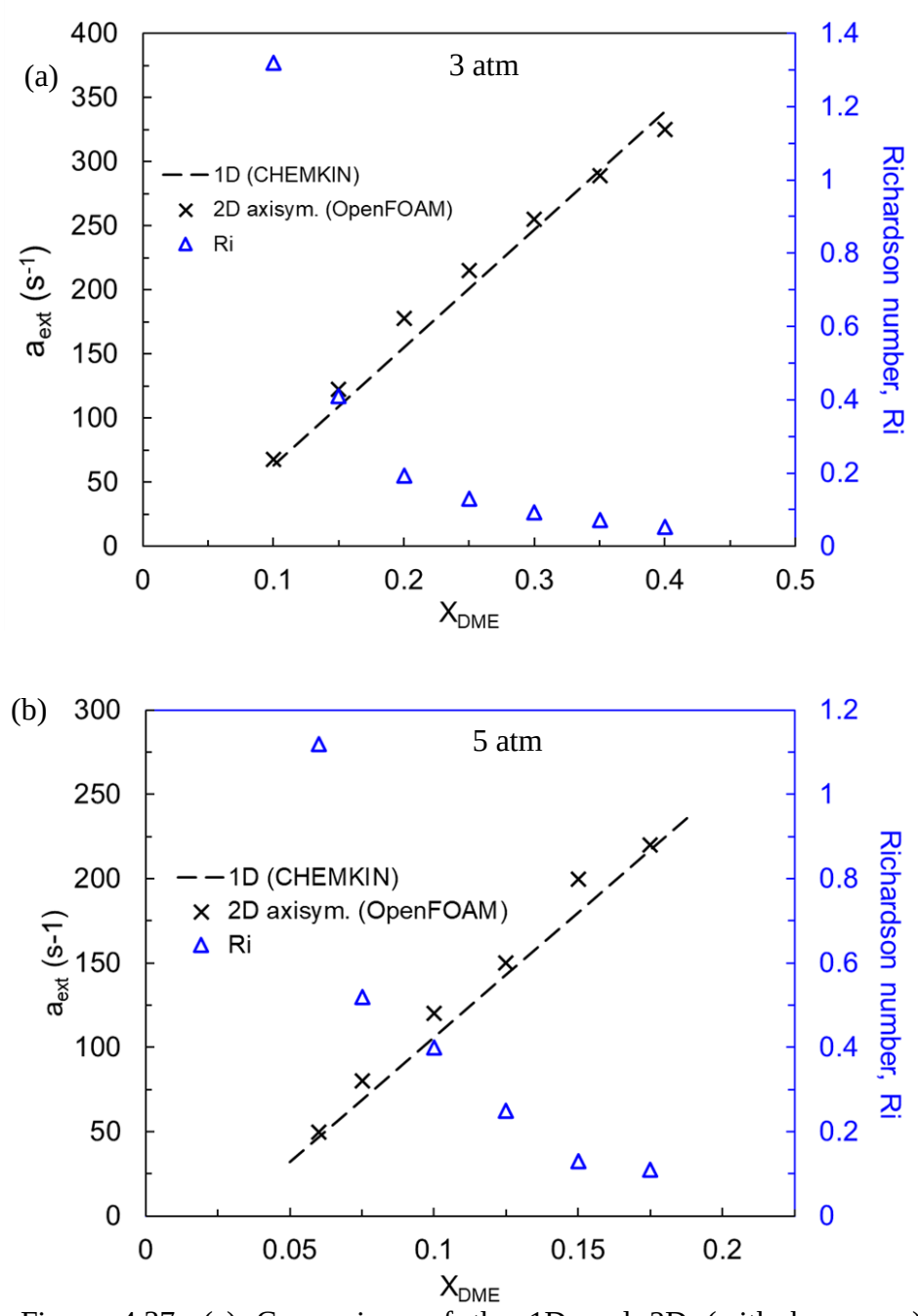

Figure 4.37: (a) Comparison of the 1D and 2D (with buoyancy) prediction on DME extinction strain rate (a_{ext}) at (a) 3 atm an d (b) 5 atm.

approach closer to the 1D prediction. To understand this phenomenon, the Richardson numbers were plotted on the secondary y-axis. At elevated pressure, the cool flame extinction rate increases. For a fuel loading of 40% (X_F = 0.4), the extinction strain rate at 3 atm (~340 s^{-1}) is four times higher than that at 1 atm (~82 s^{-1}). As fuel loading increases, higher convective flux (i.e., Reynolds number) is required for the flame to extinguish. As Reynolds number (i.e., the global strain rate) increases, Richardson number decreases dramatically, due to the inverse proportionality between these two numbers (as per Eqn. 4.1 and 4.2). As a result, the influence of buoyancy decreases substantially with increasing strain rate. For a global strain rates above ~ 175 s^{-1}, the Richardson number drops below ~ 0.1, indicating that the system approaches a scenario that can be approximated by a quasi-1D model, which assumes high Reynolds number configurations and disregards any buoyancy effect. As a result, predictions from the 1D and 2D models become similar. In the simulations conducted at 5 atm pressure, as depicted in Fig. 4.37 (b), the 1D and 2D predictions converge as the multidimensional effects become negligible at high strain rates. Fig. 4.38 illustrates the flame structure under high pressure conditions for three distinct

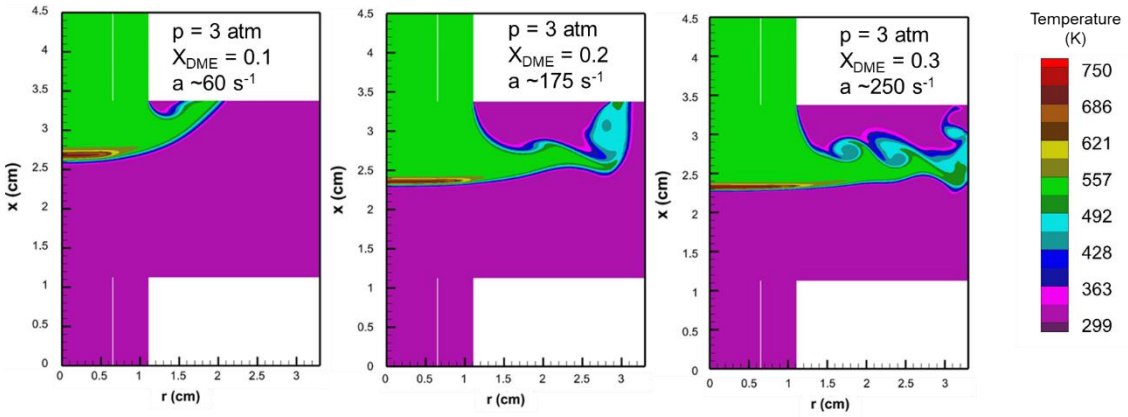

Figure 4.38: Temperature contour of DME cool flame at 3 atm for different fuel loading and strain rate conditions.

strain rates. The results suggests that at higher strain rates, the flame becomes flatter, and the radial dependence of the flame structure diminishes.

4.10 SUMMARY AND CONCLUSION

In summary, the current chapter presented numerical analyses of the non-premixed cool flame formation of dimethyl ether (DME) combustion in a counterflow geometry. By performing two-dimensional axisymmetric simulations over a range of parameters such as fuel loading, global strain rate, and pressure, the study aimed to investigate and understand the critical features of DME oxidation at low temperatures, including flame structure, extinction strain rates, species distribution, and chemical characteristics. The goal of the study was to gain insight into the effect of multidimensional transport in the formation of non-premixed cool flame in a counterflow geometry and its deviation from ideal conditions that cannot be predicted by quasi-1D theory-based numerical models. It was found that the predictions of the 2D-axisymmetric model were in better agreement with experimental measurements compared to the quasi-1D model predictions.

One of the key findings of this study is the identification of the Richardson number as a critical parameter for characterizing the system. Unlike hot flames, cool flames require much lower strain rates to sustain. At lower strain rates (a = 60~150), the Richardson number is relatively high (0.1~1.5); thus, the flame is predominantly located near the upper burner due to the buoyancy effect. As the global strain rate increases, flow inertia begins to dominate over the buoyancy effect (Ri <~0.1), and the stagnation plane gradually moves towards the axis central location due to momentum-balanced boundary conditions. This highlights the importance of considering the relative importance of buoyancy and flow

inertia in determining the flame location in low-temperature combustion in counterflow geometries.

The deviation from the ideal plug flow condition in the counterflow burner comes from the uncertainties associated with the velocity perturbation at the nozzle exits due to the thermal expansion caused by the flame. The 2D model resolves this perturbation without imposing any radial velocity gradient at the nozzle exits. As a result, it allows the flame to sustain a global strain rate higher than that of the 1D model. Thus, the extinction strain rate predicted by the 2D model is higher than that by the 1D model, and this deviation increases with the increase of the global strain rate up to certain value. This is due to the increased axial velocity gradient at the nozzle exits as the global strain rate increases, deviating further from the ideal plug flow conditions and making the adequacy of the 1D model questionable. By incorporating multidimensional transport, the current 2D model demonstrates its effectiveness in simulating cool flame formation in counterflow geometry in a self-consistent manner, highlighting the importance of considering multidimensional transport effects in modeling such combustion processes.

The model was extended to study the cool flame extinction at high-pressure conditions. At elevated pressures, the cool flame is able to sustain relatively higher global strain rates due to its increased reactivity. Two distinct trends in extinction strain rates were observed for different fuel loading at 3 and 5 atm pressures. At 3 atm, the extinction strain rate increases with fuel loading up to X_F ~0.2. Beyond that point, the rate of increase in extinction decreases and the 2D model prediction becomes similar to that of the 1D model prediction. At 5 atm, the transition is observed at a fuel loading X_F ~0.125. It can be inferred that the reduction in Richardson numbers leads to conditions where the assumption of high

Reynolds numbers in the quasi-1D theory becomes valid, and the multidimensional effect can be neglected when modeling cool flame under such conditions.

In conclusion, this chapter has provided valuable insights into the dynamics and structures of cool flame formation in a counterflow geometry by numerical simulations. The 2D axisymmetric model used in this study is a more suitable model for studying the flame formation and extinction of DME due to its ability to capture multidimensional transport effects. The findings of this research can be used as a foundation for future numerical modeling studies of reacting flow simulations of cool flame formation. Additionally, this work has advanced the current knowledge and understanding of cool flame diffusion in counterflow geometries, and it can be expected that the results and findings will appeal to further research in this field.

CHAPTER 5: HYDROTHERMAL FLAME OF METHANOL OXIDATION IN SUPERCRITICAL WATER

5.1 INTRODUCTION

Supercritical water oxidation (SCWO) is considered a promising technology for hazardous wastewater treatment and energy reclamation [148-150]. It is an advanced combustion process that involves the formation of a sustainable flame (generally known as the hydrothermal flame) in aqueous environments at conditions above the critical point of water, P > 221 bar, and T > 374°C. The hydrothermal flame was first described by Schilling and Franck [151], who reported that the high miscibility of the reacting species in supercritical water (SCW) conduces the overall chemical conversion. At this extreme condition, organic compounds exhibit complete solubility in water [152]. Hence, they can be efficiently oxidized and converted into inorganic precipitation out of the solution. The hydrothermal flame can act as an internal energy source facilitating this oxidation process. SCWO poses significant environmental advantages because of its capability to recover energy and reclamation of water without generating NO_x and SO_x particles, which involves further treatment processes [153].

Figure 5.1 shows the phase diagram of water and its physical at 250 bar. Due to the high compressibility, the density of water is highly dependent on pressure near the critical

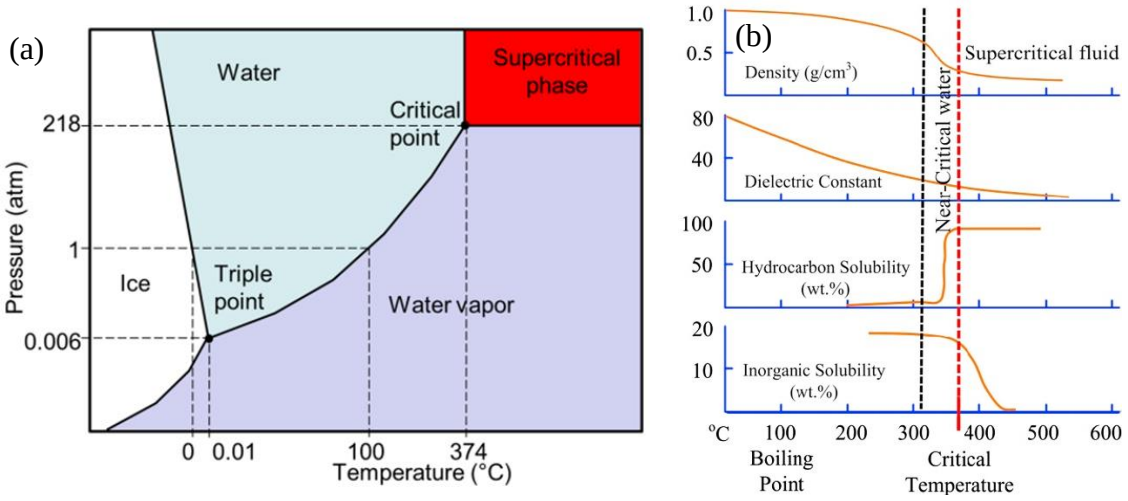

Figure 5.1: (a) Phase diagram of water [154], (b) physical properties of water at 250 bar [155]

point. So, a drastic reduction in pressure is observed. At the supercritical condition, the water density is $\lesssim 0.3$ g/cm^3, i.e., similar to the gas density [156]. The dielectric constant decreases from ~80 to $\lesssim 6$ at and above critical point [157]. Due to this low dielectric constant, water becomes non-polar and exhibits miscibility with organic compounds and non-polar gases but poor solubility to inorganic salts [158, 159]. Additionally, viscosity is lower, and diffusivity is higher in supercritical conditions, allowing for reactions to take place at high velocities and without mass transport limitations [160]. Furthermore, the interphase mass transfer resistance is diminished or eliminated in SCW, which allows reactions to proceed homogenously [161, 162]. This results in a very small conversion time scale (in the order of milliseconds), achieving approximately 99.999% chemical conversion efficiency [163]. Additionally, the process eliminates NOx and SOx pollution by depositing and filtering salt from the reactive flow [164]. Thereby, SCWO poses a crucial technical advantage in addressing the waste management challenges in various applications. It is considered a green technology due to its high energy recovery, especially

at higher operation temperatures. [162, 165, 166]. SCWO is an effective method for treating various types of organic waste. The technology is particularly useful for extraterrestrial waste recovery [149, 167] and urban sewage sludge processing [155, 168, 169]. Other innovative applications of SCWO include hydrothermal spallation drilling [170, 171], hydrothermal jet drilling[172], upgradation of heavy oil [173], extraction of bio-crude from bio-fuels [174], nuclear waste disposal [175], low power consuming coal gasification cycle [176, 177], hydrogen production from oil gasification [178], disposal of recalcitrant contaminants [179], specialty materials preparation by hydrothermal synthesis [180-182] etc. Figure 5.2 presents an overview of some of the exotic and unique applications of hydrothermal flames.

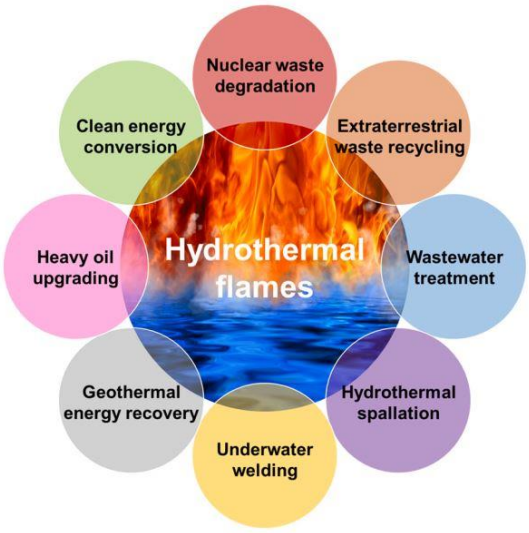

Figure 5.2: Several unique applications of SCWO and hydrothermal flames [149]

Despite the many potential benefits of SCWO, the fundamental aspects of reacting flow systems under high pressure conditions are not well understood. One major challenge in studying SCWO is that gases deviate from ideal gas behavior at high pressures, which

can make numerical simulations more complex [183]. Additionally, since reactions in SCWO are dominated by mixing phenomena, it is important to take into account the multidimensional aspects of the reacting flow system [184]. To address these challenges, there is a need for a more comprehensive understanding of the reaction chemistry, coupled with the use of real gas models and multidimensional transport simulations. In this chapter, the hydrothermal flame of methanol oxidation in supercritical water medium has been investigated. The scope of the current study, as well as a review of relevant literature, is presented in the following section. Next, a detailed explanation of the modeling approaches and simulation results are presented. Finally, results and analyses are presented to understand the effect of multidimensional transport on flame formation and extinction. Overall, the goal of the chapter is to improve the understanding of the multidimensional aspects of hydrothermal flame formation in the supercritical reactors.

5.2 Recent Works on Hydrothermal Flame

The lack of reliable measurement and diagnostic methodology at extreme high-pressure systems is one of the main impediments to our understanding of the key features of the supercritical reactor and hydrothermal flame arrangements. In recent years, several studies have been conducted to understand the fundamental process involved in SCWO, mostly centered on experimental investigation and phenomenological observation. Hicks et al. [167, 185] described the earlier experiments conducted by NASA to examine the ignition of SCWO in drop-rig setup with various fuels, e.g., methanol, methane, etc. They explored the possibility of applying hydrothermal flame to oxidize the human metabolic waste produced in the space shuttle. In their primary research at NASA Glen Research Center (GRC), Ames Research Center (ARC) and experiments carried out in International

Space Station in a long-duration microgravity environment. It has been found that a self-sustaining flame can be generated in a supercritical aqueous stream to oxidize the dissolved harmful organic compound. In continuation of this exploration, their latest experimental effort [153] investigated hydrothermal ethanol flames in co-flow jets and reported the pre-ignition, ignition, and stabilization process. They observed hydrothermal flame as a luminous reacting zone for a 50%-v fuel flow at 2ml/min. Reddy et al. [186] attempted to understand the critical steps of the ignition mechanism of n-propanol-air hydrothermal flame and proposed an ignition map for the flame initiation. They reported an optimal fuel concentration (2.4 wt% at 360 ^{o}C) to initiate a sustainable flame for a particular condition. They also concluded that the buoyancy effect ceases to exist as the reactor transforms from the near-critical to the supercritical stage. Cabeza et al. [165] presented a cooled wall reactor design to investigate the performance of a propanol-air hydrothermal flame. They reported a total elimination of organic and nitrogen compounds from the stream without preheating the feed. Bermejo et al. [187] demonstrated isopropyl-alcohol (IPA) hydrothermal flame in their experimental study. They studied the operation parameters (i.e., feed flow, injection temperature, and fuel concentration) and the geometric parameters of the injectors. A minimum of 4 wt% IPA was fed into the reactor to maintain a stable flame, and the total organic carbon (TOC) was found to be less than 20 ppm in the effluent.

5.3 Scope of Current Work

While the concept of supercritical combustion/oxidation has been known for decades, it has recently received increased attention because of its importance in high-efficiency power generation (e.g., Allam cycle [188], where supercritical carbon dioxide is

used as working fluid) and also as a potential process for recovering energy and reclaim water from wet waste streams (e.g., Hydrothermal flames). This technology has notably garnered attention for its applicability in waste management during a space exploration mission. Especially, studies on supercritical fluids onboard the International Space Station [189] under a collaboration between NASA-CNES (French Space Agency) have further intensified the interest in advancing hydrothermal flame [190, 191].

During space missions, a substantial amount of organic waste is produced that requires proper management. The waste is generally wet and composed of human excreta, disposed food, and drinks. Hick et al. [153] reported that approximately 6.8 Kg to 9.6 Kg of waste is generated by each astronaut daily. This waste is hazardous, biologically unstable, consumes a large amount of space, and poses huge logistical challenges in the preparation and organization of extra-terrestrial exploration. Therefore, sustainable technological development is required to reduce the frequency of re-supply missions and the considerable cost associated with it, and that can achieve resource reclamation from water and wet waste streams. SCWO has been considered a viable technique to mitigate this challenge.

Very few studies are available in the literature that reported on the numerical investigation of SCWO. This is because modeling combustion processes at very high-pressure conditions are still challenging. Most importantly, a suitable real gas model is required to predict the species' behavior under the supercritical state. Especially in diffusion flame formation at high-pressure conditions, the real gas effect has been found to be one of the dominant features in predicting the flame location and structure [192]. One of the early CFD models of a steady-state SCWO was presented by Oh et al. [193], where

the SCWO of isopropanol was simulated for a multi-dimensional domain. The modeling results provided insight into the distribution of the chemical components, temperature distribution, and salt particle trajectories. Zhou et al. [194] developed a CFD model to simulate methane oxidation in co-axial supercritical reactor arrangements and extended their model to three-dimensional simulations. Due to the unavailability of a detailed kinetic mechanism, they used data fitted global reaction kinetics from Webley and Tester [195]. Narayanan et al. [196] presented both experimental and numerical investigations on methanol oxidation at 700K and 250 bar conditions. They compared the predicted and simulated temperature distribution under different fuel loading conditions. A single-step reaction mechanism was utilized to model the oxidation process. In contrast, the eddy dissipation model was used to resolve turbulence combustion interaction, assuming that the conversion is dominated by turbulent micro-mixing (not by inter-species transport). Similar strategies were employed to simulate higher-order alcohol-air hydrothermal flame by Queiroz et al. [197] and Reddy et al. [198] for isopropanol and n-propanol, respectively. While these numerical efforts employing the modified global kinetics have captured the global trend of the process, they failed to explain the disagreements with experimental measurement in numerous cases. Moreover, insights into the critical features of ignition properties and flame structure could not be elucidated.

Although limited, there have been some recent advancements in hydrothermal flame modeling due to the advent of high-performance computing and numerical packages that can couple multi-step chemical kinetic model and real gas effect in computational fluid dynamics analyses. In a recent study, Song et al. [27, 28] conducted a two-dimensional direction numerical simulation to study the auto-ignition characteristics of hydrogen-air

hydrothermal flame by employing a multi-step chemistry of 8 species and 19 reactions. One-dimensional counterflow diffusion flame of hydrothermal methanol combustion was investigated by Ren et al. [199]. A 23-species mechanism adjusted from Li et al. [200] was employed. Both the effort from these researchers reiterated the importance of multi-step chemical mechanisms to understand the development and evolution of hydrothermal flame. In a recent study, Mansfield et al. [183, 201] investigated methanol combustion in low temperature (375 to 475 ^{o}C) supercritical water in a batch reactor. While the experimental results generally supported the Mansfield chemical kinetic model of methanol combustion, the model overpredicted the measured methanol yield ($[MeOH]/[MeOH]_{initial}$).

The selection of chemical compounds for research on hydrothermal flames is limited due to a lack of understanding of chemical kinetics at high pressure conditions. The fuels most thoroughly studied for reacting flow system include hydrogen, methane, methanol and ethanol [183]. Among these compounds, methanol (CH_3OH) has been particularly well-studied due to its chemical kinetic compactness [202]. Additionally, methanol has garnered interest for its diverse applications in various fields, biomass-to-energy processes [203], hydrothermal liquefaction [204], and as an organic solvent [149]. This study conducted multi-dimensional simulations of hydrothermal flame of methanol combustion employing a detailed chemical kinetics scheme. The goal of this study is to explore the differences and similarities between predictions made using detailed and single-step chemistry, in order to gain a deeper understanding of the behavior of the hydrothermal flame and the underlying chemical kinetics.

5.4 Computational Domains and Simulation Parameters

The computational geometry for the numerical study is based on an existing wall-cooled hydrothermal burner reactor (WCHB-3) developed at ETH Zurich [171, 205, 206]. The experimental setup and computational geometry are illustrated in Fig. 5.3. The WCHB-3 combustion chamber is formed by a quartz glass cylinder with an inner and outer diameter of 8.5 mm and 10 mm, respectively. Inside the chamber, a methanol-water mixture is mixed with an oxygen stream, resulting in a hydrothermal flame combustion.

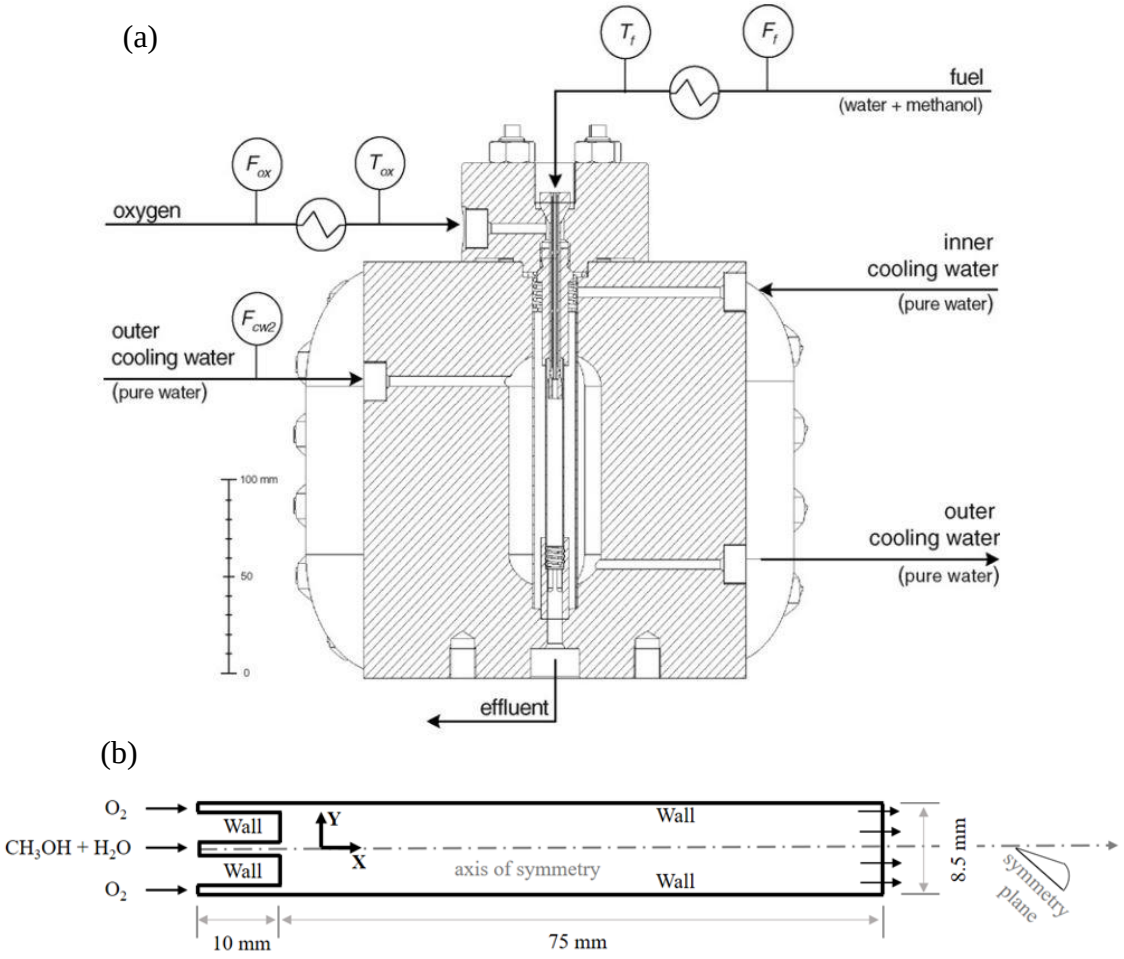

Figure 5.3: (a) Sectional view of WCHB-3 reactor, (b) schematic illustration of the modeled supercritical reactor (not in scale)

The computational geometry (Fig. 5.3b) is designed to replicate the WCHB-3 combustion chamber, with a co-axial burner configuration where the fuel and water mixture is injected through a central orifice of 1.6 mm in diameter, and oxygen is injected through an outer annulus with an inlet and outlet diameter of 6 mm and 8.5 mm respectively. The total length of the reactor is 75 mm, with an additional 10 mm of development length provided at the initial stage.

Simulation has been conducted for different loading of fuel and water mixture. The details of the parameters that have been used in the simulation are summarized in Table 5.1. All the dimensions and parameters have been chosen according to the experimental conditions provided in [196].

Table 5.1: Parameters and boundary conditions for numerical modeling

Boundary	Velocity (m/s)	Pressure (bar)	Temperature (K)	Mole fraction
Fuel + water inlet	7	250	700	X_{MeOH} = 0.07~0.12 X_{H_2O} = 0.93~0.88
Oxygen inlet	0.16	250	700	X_{O_2} = 1

5.5 MATHEMATICAL AND NUMERICAL MODELING

The mathematical model consists of steady state equations of compressible mass, momentum, enthalpy, and species conservation described in chapter 2. For resolving the turbulence effects a $k-\epsilon$ model has been employed with recommended value of 0.9 for Pr_t [28]. Peng-Robinson (PR) cubic EOS [33] has been implemented to take account of the real gas effect in supercritical conditions. For computation of the critical properties of real-gas mixture, we have employed a pseudocritical method [37, 38]. Pseudocritical rules provide a means to determine reduced properties for mixtures from the corresponding state

properties of the individual species. The detailed descriptions of the conservation equations, turbulence and real gas modeling are presented in Chapter 2.

The conservation equations have been discretized in the finite volume method (FVM) presented in chapter 3. The first-order upwind discretization is used for the convective term, while the diffusive terms are central-differenced with second-order accuracy. The sets of discretized equations are solved in the high-performance software package Ansys Fluent [55] with CHEMKIN CFD solver. The first order upwind scheme method with Semi-Implicit Method for Pressure Linked Equations (SIMPLE) algorithm [39] has been utilized to achieve a steady state solution. The computational domain is meshed using a non-uniform distribution of structured quadrilateral elements, having higher mesh density at and along the no-slip boundary and reaction zone to resolve the velocity, thermal boundary layer and species transport correctly. A total number of 13,500 quadrilateral elements were used with a maximum and minimum grid size of 0.5 mm and 0.1 mm respectively. The mesh sizes used for the analyses are chosen as such to ensure grid independent solutions.

5.6 Results and Discussion

Numerically obtained results for multi-step methanol hydrothermal combustion has been first validated against the experimental measurement [196] and then compared with that found utilizing global reaction mechanism. The centerline temperature distribution has been plotted in Fig. 5.4. Simulations with the single step oxidation chemistry (CH_3OH + 1.5 O_2 = CO_2 + 2 H_2O) of Narayanan are found to overpredict the flame temperature by ~25%. And 28% respectively for low (X_{MeOH} = 0.071) and high (X_{MeOH} = 0.097) fuel loading studied. For both cases, the predictions from the multi-step kinetic scheme are

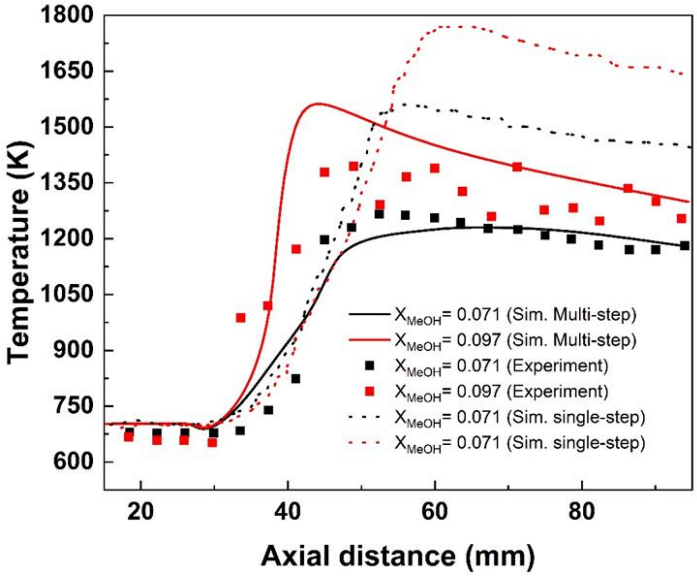

Figure 5.4: Comparison of centerline temperature distribution between simulation with single and multi-step chemistry along with the experimental results

found to be in significantly better agreement with the experiment exhibiting a maximum of 6% and 9% respectively. Besides, multi-step chemistry performs better in locating the flame position (i.e., the peak temperature location). The spatial location of the onset of the reaction zone tends to shift upstream as fuel mole fraction is increased which was also observed in the experiment, but a single step chemistry failed to predict.

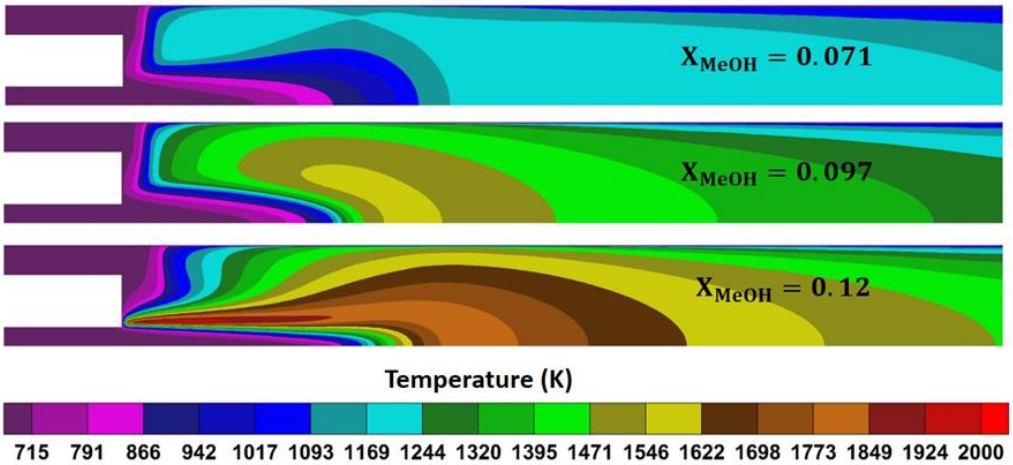

Figure 5.5: Steady-state contour plots of temperature for the different fuel loading

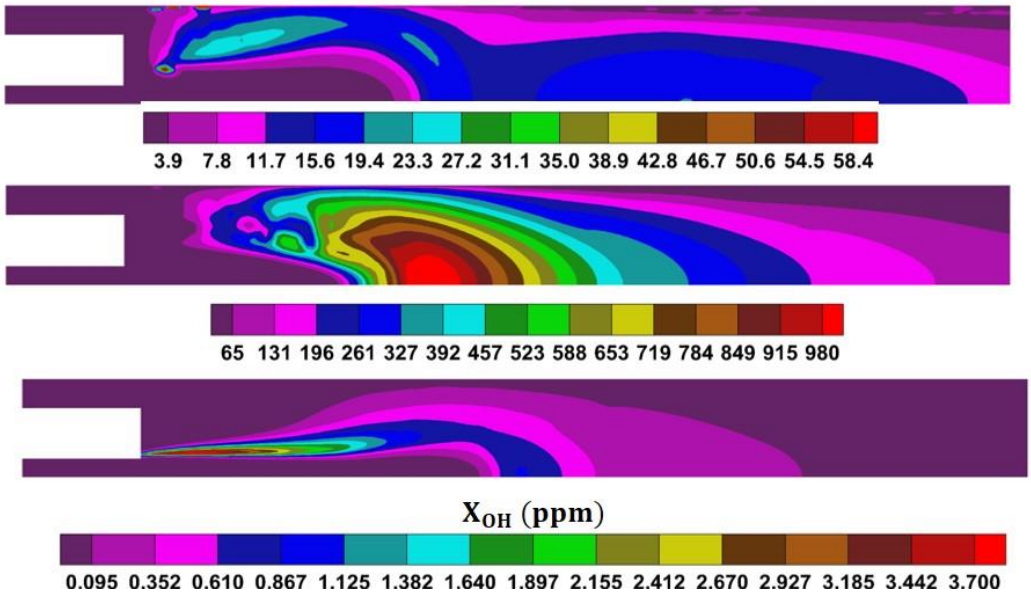

Figure 5.6: Contour plots of OH mole fraction for the different fuel loading

Simulations have been conducted for different fuel loading conditions to elucidate ignition mapping and flame structures. The flame structure and position can be determined by the temperature and the OH mole fraction contour presented in Fig. 5.5 and 5.6, respectively. At the highest fuel loading, the flame structure resembles a classic non-premixed jet flame, with the highest temperature region forming at the outer periphery of the jet, where the fuel and oxidizer mix to form a combustible mixture. Extremely sharp gradients in the flame structure are apparent in the temperature and OH distribution. A close comparison of the temperature and OH contour indicates that the flame structure has a lower radial and axial gradient under the leanest condition. We would highlight that from the simulation results of $X_{MeOH} = 0.071$, it is difficult to conclude if a flame exists or if the temperature increase is due to some partial oxidation processes. The OH concentration is found to be extremely low and ranging to a few ppm levels (Fig. 5.6). The lowest fuel loading of $X_{MeOH} = 0.025$ was also simulated to identify the combustion limit. Under this

extreme lean condition, the simulations indicated that no hydrothermal flame was performed. A maximum temperature of 760K, which is only 60K higher than the wall temperature, was observed. With such a low increase in temperature, it is unlikely that significant oxidation reactions were taking place.

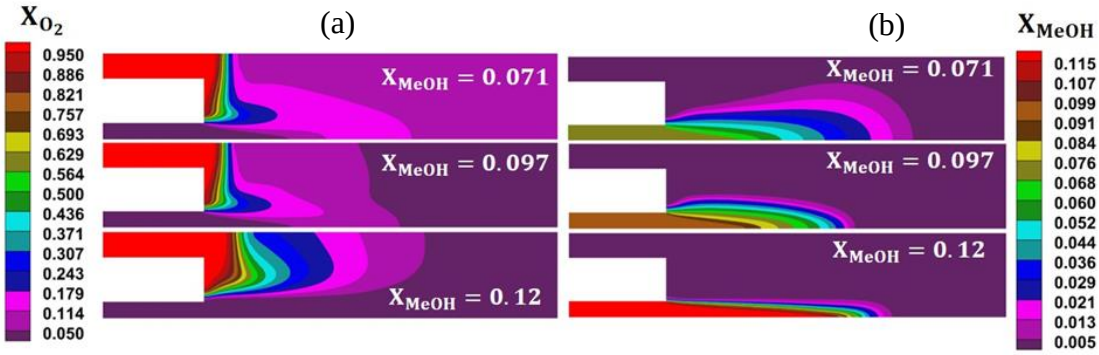

Figure 5.7: Mole fraction distribution of (a) oxygen and (b) methanol for different fuel loading (the Fig. is magnified over the high gradient zone for clarity purposes)

To further analyze the effect of fuel loading on flame formation, the mole fraction distribution of oxygen and methanol has been depicted in Fig. 5.7. With the increase of fuel loading, the penetration depth of the water-methanol stream increases (see Fig. 5.7b). A large penetration depth results in higher entrainment from the peripheral zone. On the other hand, the lower penetration depth of the core jet at lower fuel loading allows the outer peripheral oxygen to transport inwards through convective and diffusive processes (Fig. 5.7a). The transported oxygen at the core undergoes further mixing with the core until it reaches a flammable mixture and forms a lifted flame. The lift height increases as the fuel load is reduced further. To better understand the influence of fuel loading in determining the penetration depth, the axial component of the velocity and streamlines have been plotted in Fig.5.8. In the case of the highest fuel loading in this study (X_{MeOH} = 0.12), an

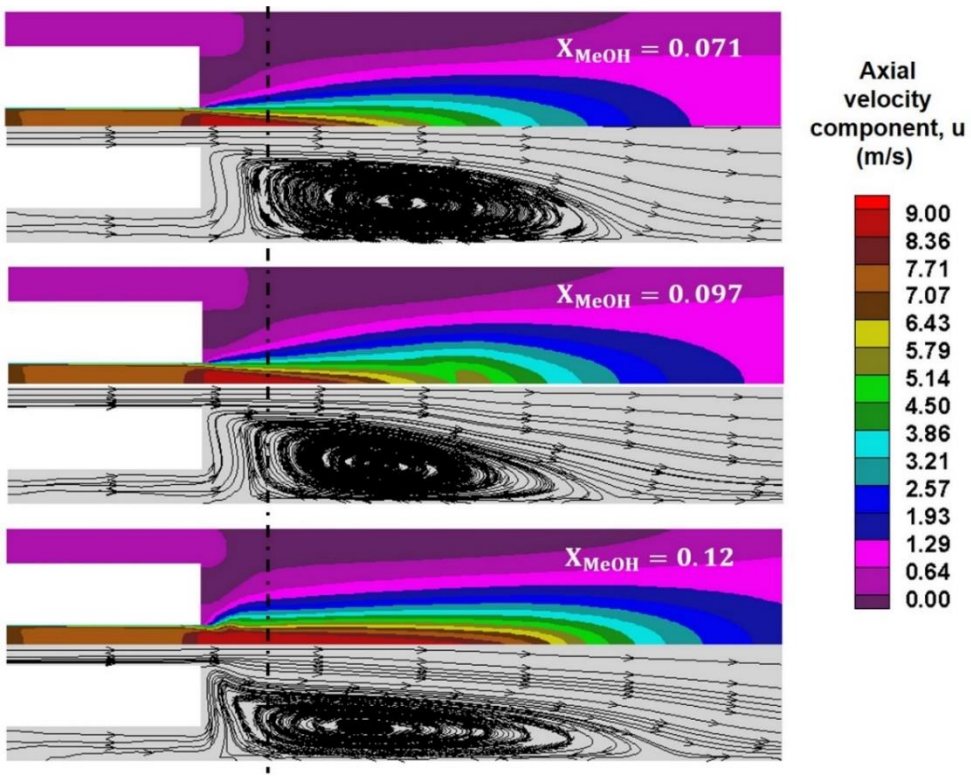

Figure 5.8: Contour plots of axial component of velocity and streamline for different fuel loading (Figure is magnified over the high gradient zone for clarity purpose). Dotted-dashed black line will be used as a reference axial location (x = 15 mm) to analyze radial distribution.

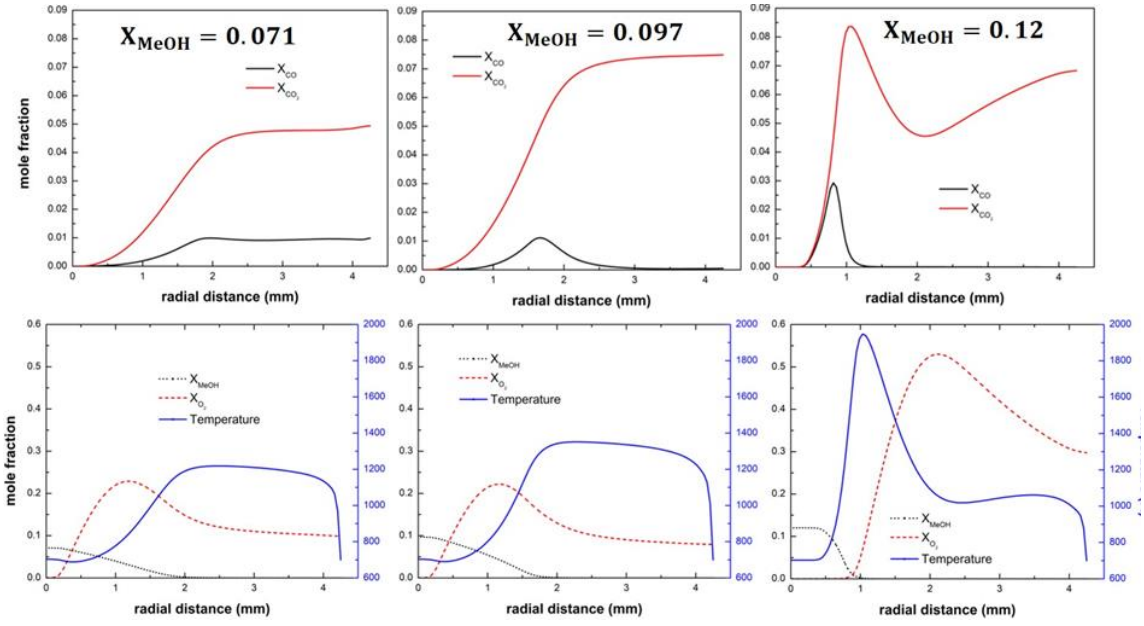

Fig. 5.9: Radial distribution of temperature and mole fraction of the species at the axial location x = 15 mm (dotted-dashed black line, Fig. 5.8)

elongated recirculation zone is observed. Hence, with high oxygen entrainment towards the core, a combustible mixture is formed at the outer periphery of the jet.

Figure 5.9 depicts the radial distribution of temperature and mole fraction of MeOH, O_2, CO_2, and CO at the axial location marked in Fig. 5.8 (dashed black line) for the different fuel loading conditions. For the highest fuel loading (X_{MeOH} = 0.12), a localized peak temperature zone is evident at r ≈ 1 mm, where fuel and oxidizer are consumed, forming a classic non-premixed thin flame structure with a peak temperature of ~2000 K. On the contrary, with the decreased fuel loading, the maximum flame temperature is decreased due to the lower global equivalence ratio, and the high-temperature region is outspread towards the outer periphery of the reactor, forming a lifted diffusion flame. For the lowest fuel loading case (X_{MeOH} = 0.071), fuel diminishes at r ≈ 2 mm (almost double the value found for the richest case), but the oxidizer is not fully consumed and further diffused to the outer periphery (X_{O2} ≈ 0.1), which is an evidence of partial oxidation at this condition. This is further illustrated by inspecting the CO_2 and CO distribution. For the highest fuel loading case, the CO forms a thin existence along the radial location of maximum temperature and then is completely converted into CO_2 along the radial direction, confirming a complete oxidation. Whereas, for X_{MeOH} = 0.097, the peak of CO is flatter and stretched further in the radial direction due to partial combustion. Finally, for the leanest of the condition studied (X_{MeOH} = 0.071), CO is present all along the radial direction, and at the outer periphery of the reactor, it retains a mole fraction value of ~0.01 (10,000 PPM) which is of the same order of CO_2 (~0.05 or ~50,000 PPM). The unreacted oxygen along the same trail exhibits the incomplete oxidation at this condition.

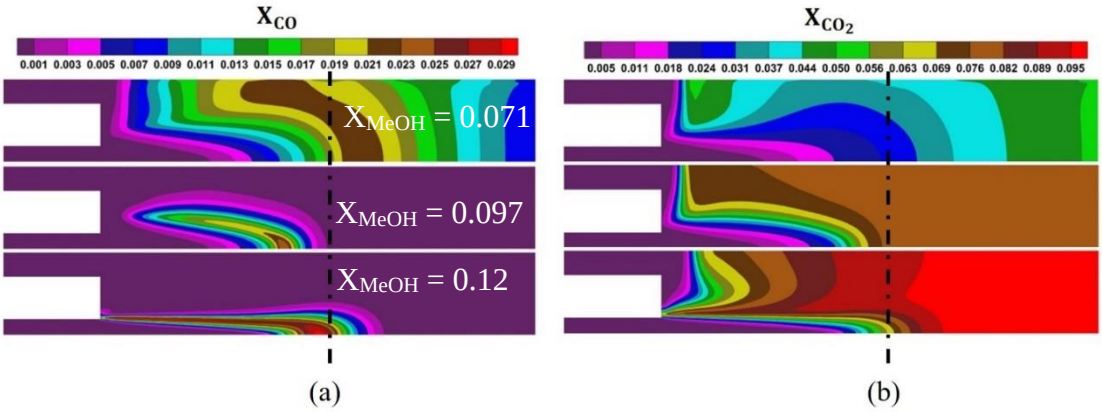

Figure 5.10: Mole fraction distribution of (a) CO and (b) CO_2 for different fuel loading. Dotted-dashed black line will be used as a reference axial location (x = 35 mm) to analyze radial distribution.

The CO and CO_2 mole fraction contours for the different fuel loading cases are presented in Fig. 5.10. At higher fuel loading, an intense oxidation process takes place and results in higher CO_2 concentration in the domain with a peak concentration of $X_{CO2} \approx 0.01$ (100,000 PPM). A thin zone of CO is present at the highest fuel loading, but the peak concentration (~0.04 or ~40,000 PPM) is lower by a factor of ~ 2.5. The peak CO is located at the fuel-rich zone of the jet. With a decrease in the fuel loading, the CO_2 concentration decreases significantly, however, a comparatively low decrease in CO is observed. For the lowest fuel loading, the CO concentration starts to become comparable with the CO_2 concentration (Fig. 5.11). This suggests the possibility of partial oxidation/incomplete combustion in the leanest condition. By comparing the temperature and CO profiles, it can be seen that the predicted CO profiles coincide with the flame lift height.

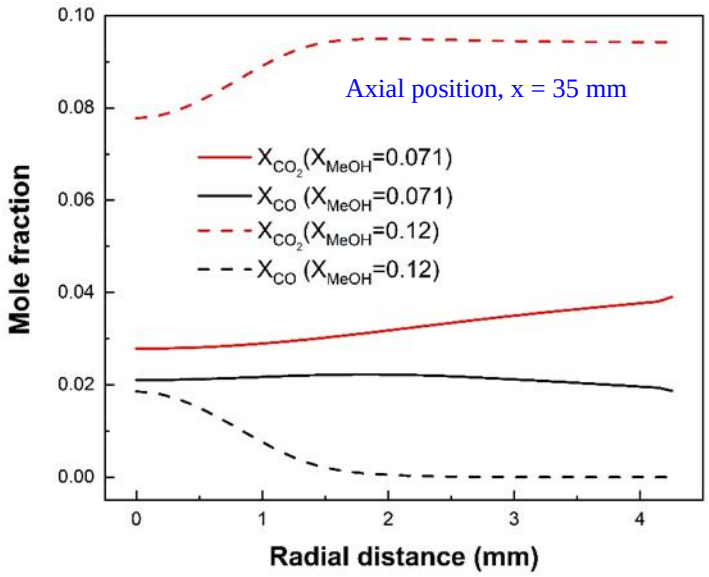

Figure 5.11: Radial distribution of mole fraction of the CO_2 and CO at axial location x = 35 mm (dotted-dashed black line, Fig. 5.10)

The radial distribution of the rate of production of CO and CO_2 is presented in Fig. 5.12 for two fuel loading cases (X_{MeOH} = 0.12 and X_{MeOH} = 0.071) at x = 15 mm and x = 35 mm. At x =15 mm (Fig. 5.12a), the net reaction rate for X_{MeOH} = 0.12 is significantly higher than that of X_{MeOH} = 0.071. The peak rates of CO and CO_2 production for X_{MeOH} = 0.12 are ~ 4.5×10^{-4} and ~ 4×10^{-4} mol/cm^{3}s, respectively, and they coincide with the peak oxygen concentration location (r ~ 1 mm), as shown in Figure 5.9 (bottom right). In contrast, for X_{MeOH} = 0.071, the peak production rates of CO and CO_2 are reduced by approximately 96% and 99%, respectively indicating lower chemical conversion at lower fuel loading. Moreover, in this case, the rate of CO production (~ 1.65×10^{-5} mol/cm^{3}s) is approximately 4.5 times higher than that of the CO_2 (~ 3.75×10^{-6} mol/cm^{3}s) indicating a lack of CO to CO_2 conversion.

(a)

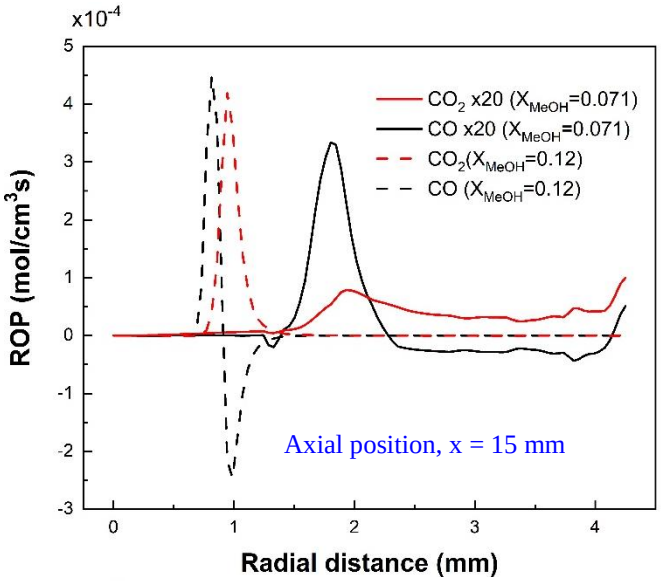

(b)

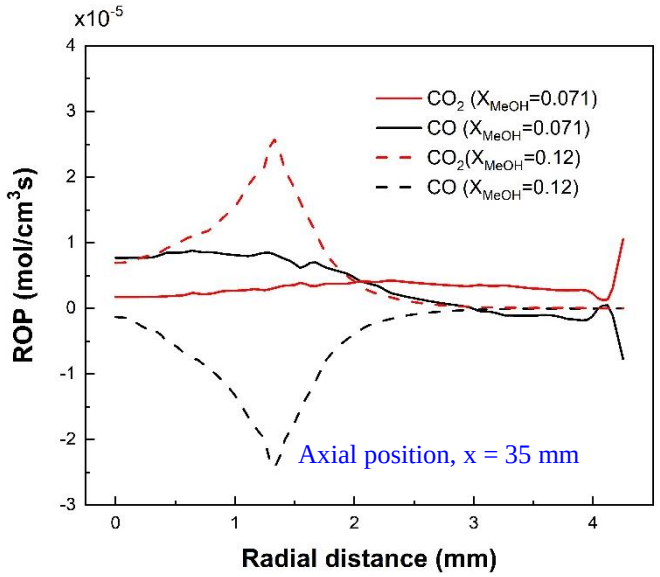

Figure 5.12: Rate of production (ROP) of CO and CO_2 along radial distance for X_{MeOH} = 0.071 and X_{MeOH} = 0.12 at two axial locations, (a) x = 15 mm, (b) x = 35 mm.

At an axial location of x = 35 mm, the net reaction rates of both fuel loading cases decrease significantly (in order of magnitude) as much of the fuel has already been consumed. In the case of X_{MeOH} = 0.12, the rate of CO_2 and CO production is opposite in sign, indicating an increase in CO to CO_2 conversion due to complete fuel consumption

(a)

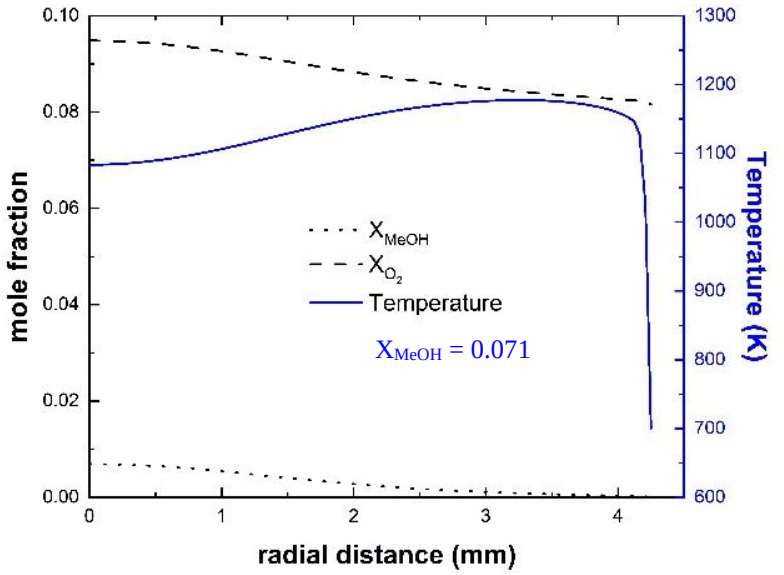

(b)

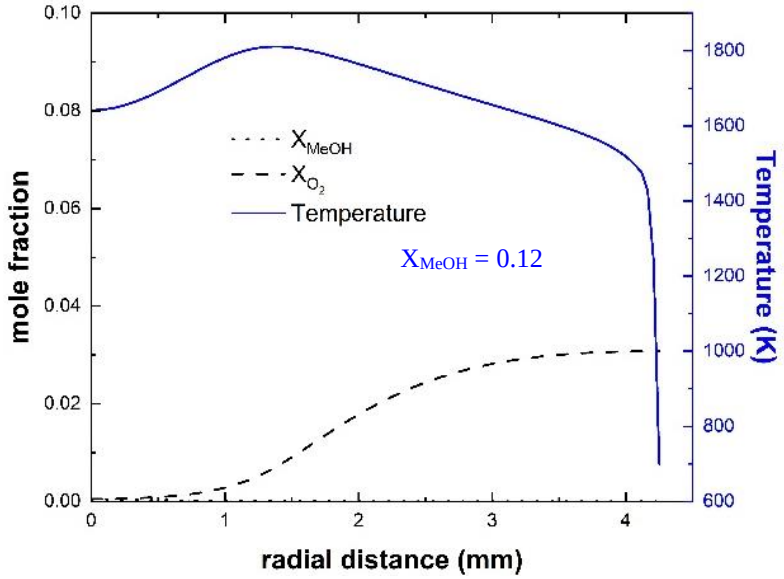

Figure 5.13: Radial distribution of temperature and mole fraction of O_2 and MeOH at the axial location x = 35 mm (dotted-dashed black line, Fig. 5.10).

and availability of sufficient O_2 (Fig. 5.13b). However, for X_{MeOH} = 0.071, the production rates of CO and CO_2 seem to be in competition with each other throughout the radial direction due to the presence of unreacted MeOH and O_2 (Fig. 5.13a). Although these unreacted components continue to react radially, CO to CO_2 conversion is unfavorable under this condition. To confirm this, the kinetic reaction rates of rxn# 29 ($CO + O_2 = CO_2$

(a)

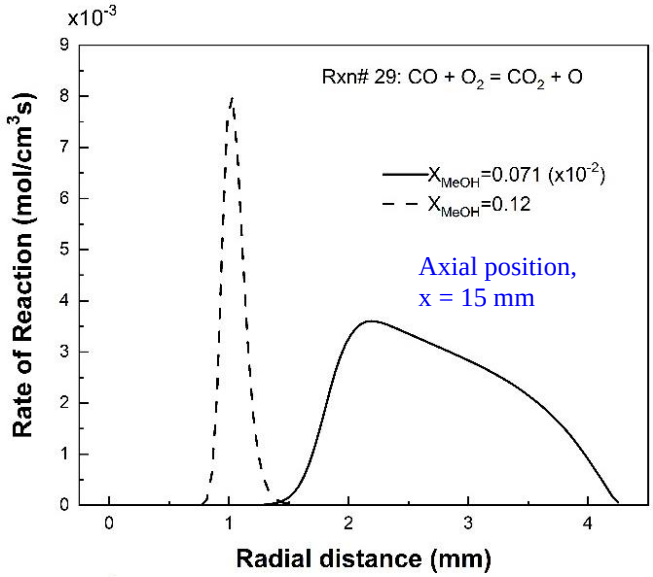

(b)

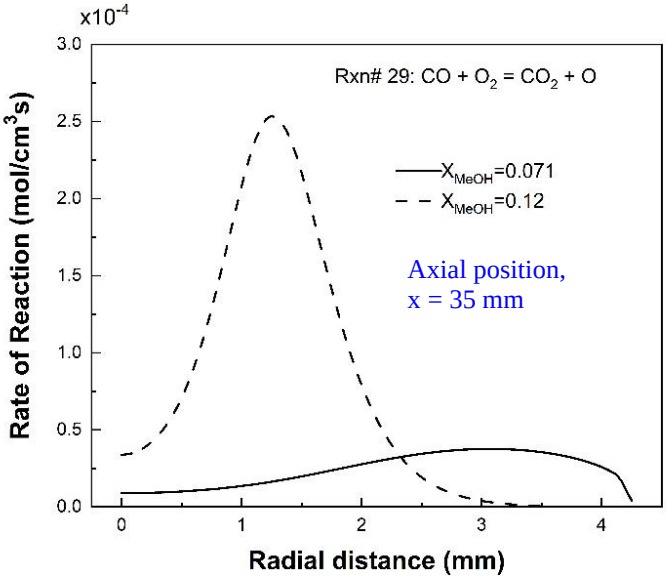

Figure 5.14: Rate of reaction of CO to CO_2 conversion as a function of radial distance at two different axial locations, (a) x = 15 mm, (b) x = 35 mm.

+ O) are plotted in Fig. 5.14. At the axial location x = 15 mm, the higher fuel loading condition shows a peak reaction rate more than two orders of magnitude greater than that of the lower fuel loading condition (Fig. 5.14a). At x = 35 mm, the peak reaction rate for X_{MeOH} = 0.12 is ~ 2.5 10^{-4} mol/cm^3s and has a bell curve structure, with maximum conversion occurring at r = 1 mm, followed by convective removal of the produced CO_2

(see Fig. 5.11, red-dashed line). In contrast, for X_{MeOH} = 0.071, the reaction rate remains low with a small variation in the radial direction, leading to comparable concentration values of CO and CO_2 that remain flat (red and black continuous line Fig. 5.11).

In this section, kinetic parameters associated with the multi-step chemistry employed in this study have been assessed. In addition, perturbation analysis was conducted to identify the impact of third-body collision efficiency of keys species on the overall predictions. In this parametric study, each case represents an increase/decrease of third body efficiency of water by a factor of two, respectively, for a reaction, whereas the kinetic parameters of the rest of the reactions were unaltered. We were particularly interested in the lowest fuel loading cases studied (X_{MeOH} = 0.071) since it exhibits incomplete oxidation with an OH concentration in the order of ~1 PPM. This will provide valuable insights into the flammability limit based on fuel loading and its dependence on the chemical kinetic parameters.

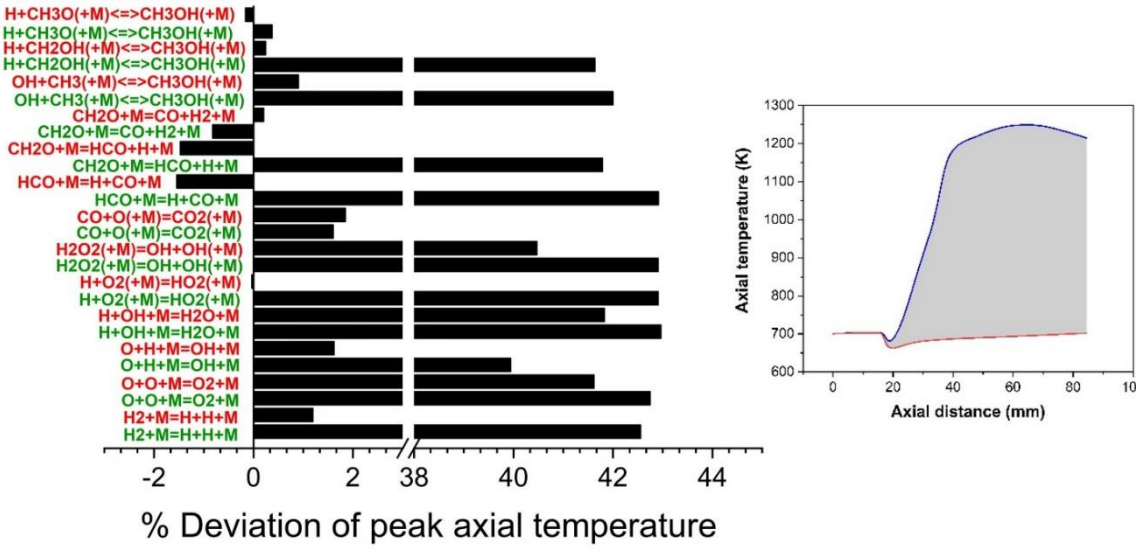

Figure 5.15 Percentage of the deviation of peak axial temperature attained by perturbing third body efficiency of water compared to unperturbed case (reactions in the green and red text represent 100 % increase and 50% decrease of third body efficiency respectively). The inset graph showing the spread of axial temperature distribution of the simulated cases

The deviation of peak axial temperature of the perturbed cases compared to that of the base (unperturbed) case has been depicted in Fig. 5.15 (reactions in the green and red text represent a factor of two increase and decrease of third body efficiency, respectively). The predictions show that the ignition behavior and peak axial temperature are susceptible to the third body collision efficiency parameters – undergoing complete extinction or establishing a stable flame structure. While the third body efficiency of water was decreased by 50%, three of the thirteen simulated cases resulted in complete extinction showing maximum deviation of axial peak temperature (~40%) compared to the unperturbed case. On the contrary, the opposite trend has been observed when the third body efficiency was increased. However, chain terminating reactions $O+O+M=O_2+M$ and $H+OH+M=H_2O+M$ were found to be exhibiting the highest sensitivity to the perturbation of the third body efficiency. Regardless of the sign of the perturbation (100% increase and 50% decrease), these two conditions failed to ignite the mixture. Whereas the chain branching reaction $CH_2O+M=CO+H_2+M$ has been found to show smaller sensitivity to the kinetic perturbation and resulted in stable flame with ~1.5% and 0.5% deviation in peak axial temperature by increasing and decreasing third body efficiency respectively. The inset graph of Fig.5.15 depicts the spread of axial temperature distribution of the simulated cases. The span of the peak axial temperature from ~700K (unignited) to ~1260K (ignited) confirms the uncertainties rooted in the kinetic parameter values at supercritical condition.

Figure 5.16 presents the deviation of the location of peak axial temperature for the simulated cases. The chain branching reaction HCO+M=H+CO+M shows the highest sensitivity; an increase in third body efficiency fails to form an ignition, whereas a stable flame is formed by reducing the third body efficiency but with a deviation of ~11% of the

location of peak axial temperature compared to unperturbed solution. This effort indicates that the kinetic parameters of the reaction mechanics require further scrutiny to analyze their applicability and suitability in supercritical conditions.

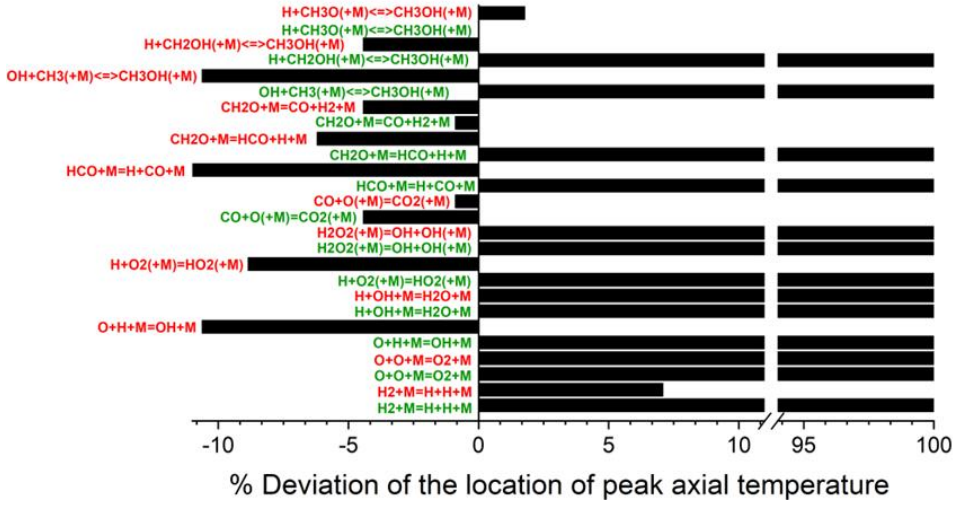

Figure 5.16 Percentage of the deviation of the location of peak axial temperature attained by perturbing third body efficiency of water compared to unperturbed case (reactions in the green and red text represents 100 % increase and 50% decrease of third body efficiency respectively).

5.7 Summary and Conclusion

This study developed a two-dimensional axisymmetric model to study hydrothermal flame produced through methanol oxidation at supercritical conditions. A detailed chemical kinetics scheme is employed in the simulations and compared with experimental results and predictions using a single-step chemistry model. Results from the simulations show that the detailed kinetics scheme can capture the experimental measurements both quantitatively and qualitatively. It was found that multi-step chemistry performs better than single-step chemistry in predicting temperature and flame location. Further simulations have been conducted by varying the fuel loading. A decrease in the fuel loading resulted in the formation of a lifted reaction front, with the lift height

increasing as the fuel loading decreased. The dynamic balance between convective and diffusive effects determines the structure of the flame, which is dictated by the incoming fuel loading.

The concentration and production rates of carbon monoxide (CO) and carbon dioxide (CO_2) under different fuel loading conditions are discussed. As the fuel loading increases, there is more oxidation entrainment near the core, leading to higher CO_2 production. At the highest fuel loading, there is a thin zone of CO, with a peak concentration of about 0.04 (40,000 PPM). The peak CO concentration is located at the fuel-rich zone of the jet. With a decrease in fuel loading, the CO_2 concentration decreases significantly, but there is a comparatively low decrease in CO. At the lowest fuel loading, the CO concentration becomes comparable with the CO_2 concentration, suggesting the possibility of partial oxidation/incomplete combustion in the leanest condition. The findings suggest that CO_2 and CO profiles coincide with the flame lift height.

The radial distribution of the rate of production of CO and CO_2 is presented for two fuel loading cases at axials locations of x = 15mm and x = 35mm. At x = 15mm, the net reaction rate for the higher fuel loading is significantly higher than that of the lower fuel loading. The peak rates of CO and CO_2 production are around 4.5×10^{-4} and 4×10^{-4} mol/cm^{3}s, respectively, and they coincide with the peak oxygen concentration location. In contrast, for the lower fuel loading, Moreover, in this case, the rate of CO production is approximately 4.5 times higher than that of CO_2, indicating a lack of CO to CO_2 conversion. At x = 35mm, as fuel is consumed, net reaction rates decrease for both higher and lower fuel loading cases. Higher fuel loading shows an increase in CO to CO_2 conversion due to complete fuel consumption and sufficient O_2 entrainment. On the other

hand, lower fuel loading results in CO and CO_2 production rates competing with each other radially, leading to an unfavorable CO to CO_2 conversion due to the presence of unreacted fuel and oxygen. The kinetic reaction rate of $CO + O_2 = CO_2 + O$ confirms this observation. The peak rate of this reaction is more than two orders of magnitude greater for the higher fuel loading condition compared to the lower fuel loading condition at x=15mm.

A parametric study has been conducted to assess the impact of the third-body collision efficiency parameters on the overall predictions. By perturbing the third body efficiency parameters, it has been found that the ignition behavior of the mixture, flame temperature and structure show distinctively different characteristics.

CHAPTER 6: CONCLUSION

6.1 SUMMARY AND MAJOR CONTRIBUTIONS

The existing knowledge gap regarding reduced-temperature flame modeling and the role of multidimensional transport was the intrinsic motivation to pursue this work. In Chapter 1, the critical need for multidimensional transport-coupled analysis of low-temperature flames was emphasized, and the two research cases (i.e., counterflow cool flame and hydrothermal flame) were introduced. Chapters 2 and 3 provided a comprehensive description of the mathematical and numerical framework used in this work. In Chapters 4 and 5, detailed case studies were presented and analyzed. Together, this work highlights the significance of multidimensional transport in understanding low-temperature flames and provides insights into the underlying physics and chemistry governing these complex processes.

In Chapter 4, the numerical analysis of non-premixed cool flame formation of dimethyl ether (DME) combustion in counterflow geometry was presented to understand the effect of multidimensional transport and its deviation from ideal conditions. It was found that the 2D-axisymmetric model prediction was in better agreement with experimental measurements compared to the quasi-1D model prediction. The study identified the Richardson number as a critical parameter for characterizing the system, with cool flames requiring much lower strain rates to sustain. At lower strain rates (a = 60~150), the Richardson number is relatively high (0.1~1.5); and the buoyancy effect is significant. This highlights the importance of considering the relative importance of buoyancy and flow

inertia in determining the flame location in low-temperature combustion in counterflow geometries. The deviation of ideal plug flow assumption in counterflow geometries has been analyzed. The 2D axisymmetric model resolves this perturbation without imposing any radial velocity gradient at the nozzle exits. The deviation originates from the axial velocity gradient at the nozzle exits as the global strain rate increases, which cannot be modeled by the 1D assumption. By incorporating multidimensional transport, the effectiveness of the 2D model in simulating cool flame formation in counterflow geometry in a self-consistent manner was demonstrated. Additionally, the model was extended to study cool flame extinction at high-pressure conditions, revealing two distinct trends in extinction strain rates for different fuel loadings at 3 and 5 atm pressures.

In the second study of the dissertation (Chapter 5), a hydrothermal flame of methanol combustion in a supercritical water medium was simulated using a detailed chemical kinetics scheme. Results from the simulations show that the detailed kinetics scheme can capture the experimental measurements reasonably well both quantitatively and qualitatively in comparison with using a single-step chemistry. Simulations were conducted by varying the fuel loading, and it was found that at the highest fuel loading, the flame structure resembled a classic non-premixed jet flame, with the highest temperature region forming at the outer periphery of the jet, where the fuel and oxidizer mix to form a combustible mixture. The temperature and OH distribution exhibit extremely sharp gradients in the flame structure. However, as the fuel loading is decreased, the flame structure changes and a lifted reaction front is formed, with the lift height increasing as the fuel loading is decreased. The structure of the flame is dictated by the dynamic balance between convective and diffusive effects, which is determined by the incoming fuel

loading. It is worth noting that at a specific fuel loading (X_{MeOH} = 0.071), it was difficult to conclude whether a flame exists or if the temperature increase is due to some partial oxidation processes, as the OH concentration was found to be extremely low, ranging to a few ppm levels. Similarly, under the lowest fuel loading condition of X_{MeOH} = 0.025, the simulations indicated that no hydrothermal flame was present, as the maximum temperature observed was only 60K higher than the wall temperature, suggesting that significant oxidation reactions were unlikely to be taking place. As the fuel loading increases, there is more oxidation entrainment near the core, leading to higher CO_2 production. With a decrease in fuel loading, the CO_2 concentration decreases significantly, but there is a comparatively low decrease in CO. At the lowest fuel loading, the CO concentration becomes comparable with the CO_2 concentration, suggesting the possibility of partial oxidation/incomplete combustion in the leanest condition. Overall, the findings from the study suggest that the CO_2 and CO profiles coincide with the flame lift height, further confirming the importance of considering multidimensional transport in the formation and dynamics of hydrothermal flames.

In summary, the dissertation has contributed significant insights into the behavior and structure of low-temperature flames in counterflow and hydrothermal combustion. The results can serve as a basis for further research in the field of reacting flow simulations that involve multidimensional transport. The study has also advanced the current knowledge and understanding of non-premixed flames and can be expected to inspire further research in this area.

6.2 FUTURE RECOMMENDATIONS

This dissertation has explored the multidimensional aspects of low-temperature flame formation in atmospheric and high-pressure conditions. To further improve the model and gain deeper insights, several studies can be conducted using the current framework.

Regarding the study of counterflow cool flame, there are a few notable areas of interest that could be explored:

1. Ignition characteristics and near-limit instability. In current work, the analyses were presented based on the steady-state solutions. The transient simulations were conducted until a steady-state solution is reached. It will be interesting to study the ignition/initiation and the near-limit instability of the flame.
2. Oscillatory cool flame. Recent studies have shown that the dynamical balance of heat generation from negative-temperature coefficient and hot ignition kinetics, as well as convective/diffusive heat loss to the far-field, can cause oscillatory observations in droplet combustion. A similar assessment could be done on the counterflow cool flame formation, either by providing a sinusoidal velocity boundary condition or by altering the fuel loading in a cyclic manner. The chemical, convective, and diffusive time scales could play a crucial role in simulating this phenomenon.

As for the hydrothermal flame, the following recommendations could be pursued as potential follow-up investigations:

1. Transient model development. The current work developed a steady-state numerical framework to simulate hydrothermal flame. To investigate the flame

ignition in supercritical water medium, the author recommends extending the model to a transient solver. This would provide further insights into supercritical water oxidation systems.

2. Waste stream analyses. Hydrothermal flame has potential applications in the treatment of hazardous materials in wastewater. Organic compounds exhibit complete solubility in supercritical water, and hydrothermal flame acts as an internal source of heat that oxidizes and converts the organic waste into inorganic precipitation out of the solution. This could be a topic of investigation as a follow-up work for the current effort.

The recommendations above are based on the experiences gained through the course of this dissertation work. The author believes that each proposal could be a Ph.D. and/or M.S. level research topic worthy of future exploration.

REFERENCES

[1] K. Seshadri and F. A. Williams, "Laminar flow between parallel plates with injection of a reactant at high Reynolds number," *International Journal of Heat and Mass Transfer*, vol. 21, no. 2, pp. 251-253, 1978.

[2] T. J. Wojnar, "Outlook for Energy: A View to 2040," presented at the AIChE Annual Meeting, Pittsburg, PA, USA, 2018.

[3] B. E. Layton, "A Comparison of Energy Densities of Prevalent Energy Sources in Units of Joules Per Cubic Meter," *International Journal of Green Energy*, vol. 5, no. 6, pp. 438-455, 2008/12/04 2008, doi: 10.1080/15435070802498036.

[4] Global Direct Primary Energy Consumption [Online] Available: https://ourworldindata.org/grapher/global-primary-energy?time=1970..latest

[5] M. Yao, Z. Zheng, and H. Liu, "Progress and recent trends in homogeneous charge compression ignition (HCCI) engines," *Progress in Energy and Combustion Science*, vol. 35, no. 5, pp. 398-437, 2009/10/01/ 2009, doi: https://doi.org/10.1016/j.pecs.2009.05.001.

[6] F. Zhao, T. N. Asmus, D. N. Assanis, J. E. Dec, J. A. Eng, and P. M. Najt, "Homogeneous charge compression ignition (HCCI) engines," 2003.

[7] Sources of Greenhouse Gas Emissions [Online] Available: https://www.epa.gov/ghgemissions/sources-greenhouse-gas-emissions

[8] S. Bobi, M. Kashif, and Y. Laoonual, "Combustion and emission control strategies for partially-premixed charge compression ignition engines: A review," *Fuel*, vol. 310, p. 122272, 2022.

[9] S. L. Kokjohn, R. M. Hanson, D. Splitter, and R. Reitz, "Fuel reactivity controlled compression ignition (RCCI): a pathway to controlled high-efficiency clean combustion," *International Journal of Engine Research*, vol. 12, no. 3, pp. 209-226, 2011.

[10] R. D. Reitz and G. Duraisamy, "Review of high efficiency and clean reactivity controlled compression ignition (RCCI) combustion in internal combustion engines," *Progress in Energy and Combustion Science*, vol. 46, pp. 12-71, 2015.

[11] M. Mofijur, M. M. Hasan, T. M. I. Mahlia, S. M. A. Rahman, A. S. Silitonga, and H. C. Ong, "Performance and Emission Parameters of Homogeneous Charge Compression Ignition (HCCI) Engine: A Review," *Energies*, vol. 12, no. 18, p. 3557, 2019. [Online]. Available: https://www.mdpi.com/1996-1073/12/18/3557.

[12] D. S. Kim and C. S. Lee, "Improved emission characteristics of HCCI engine by various premixed fuels and cooled EGR," *Fuel*, vol. 85, no. 5, pp. 695-704, 2006/03/01/ 2006, doi: https://doi.org/10.1016/j.fuel.2005.08.041.

[13] G. Samuels, A. Rose, G. David, and J. Hooker, "Energy Conservation in Transportation," in *Advances in Energy Systems and Technology*, P. Auer Ed.: Academic Press, 1982, pp. 187-297.

[14] K. Sudheesh and J. M. Mallikarjuna, "Diethyl ether as an ignition improver for biogas homogeneous charge compression ignition (HCCI) operation - An

experimental investigation," *Energy*, vol. 35, no. 9, pp. 3614-3622, 2010/09/01/ 2010, doi: https://doi.org/10.1016/j.energy.2010.04.052.

[15] D. Davidson, B. Gauthier, and R. Hanson, "Shock tube ignition measurements of iso-octane/air and toluene/air at high pressures," *Proceedings of the Combustion Institute*, vol. 30, no. 1, pp. 1175-1182, 2005.

[16] G. Mittal and C.-J. Sung, "A rapid compression machine for chemical kinetics studies at elevated pressures and temperatures," *Combustion Science and Technology*, vol. 179, no. 3, pp. 497-530, 2007/03/01 2007, doi: 10.1080/00102200600671898.

[17] P. Dagaut, M. Reuillon, and M. Cathonnet, "Experimental study of the oxidation of n-heptane in a jet stirred reactor from low to high temperature and pressures up to 40 atm," *Combustion and Flame*, vol. 101, no. 1-2, pp. 132-140, 1995.

[18] M. D. Smooke, "Solution of burner-stabilized premixed laminar flames by boundary value methods," *Journal of Computational Physics*, vol. 48, no. 1, pp. 72-105, 1982.

[19] S. H. Won, B. Jiang, P. Diévart, C. H. Sohn, and Y. Ju, "Self-sustaining n-heptane cool diffusion flames activated by ozone," *Proceedings of the Combustion Institute*, vol. 35, no. 1, pp. 881-888, 2015.

[20] H. J. Curran, P. Gaffuri, W. J. Pitz, and C. K. Westbrook, "A comprehensive modeling study of iso-octane oxidation," *Combustion and flame*, vol. 129, no. 3, pp. 253-280, 2002.

[21] H. J. Curran, P. Gaffuri, W. J. Pitz, and C. K. Westbrook, "A comprehensive modeling study of n-heptane oxidation," *Combustion and flame,* vol. 114, no. 1-2, pp. 149-177, 1998.

[22] G. Mittal, M. P. Raju, and C.-J. Sung, "CFD modeling of two-stage ignition in a rapid compression machine: Assessment of zero-dimensional approach," *Combustion and Flame,* vol. 157, no. 7, pp. 1316-1324, 2010.

[23] F. L. Dryer and M. Chaos, "Ignition of syngas/air and hydrogen/air mixtures at low temperatures and high pressures: Experimental data interpretation and kinetic modeling implications," *Combustion and Flame,* vol. 152, no. 1-2, pp. 293-299, 2008.

[24] C. B. Reuter, S. H. Won, and Y. Ju, "Flame structure and ignition limit of partially premixed cool flames in a counterflow burner," *Proceedings of the Combustion Institute,* vol. 36, no. 1, pp. 1513-1522, 2017/01/01/ 2017, doi: https://doi.org/10.1016/j.proci.2016.06.067.

[25] C. B. Reuter, R. Zhang, O. R. Yehia, Y. Rezgui, and Y. Ju, "Counterflow flame experiments and chemical kinetic modeling of dimethyl ether/methane mixtures," *Combustion and Flame,* vol. 196, pp. 1-10, 2018/10/01/ 2018, doi: https://doi.org/10.1016/j.combustflame.2018.06.004.

[26] S. C. Chapra and R. P. Canale, *Numerical methods for engineers*. Mcgraw-hill New York, 2011.

[27] S. Chapman and T. G. Cowling, *The mathematical theory of non-uniform gases. an account of the kinetic theory of viscosity, thermal conduction and diffusion in gases*. 1970.

[28] Y. Tominaga and T. Stathopoulos, "Turbulent Schmidt numbers for CFD analysis with various types of flowfield," *Atmospheric Environment*, vol. 41, no. 37, pp. 8091-8099, 2007/12/01/ 2007, doi: https://doi.org/10.1016/j.atmosenv.2007.06.054.

[29] B. E. Launder and D. B. Spalding, *Mathematical Models of turbulence*. Academic Press.

[30] P. Atkins, P. W. Atkins, and J. de Paula, *Atkins' physical chemistry*. Oxford university press, 2014.

[31] C. Zheng, D. M. Coombs, and B. Akih-Kumgeh, "Real Gas Model Parameters for High-Density Combustion from Chemical Kinetic Model Data," *ACS Omega*, vol. 4, no. 2, pp. 3074-3082, 2019/02/28 2019, doi: 10.1021/acsomega.8b03150.

[32] G.-S. Zhu and R. D. Reitz, "A model for high-pressure vaporization of droplets of complex liquid mixtures using continuous thermodynamics," *International Journal of Heat and Mass Transfer*, vol. 45, no. 3, pp. 495-507, 2002/01/01/ 2002, doi: https://doi.org/10.1016/S0017-9310(01)00173-9.

[33] D.-Y. Peng and D. B. Robinson, "A New Two-Constant Equation of State," *Industrial & Engineering Chemistry Fundamentals*, vol. 15, no. 1, pp. 59-64, 1976/02/01 1976, doi: 10.1021/i160057a011.

[34] L. Matuszewski and F. Dupoirieux, "Detailed modeling of planar transcritical H2–O2–N2 flames AU - Giovangigli, Vincent," *Combustion Theory and Modelling*, vol. 15, no. 2, pp. 141-182, 2011/03/17 2011, doi: 10.1080/13647830.2010.527016.

[35] L. S. Tee, S. Gotoh, and W. E. Stewart, "Molecular Parameters for Normal Fluids. Lennard-Jones 12-6 Potential," *Industrial & Engineering Chemistry Fundamentals*, vol. 5, no. 3, pp. 356-363, 1966/08/01 1966, doi: 10.1021/i160019a011.

[36] C. Zheng, Akih-Kumgeh, B., "Accounting for real-gas effects in high-density combustion chamber," in *Spring Technical Meeting of the Eastern States Section of the Combustion Institute, ESSCI 2018*, State College, United States, 2018.

[37] R. C. Reid and T. W. Leland Jr, "Pseudocritical constants," *AIChE Journal*, vol. 11, no. 2, pp. 228-237, 1965/03/01 1965, doi: 10.1002/aic.690110212.

[38] J. P. BE Poling, JP O'connell *The properties of gases and liquids*. McGraw-Hill 2001.

[39] S. Patankar, *Numerical heat transfer and fluid flow*. Taylor & Francis Group, 1980.

[40] H. K. Versteeg and W. Malalasekera, "Computational fluid dynamics," *The finite volume method*, pp. 1-26, 1995.

[41] J. H. Ferziger, M. Perić, and R. L. Street, *Computational methods for fluid dynamics*. Springer, 2002.

[42] V. J. Katz, "The History of Stokes' Theorem," *Mathematics Magazine*, vol. 52, no. 3, pp. 146-156, 1979/05/01 1979, doi: 10.1080/0025570X.1979.11976770.

[43] R. J. Kee and H. A. Dwyer, "Review of stiffness and implicit finite difference methods in combustion modeling," Sandia National Labs., Livermore, CA (USA); California Univ., Davis (USA …, 1980.

[44] F. Zhang, H. Bonart, T. Zirwes, P. Habisreuther, H. Bockhorn, and N. Zarzalis, "Direct Numerical Simulation of Chemically Reacting Flows with the Public Domain Code OpenFOAM," in *High Performance Computing in Science and*

Engineering '14, Cham, W. E. Nagel, D. H. Kröner, and M. M. Resch, Eds., 2015// 2015: Springer International Publishing, pp. 221-236.

[45] C. A. De Moura and C. S. Kubrusly, "The courant–friedrichs–lewy (cfl) condition," *AMC*, vol. 10, no. 12, 2013.

[46] S. Descombes, M. Duarte, and M. Massot, "Operator splitting methods with error estimator and adaptive time-stepping. Application to the simulation of combustion phenomena," in *Splitting Methods in Communication, Imaging, Science, and Engineering*: Springer, 2016, pp. 627-641.

[47] I. S. Wichman, "On the use of operator-splitting methods for the equations of combustion," *Combustion and flame*, vol. 83, no. 3-4, pp. 240-252, 1991.

[48] A. C. Hindmarsh *et al.*, "SUNDIALS: Suite of nonlinear and differential/algebraic equation solvers," *ACM Transactions on Mathematical Software (TOMS)*, vol. 31, no. 3, pp. 363-396, 2005.

[49] R. Serban and A. C. Hindmarsh, "CVODES: An ODE solver with sensitivity analysis capabilities," Technical Report UCRL-JP-200039, Lawrence Livermore National Laboratory, 2003.

[50] A. Cuoci, A. Frassoldati, T. Faravelli, and E. Ranzi, "Numerical modeling of laminar flames with detailed kinetics based on the operator-splitting method," *Energy & fuels*, vol. 27, no. 12, pp. 7730-7753, 2013.

[51] A. C. Aghdam, "Fundamental understanding of plasma discharge formation in liquid and multiphase configurations through multiphysics modeling," 2020.

[52] T. Zirwes *et al.*, "Quasi-DNS Dataset of a Piloted Flame with Inhomogeneous Inlet Conditions," *Flow, Turbulence and Combustion,* vol. 104, no. 4, pp. 997-1027, 2020/04/01 2020, doi: 10.1007/s10494-019-00081-5.

[53] H. Jasak, A. Jemcov, and Tukovic, "OpenFOAM: A C++ Library for Complex Physics Simulations," 2007.

[54] D. G. Goodwin, H. K. Moffat, and R. L. Speth, "Cantera: An object-oriented software toolkit for chemical kinetics, thermodynamics, and transport processes," *Caltech, Pasadena, CA,* vol. 124, 2009.

[55] ANSYS. "ANSYS FLUENT Software Package 19.2." (accessed.

[56] R. J. Kee, F. M. Rupley, and J. A. Miller, "Chemkin-II: A Fortran chemical kinetics package for the analysis of gas-phase chemical kinetics," Sandia National Lab.(SNL-CA), Livermore, CA (United States), 1989.

[57] "ANSYS FLUENT Theory Guide 12.0," in *Theory Guide*, ed, 2009.

[58] R. I. Issa, "Solution of the implicitly discretised fluid flow equations by operator-splitting," *Journal of computational physics,* vol. 62, no. 1, pp. 40-65, 1986.

[59] R. I. Issa, A. D. Gosman, and A. P. Watkins, "The computation of compressible and incompressible recirculating flows by a non-iterative implicit scheme," *Journal of Computational Physics,* vol. 62, no. 1, pp. 66-82, 1986.

[60] T. Holzmann, "Mathematics, numerics, derivations and OpenFOAM®," *Loeben, Germany: Holzmann CFD,* 2016.

[61] Y. Ju, "Understanding cool flames and warm flames," *Proc. Combust. Inst.,* vol. 38, no. 1, pp. 83-119, 2021, doi: 10.1016/j.proci.2020.09.019.

[62] J. Dec, "Advanced compression-igntion engines - understanding the in-cylinder processes," *Proceedings of the Combustion Institute,* vol. 32, no. 2, pp. 2727- 2742, 2009.

[63] R. Reitz and D. Ganesh, "Review of high efficiency and clean reactivity controlled compression ignition (RCCI) combustion in internal combustion engines," *Progress in Energy and Combustion Science,* vol. 46, pp. 12 - 51, 2015.

[64] M.B. Colket *et al.*, "An Overview of the National Jet Fuels Combustion Program," presented at the 54th AIAA Aerospace Sciences Meeting, American Institute of Aeronautics and Astronautics, San Diego, California, January 4 - 8, 2016.

[65] Y. Ju, C. B. Reuter, O. R. Yehia, T. I. Farouk, and S. H. Won, "Dynamics of cool flames," *Prog. Energy Combust. Sci.*, vol. 75, p. 100787, 2019, doi: 10.1016/j.pecs.2019.100787.

[66] C. B. Reuter, M. Lee, S. H. Won, and Y. Ju, "Study of the low-temperature reactivity of large n -alkanes through cool diffusion flame extinction," *Combust. Flame,* vol. 179, pp. 23-32, 2017, doi: 10.1016/j.combustflame.2017.01.028.

[67] O. R. Yehia, C. B. Reuter, and Y. Ju, "Low-temperature multistage warm diffusion flames," *Combustion and Flame,* vol. 195, pp. 63-74, 2018.

[68] C. K. Law and P. Zhao, "NTC-affected ignition in nonpremixed counterflow," *Combustion and Flame,* vol. 159, no. 3, pp. 1044-1054, 2012/03/01/ 2012, doi: https://doi.org/10.1016/j.combustflame.2011.10.012.

[69] I. K. Puri and K. Seshadri, "Extinction of diffusion flames burning diluted methane and diluted propane in diluted air," *Combustion and Flame,* vol. 65, no. 2, pp. 137-150, 1986/08/01/ 1986, doi: https://doi.org/10.1016/0010-2180(86)90015-5.

[70] I. K. Puri, K. Seshadri, M. D. Smooke, and D. E. Keyes, "A Comparison Between Numerical Calculations and Experimental Measurements of the Structure of a Counterflow Methane-Air Diffusion Flame," *Combustion Science and Technology*, vol. 56, no. 1-3, pp. 1-22, 1987/11/01 1987, doi: 10.1080/00102208708947079.

[71] M. D. Smooke, I. K. Puri, and K. Seshadri, "A comparison between numerical calculations and experimental measurements of the structure of a counterflow diffusion flame burning diluted methane in diluted air," *Symposium (International) on Combustion*, vol. 21, no. 1, pp. 1783-1792, 1988/01/01/ 1988, doi: https://doi.org/10.1016/S0082-0784(88)80412-0.

[72] R. F. Johnson, A. C. VanDine, G. L. Esposito, and H. K. Chelliah, "On the axisymmetric counterflow flame simulations: is there an optimal nozzle diameter and separation distance to apply quasi one-dimensional theory?," *Combustion Science and Technology*, vol. 187, no. 1-2, pp. 37-59, 2015.

[73] C. J. Sung, J. B. Liu, and C. K. Law, "Structural response of counterflow diffusion flames to strain rate variations," *Combustion and Flame*, vol. 102, no. 4, pp. 481-492, 1995/09/01/ 1995, doi: https://doi.org/10.1016/0010-2180(95)00041-4.

[74] H. Guo, G. J. Smallwood, F. Liu, Y. Ju, and Ö. L. Gülder, "The effect of hydrogen addition on flammability limit and NOx emission in ultra-lean counterflow CH4/air premixed flames," *Proceedings of the Combustion Institute*, vol. 30, no. 1, pp. 303-311, 2005/01/01/ 2005, doi: https://doi.org/10.1016/j.proci.2004.08.177.

[75] J. C. Rolon, D. Veynante, J. P. Martin, and F. Durst, "Counter jet stagnation flows," *Experiments in Fluids*, vol. 11, no. 5, pp. 313-324, 1991/09/01 1991, doi: 10.1007/BF00194863.

[76] H. K. Chelliah, C. K. Law, T. Ueda, M. D. Smooke, and F. A. Williams, "An experimental and theoretical investigation of the dilution, pressure and flow-field effects on the extinction condition of methane-air-nitrogen diffusion flames," *Symposium (International) on Combustion*, vol. 23, no. 1, pp. 503-511, 1991/01/01/ 1991, doi: https://doi.org/10.1016/S0082-0784(06)80297-3.

[77] B. G. Sarnacki, G. Esposito, R. H. Krauss, and H. K. Chelliah, "Extinction limits and associated uncertainties of nonpremixed counterflow flames of methane, ethylene, propylene and n-butane in air," *Combustion and Flame*, vol. 159, no. 3, pp. 1026-1043, 2012.

[78] M. Hajilou, M. Q. Brown, M. C. Brown, and E. Belmont, "Investigation of the structure and propagation speeds of n-heptane cool flames," *Combustion and Flame*, vol. 208, pp. 99-109, 2019/10/01/ 2019, doi: https://doi.org/10.1016/j.combustflame.2019.06.020.

[79] M. Hajilou, T. Ombrello, S. H. Won, and E. Belmont, "Experimental and numerical characterization of freely propagating ozone-activated dimethyl ether cool flames," *Combustion and Flame*, vol. 176, pp. 326-333, 2017/02/01/ 2017, doi: https://doi.org/10.1016/j.combustflame.2016.11.005.

[80] M. Zhou *et al.*, "The radical index and the effect of oxygen concentration on non-premixed cool flame extinction of large n-alkanes," *Combustion and Flame*, vol. 231, p. 111471, 2021/09/01/ 2021, doi: https://doi.org/10.1016/j.combustflame.2021.111471.

[81] H. Davy, "VIII. Some new experiments and observations on the combustion of gaseous mixtures, with an account of a method of preserving a continued light in

mixtures of inflammable gases and air without flame," *Philosophical Transactions of the Royal Society of London,* vol. 107, pp. 77-85, 1817/01/01 1817, doi: 10.1098/rstl.1817.0009.

[82] V. Nayagam, D. L. Dietrich, M. C. Hicks, and F. A. Williams, "Cool-flame extinction during n-alkane droplet combustion in microgravity," *Combustion and Flame*, vol. 162, no. 5, pp. 2140-2147, 2015.

[83] S. R. Turns, *Introduction to combustion*. McGraw-Hill Companies New York, NY, USA, 1996.

[84] I. Glassman, R. A. Yetter, and N. G. Glumac, *Combustion*. Academic press, 2014.

[85] J. Zádor, C. A. Taatjes, and R. X. Fernandes, "Kinetics of elementary reactions in low-temperature autoignition chemistry," *Progress in energy and combustion science*, vol. 37, no. 4, pp. 371-421, 2011.

[86] N. N. Semenov, "Some Problems in Chemical Kinetics and Reactivity" Princeton University Press," ed: Princeton, 1958.

[87] D. T. A. Townend, "Ignition Regions of Hydrocarbons," *Chemical Reviews*, vol. 21, no. 2, pp. 259-278, 1937.

[88] T. I. Farouk and F. L. Dryer, "Isolated n-heptane droplet combustion in microgravity: "Cool Flames" – Two-stage combustion," *Combustion and Flame*, vol. 161, no. 2, pp. 565-581, 2014/02/01/ 2014, doi: https://doi.org/10.1016/j.combustflame.2013.09.011.

[89] V. Nayagam, D. L. Dietrich, P. V. Ferkul, M. C. Hicks, and F. A. Williams, "Can cool flames support quasi-steady alkane droplet burning?," *Combustion and Flame*,

vol. 159, no. 12, pp. 3583-3588, 2012/12/01/ 2012, doi: https://doi.org/10.1016/j.combustflame.2012.07.012.

[90] V. R. Katta and W. M. Roquemore, "Formation of a cool diffusion flame and its characteristics," *Proceedings of the Combustion Institute,* vol. 36, no. 1, pp. 1369-1376, 2017/01/01/ 2017, doi: https://doi.org/10.1016/j.proci.2016.06.101.

[91] A. E. Potter and J. N. Butler, "A novel combustion measurement based on the extinguishment of diffusion flames," vol. 29, ed, 1959, pp. 54-56.

[92] T. P. Pandya and F. J. Weinberg, "The structure of flat, counter-flow diffusion flames," *Proceedings of the Royal Society of London. Series A. Mathematical and Physical Sciences,* vol. 279, no. 1379, pp. 544-561, 1964.

[93] H. Tsuji, "Counterflow diffusion flames," *Progress in energy and combustion science,* vol. 8, no. 2, pp. 93-119, 1982.

[94] R. V. Ravikrishna and A. B. Sahu, "Advances in understanding combustion phenomena using non-premixed and partially premixed counterflow flames: A review," *International Journal of Spray and Combustion Dynamics,* vol. 10, no. 1, pp. 38-71, 2018/03/01 2017, doi: 10.1177/1756827717738168.

[95] G. Dixon-Lewis *et al.*, "Calculation of the structure and extinction limit of a methane-air counterflow diffusion flame in the forward stagnation region of a porous cylinder," in *Symposium (International) on Combustion*, 1985 1985, vol. 20: Elsevier, 1 ed., pp. 1893-1904.

[96] R. J. Kee, J. A. Miller, G. H. Evans, and G. Dixon-Lewis, "A computational model of the structure and extinction of strained, opposed flow, premixed methane-air

flames," in *Symposium (International) on Combustion*, 1989 1989, vol. 22: Elsevier, 1 ed., pp. 1479-1494.

[97] H. K. Chelliah, C. K. Law, T. Ueda, M. D. Smooke, and F. A. Williams, "An experimental and theoretical investigation of the dilution, pressure and flow-field effects on the extinction condition of methane-air-nitrogen diffusion flames," in *Symposium (International) on Combustion*, 1991, vol. 23: Elsevier, 1 ed., pp. 503-511.

[98] S. Liu, J. C. Hewson, J. H. Chen, and H. Pitsch, "Effects of strain rate on high-pressure nonpremixed n-heptane autoignition in counterflow," *Combustion and Flame*, vol. 137, no. 3, pp. 320-339, 2004/05/01/ 2004, doi: https://doi.org/10.1016/j.combustflame.2004.01.011.

[99] Y. Ju, C. B. Reuter, and S. H. Won, "Numerical simulations of premixed cool flames of dimethyl ether/oxygen mixtures," *Combustion and Flame*, vol. 162, no. 10, pp. 3580-3588, 2015/10/01/ 2015, doi: https://doi.org/10.1016/j.combustflame.2015.06.014.

[100] Z. Chen, X. Qin, Y. Ju, Z. Zhao, M. Chaos, and F. L. Dryer, "High temperature ignition and combustion enhancement by dimethyl ether addition to methane–air mixtures," *Proceedings of the Combustion Institute*, vol. 31, no. 1, pp. 1215-1222, 2007/01/01/ 2007, doi: https://doi.org/10.1016/j.proci.2006.07.177.

[101] "Oil and petroleum products explained." U.S. Energy Information Administration. https://www.eia.gov/energyexplained/oil-and-petroleum-products/use-of-oil.php (accessed.

[102] "Monthly Energy Review." https://www.eia.gov/totalenergy/data/monthly/ (accessed.

[103] "Annual Energy Outlook 2022." U.S. Energy Information Administration (EIA). (accessed.

[104] M. Q. Wang and H. S. Huang, "A full fuel-cycle analysis of energy and emissions impacts of transportation fuels produced from natural gas," United States, 2000-01-25 2000. [Online]. Available: https://www.osti.gov/biblio/750803

https://www.osti.gov/servlets/purl/750803

[105] M. Malenshek and D. B. Olsen, "Methane number testing of alternative gaseous fuels," *Fuel*, vol. 88, no. 4, pp. 650-656, 2009.

[106] G. P. McTaggart-Cowan, H. L. Jones, S. N. Rogak, W. K. Bushe, P. G. Hill, and S. R. Munshi, "The effects of high-pressure injection on a compression-ignition, direct injection of natural gas engine," 2005, vol. 47365, pp. 161-173.

[107] K. Kato *et al.*, "Development of engine for natural gas vehicle," *SAE transactions*, pp. 939-947, 1999.

[108] T. Korakianitis, A. M. Namasivayam, and R. J. Crookes, "Natural-gas fueled spark-ignition (SI) and compression-ignition (CI) engine performance and emissions," *Progress in Energy and Combustion Science*, vol. 37, no. 1, pp. 89-112, 2011/02/01/ 2011, doi: https://doi.org/10.1016/j.pecs.2010.04.002.

[109] A.-H. Kakaee, A. Paykani, and M. Ghajar, "The influence of fuel composition on the combustion and emission characteristics of natural gas fueled engines," *Renewable and Sustainable Energy Reviews*, vol. 38, pp. 64-78, 2014/10/01/ 2014, doi: https://doi.org/10.1016/j.rser.2014.05.080.

[110] V. Dieterich, A. Buttler, A. Hanel, H. Spliethoff, and S. Fendt, "Power-to-liquid via synthesis of methanol, DME or Fischer–Tropsch-fuels: a review," *Energy & Environmental Science*, vol. 13, no. 10, pp. 3207-3252, 2020.

[111] T. A. Semelsberger, R. L. Borup, and H. L. Greene, "Dimethyl ether (DME) as an alternative fuel," *Journal of Power Sources*, vol. 156, no. 2, pp. 497-511, 2006/06/01/ 2006, doi: https://doi.org/10.1016/j.jpowsour.2005.05.082.

[112] D. Liuzzi, C. Peinado, M. A. Peña, J. van Kampen, J. Boon, and S. Rojas, "Increasing dimethyl ether production from biomass-derived syngas via sorption enhanced dimethyl ether synthesis," *Sustainable Energy & Fuels*, 10.1039/D0SE01172J vol. 4, no. 11, pp. 5674-5681, 2020, doi: 10.1039/D0SE01172J.

[113] H. M. Cho and B.-Q. He, "Spark ignition natural gas engines—A review," *Energy Conversion and Management*, vol. 48, no. 2, pp. 608-618, 2007/02/01/ 2007, doi: https://doi.org/10.1016/j.enconman.2006.05.023.

[114] S. H. Park and C. S. Lee, "Combustion performance and emission reduction characteristics of automotive DME engine system," *Progress in Energy and Combustion Science*, vol. 39, no. 1, pp. 147-168, 2013/02/01/ 2013, doi: https://doi.org/10.1016/j.pecs.2012.10.002.

[115] H. J. Kim, H. K. Suh, and C. S. Lee, "Numerical and Experimental Study on the Comparison between Diesel and Dimethyl Ether (DME) Spray Behaviors According to Combustion Chamber Shape," *Energy & Fuels*, vol. 22, no. 4, pp. 2851-2860, 2008/07/01 2008, doi: 10.1021/ef8000696.

[116] H. J. Curran, S. L. Fischer, and F. L. Dryer, "The reaction kinetics of dimethyl ether. II: Low-temperature oxidation in flow reactors," *International Journal of Chemical Kinetics*, vol. 32, no. 12, pp. 741-759, 2000.

[117] S. L. Fischer, F. L. Dryer, and H. J. Curran, "The reaction kinetics of dimethyl ether. I: High-temperature pyrolysis and oxidation in flow reactors," *International Journal of Chemical Kinetics*, https://doi.org/10.1002/1097-4601(2000)32:12<713::AID-KIN1>3.0.CO;2-9 vol. 32, no. 12, pp. 713-740, 2000/01/01 2000, doi: https://doi.org/10.1002/1097-4601(2000)32:12<713::AID-KIN1>3.0.CO;2-9.

[118] Z. Zhao, M. Chaos, A. Kazakov, and F. L. Dryer, "Thermal decomposition reaction and a comprehensive kinetic model of dimethyl ether," *International Journal of Chemical Kinetics*, vol. 40, no. 1, pp. 1-18, 2008.

[119] E. Lin, C. B. Reuter, and Y. Ju, "Dynamics and burning limits of near-limit hot, warm, and cool diffusion flames of dimethyl ether at elevated pressures," *Proceedings of the Combustion Institute*, vol. 37, no. 2, pp. 1791-1798, 2019/01/01/ 2019, doi: https://doi.org/10.1016/j.proci.2018.05.082.

[120] S. H. Won, S. Dooley, F. L. Dryer, and Y. Ju, "Kinetic effects of aromatic molecular structures on diffusion flame extinction," *Proceedings of the Combustion Institute*, vol. 33, no. 1, pp. 1163-1170, 2011.

[121] C. Geuzaine and J. F. Remacle, "Gmsh: A 3-D finite element mesh generator with built-in pre-and post-processing facilities," *International journal for numerical methods in engineering*, vol. 79, no. 11, pp. 1309-1331, 2009.

[122] H. Jasak, "OpenFOAM: open source CFD in research and industry," *International Journal of Naval Architecture and Ocean Engineering*, vol. 1, no. 2, pp. 89-94, 2009.

[123] H. Jasak, A. Jemcov, and Z. Tukovic, "OpenFOAM: A C++ library for complex physics simulations," in *International workshop on coupled methods in numerical dynamics*, 2007, vol. 1000: IUC Dubrovnik Croatia, pp. 1-20.

[124] F. Zhang, T. Zirwes, P. Habisreuther, and H. Bockhorn, "Effect of unsteady stretching on the flame local dynamics," *Combustion and Flame*, vol. 175, pp. 170-179, 2017.

[125] T. Zirwes, F. Zhang, P. Habisreuther, J. A. Denev, H. Bockhorn, and D. Trimis, "Implementation and validation of a computationally efficient DNS solver for reacting flows in OpenFOAM," in *14th World Congress on Computational Mechanics, Virtual Congress*, 2020, 2021.

[126] D. E. Rosner, *Transport processes in chemically reacting flow systems*. Courier Corporation, 2012.

[127] D. G. Goodwin, H. K. Moffat, and R. L. Speth, "Cantera: An object-oriented software toolkit for chemical kinetics, thermodynamics, and transport processes, version 2.2. 1," *Cantera Developers, Warrenville, IL*, 2017.

[128] G. V. Rossum, "Python Software Foundation. Python Language Reference, Version 3.7," ed, 1995.

[129] H. A. Van der Vorst, "Bi-CGSTAB: A fast and smoothly converging variant of Bi-CG for the solution of nonsymmetric linear systems," *SIAM Journal on scientific and Statistical Computing*, vol. 13, no. 2, pp. 631-644, 1992.

[130] Y. Saad, "ILUT: A dual threshold incomplete LU factorization," *Numerical linear algebra with applications*, vol. 1, no. 4, pp. 387-402, 1994.

[131] D. S. Kershaw, "The incomplete Cholesky—conjugate gradient method for the iterative solution of systems of linear equations," *Journal of Computational Physics*, vol. 26, no. 1, pp. 43-65, 1978/01/01/ 1978, doi: https://doi.org/10.1016/0021-9991(78)90098-0.

[132] Z. Wang, X. Gou, and C. Zhong, "Experimental and Kinetic Study on the Cool Flame Characteristics of Dimethyl Ether," *Energy & Fuels*, vol. 33, no. 9, pp. 9205-9214, 2019.

[133] H. Nakamura, T. Sugita, T. Tezuka, and K. Maruta, "Study on methane oxidation affected by dimethyl ether oxidation at low temperatures using a micro flow reactor with a controlled temperature profile," *Combustion and Flame*, vol. 223, pp. 320-329, 2021.

[134] R. Zhang, S. Yang, X. Zhou, and D. Liu, "Study of Diffusion Cool Flames of Dimethyl Ether in a Counterflow Burner under a Wide Range of Pressures," *ACS omega*, vol. 7, no. 29, pp. 25087-25093, 2022.

[135] V. Nevrlý *et al.*, "TDLAS-based in situ diagnostics for the combustion of preheated ultra–lean dimethyl ether/air mixtures," *Fuel*, vol. 263, p. 116652, 2020.

[136] X. Gou, J. A. Miller, W. Sun, and Y. Ju, "Implementation of PLOG function in Chemkin II and III," 2011.

[137] J. A. Miller and A. E. Lutz, ed, 2003.

[138] H. J. Curran, "Developing detailed chemical kinetic mechanisms for fuel combustion," *Proceedings of the Combustion Institute*, vol. 37, no. 1, pp. 57-81, 2019/01/01/ 2019, doi: https://doi.org/10.1016/j.proci.2018.06.054.

[139] A. E. Lutz, R. J. Kee, J. F. Grcar, and F. M. Rupley, "OPPDIF: A Fortran program for computing opposed-flow diffusion flames," Sandia National Lab.(SNL-CA), Livermore, CA (United States), 1997.

[140] M. Nishioka, C. K. Law, and T. Takeno, "A flame-controlling continuation method for generating S-curve responses with detailed chemistry," *Combustion and Flame*, vol. 104, no. 3, pp. 328-342, 1996.

[141] Y. Ju, H. Guo, K. Maruta, and F. Liu, "On the extinction limit and flammability limit of non-adiabatic stretched methane–air premixed flames," *Journal of fluid mechanics*, vol. 342, pp. 315-334, 1997.

[142] E. L. Cussler and E. L. Cussler, *Diffusion: mass transfer in fluid systems*. Cambridge university press, 2009.

[143] J. C. R. Hunt, "Lewis fry richardson and his contributions to mathematics, meteorology, and models of conflict," *Annual Review of Fluid Mechanics*, vol. 30, no. 1, pp. xiii-xxxvi, 1998/01/01 1998, doi: 10.1146/annurev.fluid.30.1.0.

[144] H. D. I. Abarbanel, D. D. Holm, J. E. Marsden, and T. Ratiu, "Richardson number criterion for the nonlinear stability of three-dimensional stratified flow," *Physical Review Letters*, vol. 52, no. 26, p. 2352, 1984.

[145] M. N. Bui-Pham and J. A. Miller, "Rich methane/air flames: burning velocities, extinction limits, and flammability limit," in *Symposium (international) on combustion*, 1994, vol. 25, no. 1: Elsevier, pp. 1309-1315.

[146] H.-Y. Shih, "Computed extinction limits and flame structures of H2/O2 counterflow diffusion flames with CO2 dilution," *International Journal of Hydrogen Energy*, vol. 34, no. 9, pp. 4005-4013, 2009/05/01/ 2009, doi: https://doi.org/10.1016/j.ijhydene.2009.03.013.

[147] Z. Wang *et al.*, "Kinetics and extinction of non-premixed cool and warm flames of dimethyl ether at elevated pressure," *Proceedings of the Combustion Institute*, 2022.

[148] J. M. Ploeger *et al.*, "Modeling oxidation and hydrolysis reactions in supercritical water—free radical elementary reaction networks and their applications," *Combustion Science and Technology*, vol. 178, no. 1-3, pp. 363-398, 2006/01/01 2006, doi: 10.1080/00102200500287209.

[149] S. N. Reddy *et al.*, "Hydrothermal flames for subaquatic, terrestrial and extraterrestrial applications," *Journal of Hazardous Materials*, vol. 424, p. 127520, 2022/02/15/ 2022, doi: https://doi.org/10.1016/j.jhazmat.2021.127520.

[150] T. Hirth and E. U. Franck, "Oxidation and Hydrothermolysis of Hydrocarbons in Supercritical Water at High Pressures," *Berichte der Bunsengesellschaft für physikalische Chemie*, https://doi.org/10.1002/bbpc.19930970905 vol. 97, no. 9, pp. 1091-1097, 1993/09/01 1993, doi: https://doi.org/10.1002/bbpc.19930970905.

[151] W. Schilling and E. U. Franck, "Combustion and Diffusion Flames at High Pressures to 2000 bar," *Berichte der Bunsengesellschaft für physikalische Chemie*, vol. 92, no. 5, pp. 631-636, 1988/05/01 1988, doi: 10.1002/bbpc.198800149.

[152] T. T. Bramlette *et al.*, "Destruction of DOE/DP surrogate wastes with supercritical water oxidation technology," United States, 1990. [Online]. Available: http://inis.iaea.org/search/search.aspx?orig_q=RN:23083866

[153] M. C. Hicks, U. G. Hegde, and J. J. Kojima, "Hydrothermal ethanol flames in Co-flow jets," *The Journal of Supercritical Fluids*, vol. 145, pp. 192-200, 2019/03/01/ 2019, doi: https://doi.org/10.1016/j.supflu.2018.12.010.

[154] "Supercritical Water Oxidation (SCWO)," ed.

[155] C. He, C.-L. Chen, A. Giannis, Y. Yang, and J.-Y. Wang, "Hydrothermal gasification of sewage sludge and model compounds for renewable hydrogen production: A review," *Renewable and Sustainable Energy Reviews*, vol. 39, pp. 1127-1142, 2014/11/01/ 2014, doi: https://doi.org/10.1016/j.rser.2014.07.141.

[156] L. Zhang, C. Xu, and P. Champagne, "Overview of recent advances in thermo-chemical conversion of biomass," *Energy Conversion and Management*, vol. 51, no. 5, pp. 969-982, 2010/05/01/ 2010, doi: https://doi.org/10.1016/j.enconman.2009.11.038.

[157] S. Deguchi and K. Tsujii, "Supercritical water: a fascinating medium for soft matter," *Soft Matter*, vol. 3, no. 7, pp. 797-803, 2007.

[158] V. Vadillo, J. Sánchez-Oneto, J. R. Portela, and E. J. Martinez de la Ossa, "Problems in supercritical water oxidation process and proposed solutions," *Industrial & Engineering Chemistry Research*, vol. 52, no. 23, pp. 7617-7629, 2013.

[159] J. P. S. Queiroz, M. D. Bermejo, F. Mato, and M. J. Cocero, "Supercritical water oxidation with hydrothermal flame as internal heat source: Efficient and clean

energy production from waste," *The Journal of Supercritical Fluids*, vol. 96, pp. 103-113, 2015/01/01/ 2015, doi: https://doi.org/10.1016/j.supflu.2014.09.018.

[160] J. W. Tester *et al.*, "Supercritical water oxidation technology: process development and fundamental research," 1993.

[161] A. A. Peterson, F. Vogel, R. P. Lachance, M. Fröling, M. J. Antal Jr, and J. W. Tester, "Thermochemical biofuel production in hydrothermal media: a review of sub-and supercritical water technologies," *Energy & environmental science*, vol. 1, no. 1, pp. 32-65, 2008.

[162] M. Watanabe *et al.*, "Chemical reactions of C1 compounds in near-critical and supercritical water," *Chemical Reviews*, vol. 104, no. 12, pp. 5803-5822, 2004.

[163] S. N. Reddy, S. Nanda, U. G. Hegde, M. C. Hicks, and J. A. Kozinski, "Ignition of hydrothermal flames," *RSC Advances*, 10.1039/C5RA02705E vol. 5, no. 46, pp. 36404-36422, 2015, doi: 10.1039/C5RA02705E.

[164] L. Guo and H. Jin, "Boiling coal in water: Hydrogen production and power generation system with zero net CO2 emission based on coal and supercritical water gasification," *International Journal of Hydrogen Energy*, vol. 38, no. 29, pp. 12953-12967, 2013/09/30/ 2013, doi: https://doi.org/10.1016/j.ijhydene.2013.04.089.

[165] P. Cabeza *et al.*, "Supercritical water oxidation for energy production by hydrothermal flame as internal heat source. Experimental results and energetic study," *Energy*, vol. 90, pp. 1584-1594, 2015/10/01/ 2015, doi: https://doi.org/10.1016/j.energy.2015.06.118.

[166] G. Brunner, "Near critical and supercritical water. Part I. Hydrolytic and hydrothermal processes," *The Journal of Supercritical Fluids,* vol. 47, no. 3, pp. 373-381, 2009/01/01/ 2009, doi: https://doi.org/10.1016/j.supflu.2008.09.002.

[167] M. C. Hicks, U. Hegde, and J. Fisher, "Investigation of supercritical water phenomena for space and extraterrestrial application," in *10th International Symposium on Supercirtical Fluids*, San Francisco, CA, USA, May 13 - 16 2012.

[168] L. Qian, S. Wang, D. Xu, Y. Guo, X. Tang, and L. Wang, "Treatment of municipal sewage sludge in supercritical water: a review," *Water research*, vol. 89, pp. 118-131, 2016.

[169] P. Cabeza *et al.*, "Sludge destruction by means of a hydrothermal flame. Optimization of ammonia destruction conditions," *Chemical Engineering Journal*, vol. 232, pp. 1-9, 2013.

[170] X. Hu *et al.*, "An analytical model to evaluate the heating conditions for drilling in hard rock using an innovative hydrothermal spallation method," *Applied Thermal Engineering*, vol. 142, pp. 709-716, 2018/09/01/ 2018, doi: https://doi.org/10.1016/j.applthermaleng.2018.07.043.

[171] T. Meier, M. J. Schuler, P. Stathopoulos, B. Kramer, and P. Rudolf von Rohr, "Hot surface ignition and monitoring of an internal oxygen–ethanol hydrothermal flame at 260bar," *The Journal of Supercritical Fluids*, vol. 130, pp. 230-238, 2017/12/01/ 2017, doi: https://doi.org/10.1016/j.supflu.2016.09.015.

[172] X. Song, Z. Lyu, G. Li, and X. Hu, "Numerical analysis of the impact flow field of multi-orifice nozzle hydrothermal jet combined with cooling water," *International*

Journal of Heat and Mass Transfer, vol. 114, pp. 578-589, 2017/11/01/ 2017, doi: https://doi.org/10.1016/j.ijheatmasstransfer.2017.06.106.

[173] P. Arcelus-Arrillaga, J. L. Pinilla, K. Hellgardt, and M. Millan, "Application of Water in Hydrothermal Conditions for Upgrading Heavy Oils: A Review," *Energy & Fuels*, vol. 31, no. 5, pp. 4571-4587, 2017/05/18 2017, doi: 10.1021/acs.energyfuels.7b00291.

[174] R. Chand, V. Babu Borugadda, M. Qiu, and A. K. Dalai, "Evaluating the potential for bio-fuel upgrading: A comprehensive analysis of bio-crude and bio-residue from hydrothermal liquefaction of agricultural biomass," *Applied Energy*, vol. 254, p. 113679, 2019/11/15/ 2019, doi: https://doi.org/10.1016/j.apenergy.2019.113679.

[175] Y. Chen, Z. Jing, K. Cai, and J. Li, "Hydrothermal conversion of Cs-polluted soil into pollucite for Cs immobilization," *Chemical Engineering Journal*, vol. 336, pp. 503-509, 2018/03/15/ 2018, doi: https://doi.org/10.1016/j.cej.2017.11.187.

[176] Z. Chen, L. Gao, X. Zhang, W. Han, and S. Li, "High-efficiency power generation system with integrated supercritical water gasification of coal," *Energy*, vol. 159, pp. 810-816, 2018/09/15/ 2018, doi: https://doi.org/10.1016/j.energy.2018.06.140.

[177] F. Zhang, Y. Ding, C. Su, and Z. Chen, "Energy self-sufficiency of a supercritical water oxidation system with an improved cooled-wall reactor for power generation," *Applied Thermal Engineering*, vol. 172, p. 115158, 2020/05/25/ 2020, doi: https://doi.org/10.1016/j.applthermaleng.2020.115158.

[178] S. Nanda, R. Rana, H. N. Hunter, Z. Fang, A. K. Dalai, and J. A. Kozinski, "Hydrothermal catalytic processing of waste cooking oil for hydrogen-rich syngas

production," *Chemical Engineering Science,* vol. 195, pp. 935-945, 2019/02/23/ 2019, doi: https://doi.org/10.1016/j.ces.2018.10.039.

[179] F. Zhang, Y. Li, Z. Liang, T. Wu, and Y. Huang, "Experimental investigation on the oxidation of printing ink wastewater under hydrothermal flames," *Journal of Environmental Chemical Engineering,* vol. 9, no. 6, p. 106745, 2021/12/01/ 2021, doi: https://doi.org/10.1016/j.jece.2021.106745.

[180] K. Dokko, S. Koizumi, K. Sharaishi, and K. Kanamura, "Electrochemical properties of LiFePO4 prepared via hydrothermal route," *Journal of Power Sources,* vol. 165, no. 2, pp. 656-659, 2007.

[181] Y. Yang *et al.*, "Hydrothermal combustion synthesis and characterization of Sr2CeO4 phosphor powders," *Materials Research Bulletin,* vol. 112, pp. 159-164, 2019/04/01/ 2019, doi: https://doi.org/10.1016/j.materresbull.2018.12.018.

[182] J. Zhang, L. Zhang, C. Men, M. Ren, H. Zhang, and J. Lu, "Ignition of supercritical hydrothermal flames in co-flow jets," *The Journal of Supercritical Fluids,* vol. 188, p. 105683, 2022/09/01/ 2022, doi: https://doi.org/10.1016/j.supflu.2022.105683.

[183] A. Mansfield, E. Keena, and N. Sophonrat, "An experimental investigation of methanol combustion in low temperature supercritical water," *The Journal of Supercritical Fluids,* vol. 184, p. 105566, 2022.

[184] T. Gallaway, S. P. Antal, and M. Z. Podowski, "Multi-dimensional model of fluid flow and heat transfer in Generation-IV Supercritical Water Reactors," *Nuclear Engineering and Design,* vol. 238, no. 8, pp. 1909-1916, 2008/08/01/ 2008, doi: https://doi.org/10.1016/j.nucengdes.2007.11.019.

[185] M. C. Hicks, U. G. Hegde, and J. J. Kojima, "Spontaneous Ignition of Hydrothermal Flames in Supercritical Ethanol Water Solutions," presented at the 10th U.S. National Combustion Meeting, College Park, MD; United States, 2017.

[186] S. N. Reddy, S. Nanda, U. G. Hegde, M. C. Hicks, and J. A. Kozinski, "Ignition of n-propanol–air hydrothermal flames during supercritical water oxidation," *Proceedings of the Combustion Institute,* vol. 36, no. 2, pp. 2503-2511, 2017/01/01/ 2017, doi: https://doi.org/10.1016/j.proci.2016.05.042.

[187] M. D. Bermejo, C. Jiménez, P. Cabeza, A. Matías-Gago, and M. J. Cocero, "Experimental study of hydrothermal flames formation using a tubular injector in a refrigerated reaction chamber. Influence of the operational and geometrical parameters," *The Journal of Supercritical Fluids,* vol. 59, pp. 140-148, 2011/11/01/ 2011, doi: https://doi.org/10.1016/j.supflu.2011.08.009.

[188] R. Allam *et al.*, "Demonstration of the Allam Cycle: An update on the development status of high efficiency supercritical carbon dioxide process employing full carbon capture," *Energy Procedia,* vol. 114, pp. 5948 - 5966, 2017.

[189] G. Pont *et al.*, "DECLIC, soon two years of successful operations," presented at the 62nd International Astronautical Congress, Cape Town, South Africa, October 3 - 7, 2011.

[190] D. L. Urban, "NASA Microgravity Combustion Program," 2015, GRC-E-DAA-TN27493 ed.

[191] U. Hegde, M. Hicks, C. Lecoutre, and Y. Garrabos, "Influence of a Temperature Gradient on the Behavior of Near-Critical Water in Microgravity," 2011 2011, p. 5238.

[192] Z. Gao, H. Wang, C. Song, K. Luo, and J. Fan, "Real-fluid effects on laminar diffusion and premixed hydrothermal flames," *The Journal of Supercritical Fluids*, vol. 153, p. 104566, 2019/11/01/ 2019, doi: https://doi.org/10.1016/j.supflu.2019.104566.

[193] C. H. Oh, R. J. Kochan, and J. M. Beller, "Numerical analysis and data comparison of a supercritical water oxidation reactor," *AIChE Journal*, vol. 43, no. 6, pp. 1627-1636, 1997/06/01 1997, doi: 10.1002/aic.690430626.

[194] N. Zhou, A. Krishnan, F. Vogel, and W. A. Peters, "A computational model for supercritical water oxidation of organic toxic wastes," *Advances in Environmental Research*, vol. 4, no. 1, pp. 75-90, 2000/06/01/ 2000, doi: https://doi.org/10.1016/S1093-0191(00)00011-3.

[195] P. A. Webley and J. W. Tester, "Fundamental Kinetics of Methane Oxidation in Supercritical Water," *Energy & Fuel* vol. 5, no. 3, pp. 411-419, 1991.

[196] C. Narayanan, C. Frouzakis, K. Boulouchos, K. Príkopský, B. Wellig, and P. Rudolf von Rohr, "Numerical modelling of a supercritical water oxidation reactor containing a hydrothermal flame," *The Journal of Supercritical Fluids*, vol. 46, no. 2, pp. 149-155, 2008/09/01/ 2008, doi: https://doi.org/10.1016/j.supflu.2008.04.005.

[197] J. P. S. Queiroz, M. D. Bermejo, and M. J. Cocero, "Kinetic model for isopropanol oxidation in supercritical water in hydrothermal flame regime and analysis," *The Journal of Supercritical Fluids*, vol. 76, pp. 41-47, 2013/04/01/ 2013, doi: https://doi.org/10.1016/j.supflu.2013.01.021.

[198] S. N. Reddy, S. Nanda, P. Kumar, M. C. Hicks, U. G. Hegde, and J. A. Kozinski, "Impacts of oxidant characteristics on the ignition of n-propanol-air hydrothermal flames in supercritical water," *Combustion and Flame,* vol. 203, pp. 46-55, 2019/05/01/ 2019, doi: https://doi.org/10.1016/j.combustflame.2019.02.004.

[199] M. Ren, S. Wang, and D. Roekaerts, "Numerical study of the counterflow diffusion flames of methanol hydrothermal combustion: The real-fluid effects and flamelet analysis," *The Journal of Supercritical Fluids,* vol. 152, p. 104552, 2019/10/01/ 2019, doi: https://doi.org/10.1016/j.supflu.2019.104552.

[200] J. Li, Z. Zhao, A. Kazakov, M. Chaos, F. L. Dryer, and J. J. Scire Jr, "A comprehensive kinetic mechanism for CO, CH2O, and CH3OH combustion," *International Journal of Chemical Kinetics,* vol. 39, no. 3, pp. 109-136, 2007/03/01 2007, doi: 10.1002/kin.20218.

[201] A. B. Mansfield, "Corrigendum to: “A revised chemical kinetic mechanism for methanol combustion in sub and supercritical water” [J. Supercrit. Fluids 166 (2020)]," *The Journal of Supercritical Fluids,* vol. 173, p. 105225, 2021/07/01/ 2021, doi: https://doi.org/10.1016/j.supflu.2021.105225.

[202] F. Vogel *et al.*, "Critical review of kinetic data for the oxidation of methanol in supercritical water," *The Journal of Supercritical Fluids,* vol. 34, no. 3, pp. 249-286, 2005/07/01/ 2005, doi: https://doi.org/10.1016/j.supflu.2003.12.018.

[203] C. N. Hamelinck and A. P. C. Faaij, "Future prospects for production of methanol and hydrogen from biomass," *Journal of Power Sources,* vol. 111, no. 1, pp. 1-22, 2002/09/18/ 2002, doi: https://doi.org/10.1016/S0378-7753(02)00220-3.

[204] S. Masoumi and A. K. Dalai, "Techno-economic and life cycle analysis of biofuel production via hydrothermal liquefaction of microalgae in a methanol-water system and catalytic hydrotreatment using hydrochar as a catalyst support," *Biomass and Bioenergy*, vol. 151, p. 106168, 2021.

[205] P. R. Von Rohr, K. Prikopsky, and T. Rothenfluh, "Flames in supercritical water and their applications," *Strojnicky Casopis*, vol. 59, no. 2, pp. 91-103103, 2008.

[206] B. Wellig, K. Lieball, and P. R. von Rohr, "Operating characteristics of a transpiring-wall SCWO reactor with a hydrothermal flame as internal heat source," *The Journal of supercritical fluids*, vol. 34, no. 1, pp. 35-50, 2005.

APPENDIX A: COMPARISON BETWEEN 1D CHEMKIN AND 2D AXISYMMETRIC OPENFOAM SIMULATION RESULTS

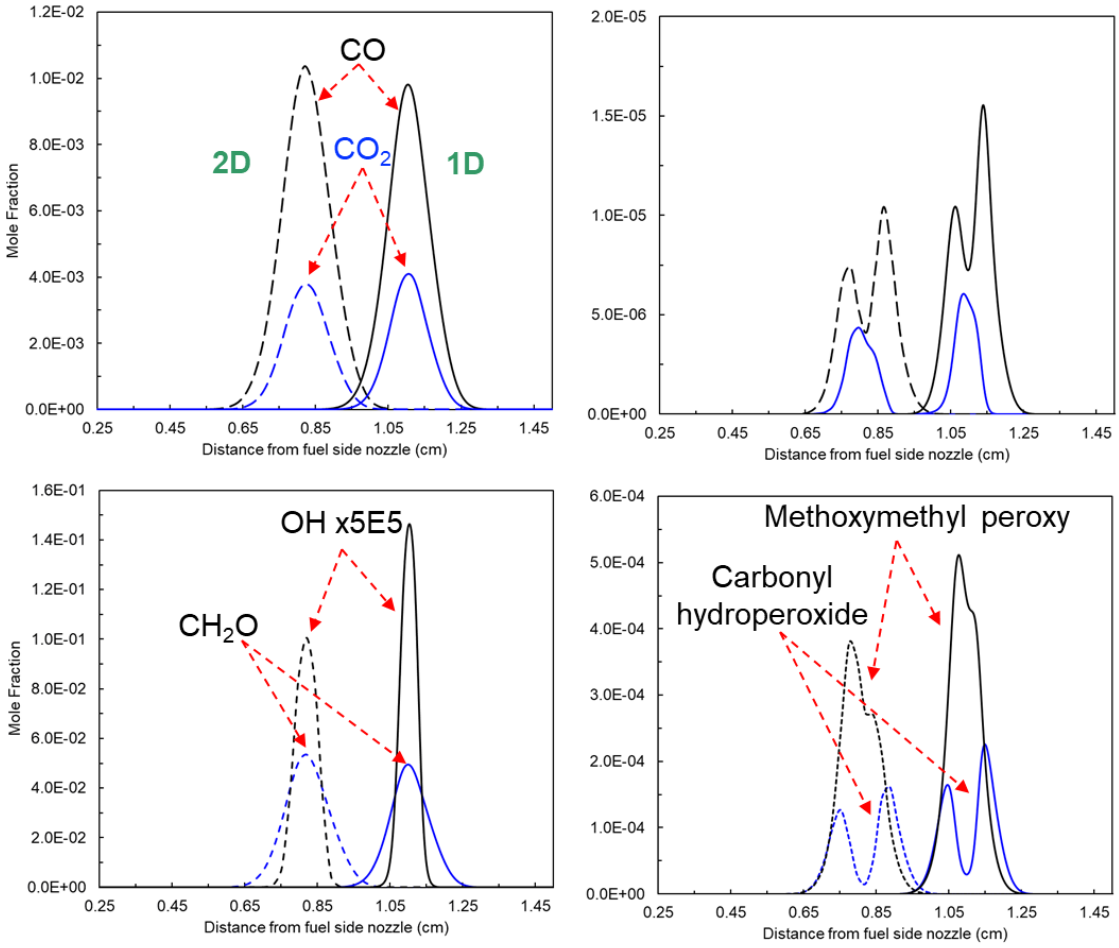

Figure A1: Comparison of species distribution between 1D and 2D model prediction.

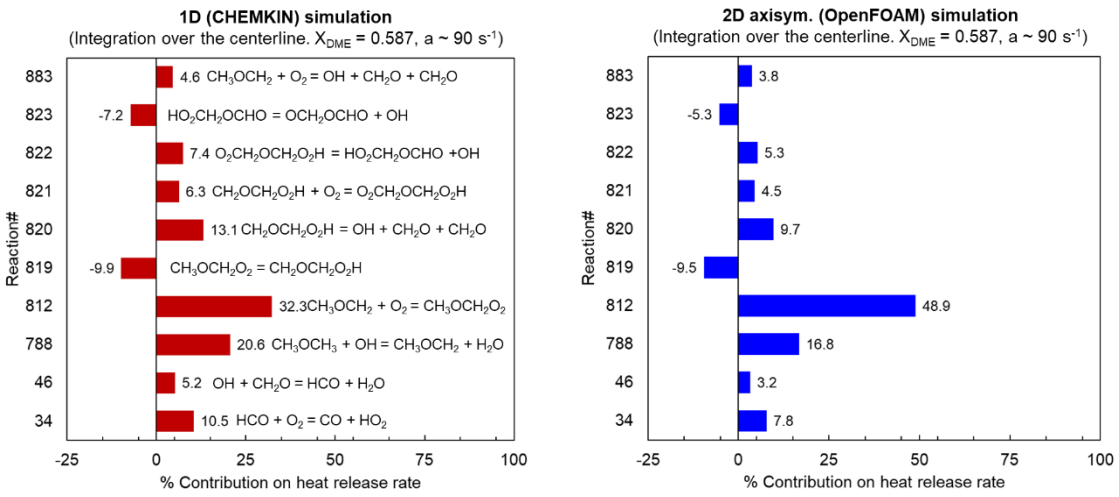

Figure A2: Comparison of 1D and 2D model prediction on the heat production from major reactions contributing to the chemical heat release.

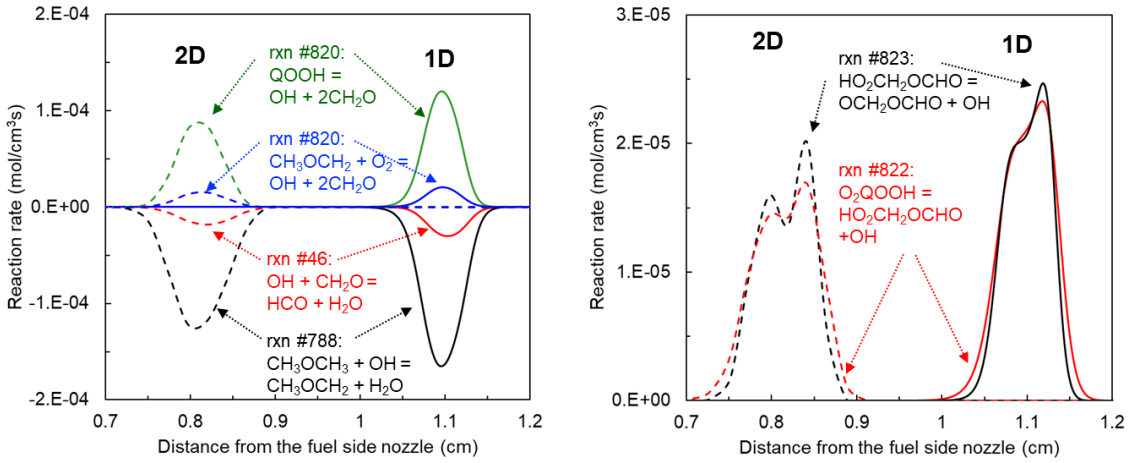

Figure A3: Comparison of 1D and 2D model prediction on the rate of production (ROP) of OH radical.

APPENDIX B: ACADEMIC VITAE

Sudipta Saha, EIT
43 Indian Pipe, Painted Post, NY 14870, 803-445-5772
sahas4@corning.com, www.linkedin.com/in/sudipta-saha-usc

EDUCATION

Doctor of Philosophy in Mechanical Engineering Expected graduation date: May, 2023
University of South Carolina, Columbia, SC CGPA: 3.90/4.00
Dissertation: Multi-dimensional Reacting Flow Simulation of Low Temperature Diffusion Flame

Master of Science in Mechanical Engineering May, 2019
University of South Carolina, Columbia, SC CGPA: 4.00/4.00
Thesis: Numerical analysis on convective cooling augmented by evaporative heat and mass transfer for thermal power plant application (Outstanding Thesis Award)

Bachelor of Science in Mechanical Engineering February, 2013
Bangladesh University of Engr. and Tech., Dhaka, Bangladesh CGPA: 3.61/4/00
Thesis: Experimental determination of Head loss and minor loss coefficient of locally made PVC Reducers

PROFESSIONAL EXPERIENCE

R&D Engineer, Corning Incorporated, NY July, 2022 - present

- Develops CFD models for early stage hot-glass innovation projects.
- Analyzes combustion system for the catalytic converter development and fiber making process.
- Designs experiments for technology development for the next-generation display materials.

Spent Fuel Modeling Intern, Idaho National Laboratory, ID June-Sept., 2020

- Developed CFD model representative of the geometry in the spent nuclear fuel (SNF) report.
- Used the CFD model to test other turbulence models for higher accuracy, large eddy simulation.
- Performed study of neutron poison corrosion potential in materials for DOE canisters.

Graduate Research Assistant, University of South Carolina, SC Aug., 2015-June, 2022

- Developed computational model for hybrid cooling system for heat transfer enhancement.
- Performed modeling and simulation of thermal-fluid and reacting flow system.
- Prepared annual and final reports for the projects funded by NSF and DOE.

Junior Energy Auditor, Sodev Consult International Ltd., Dhaka, Bangladesh. May 2013- January 2014

- Completed USAID projects on energy efficiency in industrial application in Bangladesh.
- Visited several textile plants and investigated heavy energy consuming equipment (Boiler, Gas Turbine etc.) and HVAC system to find potential sources of energy conservation.

Industrial Trainee Sanofi Bangladesh Ltd., Gazipur, Bangladesh April-May 2012

- Completed projects on energy sustainability in pharmaceutical industries
- Presented project summary focusing on reduction of emission from pharmaceutical plants

AWARDS AND HONORS

SPARC Graduate Research Grant Program, 2018
Received $5,000 research grant by University of South Carolina Office of Research for a proposal on development of numerical model for investigation of hybrid cooling method in industries.

Outstanding Thesis Award, 2019
Awarded by UofSC Graduate School for completing exceptional Master's thesis in the university.

American Nuclear Society (ANS) Graduate Scholarship Award, 2021
Awarded for research contribution to thermal hydraulic analyses regarding nuclear waste management.

The Duke of Edinburgh's Award, 2010
Awarded by The Duke of Edinburgh's International Award Foundation on leadership and teamwork

Research Travel Grant
National Science Foundation (NSF), 2019; American Nuclear Society (ANS)

The Outstanding Achievement and Student Triumph Award (T.O.A.S.T), 2020
Awarded by Leadership and Service Center, University of South Carolina for showing commitment to a student organization, university department or program; and other areas of student life.

CERTIFICATION AND TRAINING

Preparing Future Faculty (PFF)
Center for Teaching Excellence (CTE), University of South Carolina

Engineer-in-Training (Certification no. EIT – 21136)
Board of Registration for Professional Engineers and Surveyors, South Carolina

Princeton-Combustion Institute Summer School on Combustion, 2017
The Combustion Energy Frontier Research Center (CEFRC), Princeton University, Princeton, NJ

Responsible Conduct of Research (RCR) for Engineers
Collaborative Institutional Training Initiative (CITI), National Science Foundation (NSF)

Fostering Proactive Learning Environments (FPLE)
Center for Teaching Excellence (CTE), University of South Carolina

Teaching Towards Inclusive Excellence (TTIE)
Center for Teaching Excellence (CTE), University of South Carolina

SELECTED PUBLICATIONS (Peer-reviewed)

Journals:

Saha, S., Khan, J., & Farouk, T. (2020). Numerical study of evaporation assisted hybrid cooling for thermal powerplant application. *Applied Thermal Engineering*, *166*, 114677.

Saha, S., Khan, J., Knight, T., & Farouk, T. (2022). A Global Model for Predicting Vacuum Drying of Used Nuclear Fuel Assemblies. *Nuclear Technology*, *208*(3), 414-427.

Hoque, S., Tahiyat, M. M., Abbas, N. Z., **Saha, S.**, Berge, N. D., Flora, J. V., & Farouk, T. I. (2019). Atmospheric pressure dielectric barrier discharge for siloxane reformation. *Journal of Physics D: Applied Physics*, *53*(1), 015202.

Prince, H. A., Redwan, D. A., Rozin, E. H., **Saha, S.**, & Mamun, M. A. H. (2021). Augmentation of pure mixed convection heat transfer in a non-newtonian power-law fluid filled lid-driven trapezoidal cavity with double rotating cylinders. *Journal of Heat Transfer*, *143*(8).

Saha, S., Tikadar, A., Knight, T. W., Khan, J. A., & Farouk, T. I. (2019). Can an analytical model be employed for simulating used fuel vacuum drying process?. *Trans. Am. Nucl. Soc*, *121*(1), 175.

Tikadar, A., **Saha, S.**, Knight, T. W., Farouk, T. I., & Khan, J. A. (2019). CFD Framework for Used Fuel Vacuum Drying Application. *Trans. Am. Nucl. Soc*, *121*(1), 179.

S. Saha, T. Farouk, "Numerical analyses of methanol-air hydrothermal flame in supercritical water", (under preparation for *Journal of Supercritical Fluids*)

Conference Proceedings:

Saha, S., Tikadar, A., Khan, J., & Farouk, T. (2019, November). Numerical analysis on evaporation assisted convective cooling: effect of surface morphology. *ASME International Mechanical Engineering Congress and Exposition* (Vol. 59452, p. V008T09A051). American Society of Mechanical Engineers.

Saha, S., Mahamud, R., Khan, J., & Farouk, T. (2017, July). Simulation of sweating/evaporation boosted convective heat transfer under laminar flow condition. *Heat Transfer Summer Conference* (Vol. 57885, p. V001T09A016). American Society of Mechanical Engineers.

Saha, S., Khan, J., & Farouk, T. (2020, July). Study of hybrid wet/dry cooling with different surface morphology: Analyses on pressure drop and thermal performances. *Heat Transfer Summer Conference* (Vol. 83709, p. V001T12A015). American Society of Mechanical Engineers.

CONFERENCE PRESENTATION

Saha, S., Ahmed, S., & Farouk, T. (2019). "Numerical investigation on hydrothermal flame of supercritical methanol combustion," 11th U. S. National Combustion Meeting, Pasadena, CA, 2019, pp. 71EA-0480.

Saha, S. & Farouk, T. (2020). "Simulation of Methanol-Air Hydrothermal Flames During Supercritical Water Oxidation: Impact of Kinetic Parameters " 2020 Spring Technical Meeting of the Eastern States Section of Combustion Institute, Columbia, SC, 2020, pp. 109010-0023

SELECTED PROJECTS

Multi-Phase Multi-Physics Modeling of Heat Transfer Enhancement in Practical Approach

- Developed CFD model of an evaporation assisted cooling system in **COMSOL Multiphysics**
- Conducted simulation based on various parameter to optimize proposed thermal system
- Prepares annual and final reports of research outcomes for projects funded by NSF

Modeling of Supercritical Water Oxidation (SCWO) of Methanol Combustion

- Developed model in **ANSYS Fluent** and simulated hydrothermal flame at supercritical condition
- Analyzed the simulation results and validated with similar experimental data

Numerical Investigation of counterflow cool flame structure for dimethyl ether combustion

- Conducted modeling and simulation of DME cool flame in counterflow geometry
- Investigation of the effect of multidimensional transport on diffusion flame formation

Modeling of Vacuum Drying Process for Waste/Spent Nuclear Fuel Rod Assembly

- Conducted thermal hydraulic analyses of failed nuclear fuel rod assemblies in Integrated Research Project (IRP) funded by NEUP, DOE
- Developed **MATLAB** code to simulate dry vacuum process of spent nuclear fuel rods

Unraveling Hidden Physics in Multiphase Combustion: Preferential Vaporization

- Conducted the development of multiphase multiphysics numerical model of droplet combustion
- Investigated the preferential vaporization of multi-component droplet evaporation and burning

LEADERSHIP AND ORGANIZATIONAL EXPERIENCES

Graduate Council Representative, University of South Carolina (UofSC), 2020-21

- Elected representative of Graduate Student Association (GSA) at UofSC Graduate Council
- Serves on the academic *Grievances, Appeals and Petitions Committee*
- Advocates for the better representation of the graduate and professional needs of students
- Facilitates *Diversity Equality and Inclusion* (DEI) efforts taken by the university offices

Leadership Member, Midland Section, American Society of Mech. Engineering (ASME), 2021-22

- Provides local/geographic engagement for the ASME members
- Contributes to the augmentation of networking opportunity and professional development

Secretary, Graduate Student Association (GSA), UofSC, 2019-20

- Served as a *Secretary of Graduate Student Organization*
- Developed a central database for the campus graduate student organizations
- Planned and organized GSA Townhall Meetings
- Served on the University's *Provost Search Committee* (2019)

Representative, Student Advisory Council, Thomas Cooper Library, UofSC, 2018-19

- Worked on the better accommodation for the graduate students at university library facilities
- Attended semester meetings conducted by the associated dean of the university library
- Provided inputs on the dissemination of library facilities among the diverse group of students

Vice President, International Student Association, UofSC, 2019-20

- Promotes interaction between local and international student communities at the campus
- Organizes social events, trivia nights, watch party to bring diverse student communities together

Vice President, Graduate Student Org. of Dept. of Mech. Engr. (ME-GSO), UofSC 2021-22

- Co-founder of the organization
- Plans and organizes academic talks, career development events for the graduate students

ACADEMIC SERVICES

- **Enlisted peer-reviewer**
  - *Int. J. of Heat & Mass Transfer*
  - *Int. J. of Heat & Fluid Flow*
  - *Nuclear Technology*
  - *J. of Therm. Sci. & Engr. Application,*
  - *Energy for Sustainable Development.*
  - *Nuclear Science and Engineering*
- Adjudicated at Student Design Competition at **American Nuclear Society (ANS) Winter Meeting & Expo**, Washington DC, 2019
- Acted as a proctor at **Student Disability Resource Center** at Univ. of South Carolina, 2018
- Served as Knowledge Manager Intern at American Nuclear Society **Utility Working Conference (UWC)** Virtual Summit, August 2020.

PROFESSIONAL AFFILIATION

- American Society of Mechanical Engineers (ASME): *Leadership Member of the Midland Section*
- American Nuclear. Society (ANS): *Member of Standard Committee*
- Society of Automotive Engineers (SAE): *Young Professionals Advisory Board*

MEDIA PRESENCE

- "Saha receives UofSC 2020 Outstanding Thesis Award"

https://www.sc.edu/study/colleges_schools/engineering_and_computing/news_events/news/2020/saha_outstandingthesis.php

- "Graduate Student Association overcomes communication challenges between administration, students". The Daily Gamecock, 06/07/2020

https://www.dailygamecock.com/article/2020/06/graduate-student-association-overcomes-communication-challenges-between-administration-students-poag-news

- "COVID-19 impacts student visa distribution, international students" The Daily Gamecock, 11/18/2020

https://www.dailygamecock.com/article/2020/11/covid-impacts-student-visas-international-students-news-capps

- Society of Automotive Engineers (SAE): "STEM@HOME: Meet the Engineers" Video Series

https://www.sae.org/learn/education/stem-at-home/explore/meet-the-engineer